Design and Optimization of Avalanche Photodiodes

by

Khashayar Ghaffari
B.Sc., University of Tehran, 2016

A Thesis Submitted in Partial Fulfillment of the
Requirements for the Degree of

MASTER OF APPLIED SCIENCE

in the Department of Electrical and Computer Engineering

© Khashayar Ghaffari, 2019
University of Victoria

All rights reserved. This thesis may not be reproduced in whole or in part,
by photocopy or other means, without the permission of the author.

Design and Optimization of Avalanche Photodiodes

by

Khashayar Ghaffari
B.Sc., University of Tehran, 2016

Supervisory Committee

Dr. Tao Lu, Supervisor
(Department of Electrical and Computer Engineering)

Dr. Reuven Gordon, Departmental Member
(Department of Electrical and Computer Engineering)

Supervisory Committee

Dr. Tao Lu, Supervisor
(Department of Electrical and Computer Engineering)

Dr. Reuven Gordon, Departmental Member
(Department of Electrical and Computer Engineering)

ABSTRACT

Avalanche photodiodes are the primary choice for photodetection in optical access networks, due to their capacity to meet the current requirements of bandwidth and sensitivity introduced by NG-PON2. This work provides an effective tool for modeling and predicting the operation of an avalanche photodiode, paving the way to making better performing receivers.

We employed Lumerical to obtain several steady state and transient parameters for a silicon germanium SACM waveguide avalanche photodiode, where close agreement is illustrated between our findings and measurements reported on fabricated devices. The utility of our work is further demonstrated by implementing and modeling a device, designed to meet certain fabrication specifications, where optimization guidelines are suggested afterwards.

By providing an accurate approximation of the avalanche photodiode operation, we offer a cost-effective approach to address the problem of fabricating better devices in optical access networks. The introduced methods can be similarly used for other types of photodiodes, contributing to a vast range of applications.

Contents

Supervisory Committee ii

Abstract iii

Table of Contents iv

List of Tables vii

List of Figures viii

Acknowledgments xii

Dedication xiii

1 Introduction 1
- 1.1 Contribution . . . 2
- 1.2 Thesis Outline . . . 2

2 Passive Optical Networks 4
- 2.1 Access Networks . . . 4
- 2.2 Optical Access Networks . . . 6
- 2.3 PON Evolution . . . 8
- 2.4 Photodetection in PON . . . 9

3 Avalanche Photodiode 11
- 3.1 Impact Ionization . . . 11
- 3.2 Multiplication Gain . . . 13
- 3.3 Dark Current . . . 13
- 3.4 Excess Noise . . . 15

3.5 Bandwidth . . . 16
3.6 Sub-micron Scaling of the Multiplication Layer . . . 19
3.7 Impact Ionization Engineering (I^2E) . . . 21
3.8 Waveguide Integration . . . 22
3.9 SACM APD . . . 23
3.10 Sensitivity and Optimal Operation Point . . . 24
3.11 Noise Equivalent Power . . . 25

4 Lateral PIN Photodiode **28**
4.1 Introduction . . . 28
4.2 Structure . . . 28
4.3 Quantum Efficiency . . . 29
4.3.1 Internal Quantum Efficiency (IQE) . . . 31
4.3.2 Reflection and Transmission Losses . . . 37
4.3.3 Photosensitive Area . . . 43
4.4 Dark Current . . . 47
4.5 Considerations . . . 48
4.6 Conclusion . . . 48

5 SiGe SACM Waveguide Avalanche Photodiode **50**
5.1 Structure . . . 50
5.2 Simulation . . . 53
5.2.1 Optical Simulation and Generation . . . 54
5.2.2 Electrical Simulation . . . 57
5.3 Results . . . 59
5.3.1 Mesh and Accuracy . . . 59
5.3.2 Electric Field . . . 64
5.3.3 Current . . . 65
5.3.4 Responsivity . . . 68
5.3.5 Multiplication Gain . . . 71
5.3.6 Transient Response and Bandwidth . . . 72
5.3.7 Excess Noise Factor . . . 76
5.3.8 Noise Equivalent Power . . . 80

6 Fabrication Adjustments and Optimization **83**
6.1 Fabrication Specifications . . . 83
6.2 Structure . . . 84
6.3 Results . . . 87

6.3.1 Electric Field 87
6.3.2 Current 88
6.3.3 Responsivity 89
6.3.4 Multiplication Gain 90
6.3.5 Bandwidth 91
6.4 Optimization 92
6.4.1 Total Length 92
6.4.2 Total Width 94
6.4.3 Rib Width 96
6.4.4 Doping 100
6.4.5 Gain-bandwidth product 102
6.4.6 Conclusion 105

7 Conclusion **106**

Bibliography **107**

Appendix **116**

List of Tables

5.1 Dopant type, doping level and thickness of layers in the silicon germanium photodiode. 52
5.2 Refractive index of materials used in the silicon germanium avalanche photodiode. 53
5.3 Data points for Fig. 5.15. 62
5.4 Obtained $|E|$ and k-value at each bias voltage and multiplication gain. 77

List of Figures

2.1 Total internal reflection in an optical fiber [4]. 6
2.2 Various formats of FTTX [6]. 7
2.3 Basic representation of a passive optical network [58]. 8

3.1 An initial electron creating an electron-hole pair. Due to presense of high electric field the secondary carriers can gain enough energy to initiate more generations. [3] 12
3.2 Theoretical excess noise as a function of multiplication gain for different k-values [60]. 16
3.3 Schematic representation of RCE-SACM APD [26]. 18
3.4 Calculated 3 dB bandwidth as a function of multiplication gain, for different k-values. The dashed line indicates where $M = 1/k$ (edited). [27] 19
3.5 Measured (symbols) and calculated (lines) excess noise factors for different multiplication layer thickness (w) as a function of multiplication factor. w = 850 nm ($\bigcirc$, dashed line), w = 490 nm ($\square$, dotted line), w = 90 nm ($\triangle$, dash-dotted line), w = 49 nm ($\triangledown$), and w = 26 nm ($\diamond$). The inset presents the excess noise factors for electron-hole initiated multiplication (black symbols) and purely by electrons initiated multiplication for w = 850 nm ($\bullet, \bigcirc$) and w = 49 nm ($\blacktriangledown, \triangledown$). Curves for different k-values are also represented as dotted lines. [73] 20
3.6 measured and simulated excess noise factor as a function of gain. [25] 21
3.7 Ge/Si waveguide pin photodetector. The waveguide is placed on top of the photodetector and light is coupled using evanescent coupling. [12] 23

3.8 Ge/Si waveguide avalanche photodetector. a) evanescent-coupled and b) butt-coupled device. [46] 23
3.9 Theoretical SNR as a function of multiplication gain for different k-values. [67] 25
3.10 Theoretical NEP as a function of multiplication gain for different k-values [2]. R= 0.8 A/W, $I_1 = 1nA$. 26

4.1 lateral PIN photodiode, 3D view. 29
4.2 lateral pin photodiode, side view. 30
4.3 Internal Quantum Efficiency for $0 < L_i < 200\mu m$. 38
4.4 Refractive index profile of SiO_2. 38
4.5 Refractive index profile of Si. 38
4.6 Reflectance of the structure given SiO_2 thickness of 300nm. . 39
4.7 Absorption coefficient profile of silicon. 42
4.8 Transmittance in the intrinsic region. 42
4.9 $\eta = (1-R)\cdot(1-T)$. 43
4.10 *pin* photodiode, top view. 44
4.11 Number of fingers vs intrinsic region length; $L_t = 75\mu m, L_{PN} = 1\mu m$. 45
4.12 α_{ph} vs L_i; $L_{PN} = 1\mu m, V_d = -3V, W = 75\mu m, L_t = 75\mu m, t_{si} = 80nm$. 46
4.13 α_{ph} vs L_i; $L_{PN} = 0.12\mu m, V_d = -3V, W = 75\mu m, L_t = 75\mu m, t_{si} = 80nm$. 46
4.14 External Quantum Efficiency vs L_i; $L_{PN} = 1\mu m$. 46
4.15 External Quantum Efficiency vs L_i; $L_{PN} = 0.12\mu m$. 46
4.16 Dark current vs L_i. 47

5.1 Layers thickness and doping profile. 51
5.2 Design details, top view. 52
5.3 Refractive index basic representation. 53
5.4 Structure implemented in FDTD environment. 54
5.5 Light source with fundamental mode, XZ plane. 55
5.6 Electric field, top view $z = 1.04\mu m$. 56
5.7 Electric field, top view $z = 1.34\mu m$. 56
5.8 Generation in absorbing layer, top view $z = 1.04\mu m$. 56
5.9 Generation in absorbing layer, top view $z = 1.34\mu m$. 56
5.10 Generation in absorbing layer, averaged along y direction, top view $z = 1.04\mu m$. 57

5.11 Generation in absorbing layer, averaged along y direction, top view $z = 1.34\mu m$. 57
5.12 Implemented design in Lumerical DEVICE environment. . . . 58
5.13 Generated mesh. maximum edge length = 200 nm, minimum edge length = 500 pm. 60
5.14 Dark current as a function of applied bias voltage. 61
5.15 Obtained dark current as a function of mesh minimum edge length, for $V = -9$ and $V = -5$. 62
5.16 Relative error for obtained dark current as a function of mesh minimum edge length, for $V = -9$ and $V = -5$. 63
5.17 Electric field at a) $-5V$ and b) $-9V$, side view. 64
5.18 A comparison between simulation results and reported measurements for current (I) and its dark component (I_d). Simulation results are presented by Lumerical [1]; Fabricated device and measurements reported by Huang et al. [44]. 66
5.19 Current (for different input powers) and dark current as a function of applied bias voltage. $\lambda = 1550nm$. 67
5.20 Photocurrent as a function of input power for $V = -12V$ and $V = -4V$. $\lambda = 1550nm$. 68
5.21 Responsivity vs Applied Reverse Bias Voltage for four different wavelengths. 69
5.22 Responsivity vs Wavelength for $V = -9V$ and $V = -5V$. Input power = $1\mu W$. 70
5.23 Normalized absorbed power derived in FDTD as a function of wavelength. 71
5.24 Gain as a function of applied bias voltage. 72
5.25 Impulse response at V= $-9V$. 73
5.26 3dB bandwidth for V= $-9V$. 74
5.27 Bandwidth as a function of minimum time step. 75
5.28 Relative error as a function of minimum time step. 76
5.29 Excess noise factor as a function of multiplication gain. 78
5.30 Excess noise factor as a function of applied bias voltage. . . . 79
5.31 Noise equivalent power as a function of multiplication gain. . 81
5.32 Noise equivalent power as a function of applied bias voltage. . 82

6.1 A general schematic of the device. 84
6.2 The simulated design, side view. 85
6.3 The simulated design, top view. 86

6.4 The design implemented in Lumerical, 3D view. 87
6.5 Electric field, a) at $V = -10V$ b) at $V = -20V$. Side view. . . . 88
6.6 Photocurrent (for input power $= 1\mu W$) and dark current as a function of applied bias voltage. $\lambda = 1550nm$. 89
6.7 Responsivity as a function of applied bias voltage for four different wavelengths. Input power $= 1\mu W$. 90
6.8 Multiplication gain as a function of applied bias voltage. $\lambda = 1550nm$, Input Power $= 1\mu W$. 91
6.9 3dB bandwidth for $V = -20V$. $\lambda = 1550nm$ and input power $= 1\mu W$. 92
6.10 Photocurrent as a function of device total length, for $V = -20V$ and $V = -10V$. $\lambda = 1550nm$ and input power $= 1\mu W$. 93
6.11 Bandwidth as a function of device total length. $V = -20V$, $\lambda = 1550nm$, and input power $= 1\mu W$. 94
6.12 Photocurrent as a function of device total width, for $V = -20V$ and $V = -10V$. $\lambda = 1550nm$ and input power $= 1\mu W$. 95
6.13 Bandwidth as a function of device total width. $V = -20V$, $\lambda = 1550nm$, and input power $= 1\mu W$. 96
6.14 Multiplication gain as a function of applied bias voltage for rib width $= 7\mu m$. $\lambda = 1550nm$ and input power $= 1\mu W$. . . . 97
6.15 Multiplication gain as a function of applied bias voltage for rib width $= 9\mu m$. $\lambda = 1550nm$ and input power $= 1\mu W$. . . . 98
6.16 3dB bandwidth for rib width $= 7\mu m$. $V = -20V$, $\lambda = 1550nm$, and input Power $= 1\mu W$. 99
6.17 3dB bandwidth for rib width $= 9\mu m$. $V = -20V$, $\lambda = 1550nm$, and input power $= 1\mu W$. 100
6.18 Multiplication gain as a function of applied bias voltage for structure with altered doping. $\lambda = 1550nm$ and input power $= 1\mu W$. 101
6.19 3dB bandwidth for structure with altered doping. $V = -7.5V$, $\lambda = 1550nm$, and input power $= 1\mu W$. 102
6.20 Gain-bandwidth product as a function of device length. $V = -7V$, $\lambda = 1550nm$, and input power $= 1\mu W$. 103
6.21 Gain-bandwidth product as a function of rib width. $V = -7$, $\lambda = 1550nm$, input power $= 1\mu W$, and total length $= 25\mu m$. . 104

ACKNOWLEDGMENTS

I would like to express my gratitude to my supervisor Dr. Tao Lu for his valuable guidance and insightful suggestions throughout my program and for providing me with the opportunity to be a part of the bio and nanophotonics lab.
I would also like to thank members of my advisory committee, Dr. Reuven Gordon and Dr. Alexandara Branzan Albu for their support and expert advice.

DEDICATION

To my family

Chapter 1

Introduction

Photodiodes fundamental objective is to receive an optical signal and to transform it into electricity. This capacity has proven to be crucial in many industries and applications. With the recent developments in telecommunication networks, where optical fibers have started to replace copper based establishments in access networks, photodiodes need to match the increasing demand in speed and sensitivity.

We begin this work by introducing passive optical networks, a current favorite in optical access networks, which is therefore an important and defining field of applications for photodiodes. Two available options for photodetection in passive optical networks are pin and avalanche photodiodes. Despite many of their advantages, pin photodiodes seem to be unable to meet the requirements in this field of applications. This makes avalanche photodiodes the promising choice.

In chapter 3 we present the fundamentals and operation principles of avalanche photodiodes. Moreover, important parameters defining its performance and therefore viability are introduced, along with previously utilized methods and ideas to enhance these parameters.

In chapters 4 and 5 analytic and numerical modeling of pin and avalanche photodiode are demonstrated. Chapter 4 is a replication of a previous work on lateral pin photodiode. In chapter 5 we use Lumerical, to simulate and optimize a waveguide avalanche photodiode, with a promising performance. By providing accurate modeling for these devices, improving their performance and fabricating structures with higher quality becomes more achievable.

In chapter 6 we present a device, which is designed in order to be attainable using the fabrication capacity available to our group at the time. We

repeat our methods in chapter 5 to model and predict the performance of this device. We continue by observing the influence of certain design parameters on performance, and finish this section by making optimization suggestions.

Eventually in chapter 7 a summary and conclusion to this work is presented.

1.1 Contribution

In this thesis I first identified the established design themes for avalanche photodiodes and their critical performance parameters. I demonstrated that Lumerical is a viable option to accomplish our aim of effectively modeling avalanche photodiodes; Current, responsivity, multiplication gain, and bandwidth are obtained, where results are in good agreement with reported measurements and our understanding about the operation of avalanche photodiodes. Excess noise factor and other noise parameters are also derived to offer a more complete analysis of the performance.

I then utilized this work to implement and model a design, tailored for a particular fabrication specifications available to our group. After that, different variants of the structure are simulated; The relation between design and performance parameters is illustrated and optimization suggestions are made.

1.2 Thesis Outline

The thesis structure is as follows:

Chapter 2 introduces passive optical networks, their part in telecommunication networks, and their evolution.

Chapter 3 is a study of avalanche photodiodes, how they operate, what is some of their important parameters, and what efforts have been made in order to enhance their operation.

Chapter 4 is replication of a previous work on a lateral pin diode. This chapter offers an analytic modeling, where design parameters are directly related to performance of the device.

Chapter 5 presents modeling of a silicon germanium SACM waveguide avalanche photodiode. The modeling is performed using Lumerical where parameters such as current, responsivity and bandwidth are obtained.

Chapter 6 Demonstrates the simulation and optimization of a device, adjusted to meet certain fabrication specifications.

Chapter 7 provides a brief summary and conclusion of the thesis.

Chapter 2

Passive Optical Networks

For decades, telecommunication networks have been consistently required to develop their capacity for transferring data. This is due to the continuous introduction of new applications with more bandwidth requirements and growth in number of subscribers. In this chapter we introduce passive optical networks and explain their important part in today's telecommunication networks. This provides a clear context on the significance of the designed structure in current technology and highlights its critical performance parameters and what is expected from the device.

2.1 Access Networks

Telecommunication networks can be divided into three parts. Long-haul network, metropolitan area network and access network. Long-haul or backbone networks transfer data traffics over long distances, across countries and continents and can be thousands of kilometers long. Access networks also known as first mile networks provide network for end users, ranging from $0-20$ km. These two networks are connected by the intermediate metropolitan area network which are $10-100$ km long.

In early 1990s Digital Subscriber Line (DSL) was introduced to transfer data in access networks. This technology uses the existing infrastructure for telephone lines and is therefore a copper based network. Since then different variants of DSL has been employed such as Asymmetric Digital Subscriber Line (ADSL) and Very-high-bit-rate Digital Subscriber Line (VDSL). ADSL

managed to support between 1.5 Mbps to 8 Mbps in downstream, and 64 Kbps to 768 Kbps in upstream [45], while VDSL provided a maximum of 52 Mbps in downstream and 26 Mbps in upstream [55].

Despite its utility in the past years, DSL will not be able to keep up with the increasing demand for capacity to transfer data. This is not only due to DSL's bandwidth restriction, but also its limited distance reaching its maximum at 5.5 Km [77].

Optical fiber network is the ideal candidate to meet telecommunication requirements in access networks. By using optical fibers as the medium responsible for transferring data, this network is capable of enhancing the provided service in terms of bandwidth and distance, making it qualified for supporting the next generation services.

Optical networks have several advantages compared to copper-based networks:

- Optical networks can transfer data with higher speed due to their superior bandwidth.
- They can operate over longer distances, due to the smaller attenuation of optical fibers.
- Optical fiber is less susceptible to electromagnetic interference.
- The transferred data is more secure in an optical network and a security breach is easier to detect.

Optical fiber utilizes total internal reflection to propagate light within it. If the angle of the incident light (θ_{in}) inside the fiber is larger than the critical angle (θ_c), it is able to reflect and continue its transmission. Fig. 2.1 demonstrates total internal reflection inside a fiber.

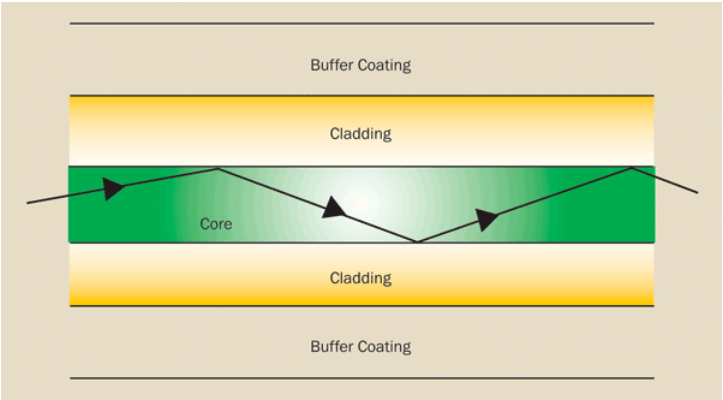

Figure 2.1: Total internal reflection in an optical fiber [4].

Using optical fibers in access networks however, means that the electrical signal needs to be converted to light for transmission and transformed back to electricity when received. Later in this chapter, we introduce the structure that is responsible for conversion of light into electricity and explain how their viability is defined in relation to their utility for optical data communication.

2.2 Optical Access Networks

The optical access network is also referred to as Fiber to the X (FTTX). There are different classifications depending on how close the fiber is to the end user, such as fiber to the node (FTTN), fiber to the curb (FTTC), fiber to the building (FTTB), and fiber to the home (FTTH) (Fig. 2.2).

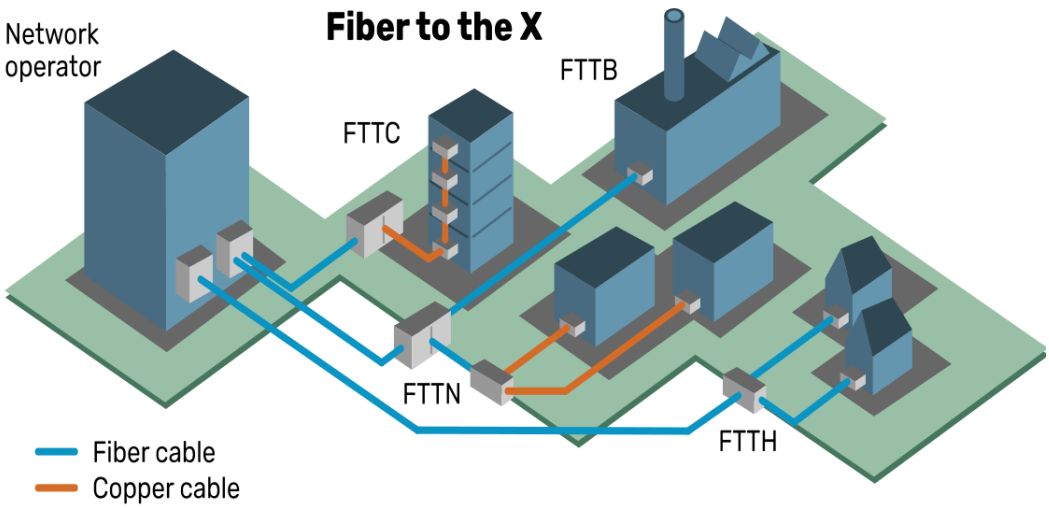

Figure 2.2: Various formats of FTTX [6].

Two main components of an optical access network are Optical Line Terminal (OLT) and Optical Network Unit (ONU). OLT is located in the Central Office (CO) at the service provider's end, and ONU is at the user's side. The continuous transfer of optical signal in access network takes place between OLT and ONU.

OLT interfaces between the long-haul or metropolitan area network and the access network. It is responsible for the bidirectional flow of information in the access network, in downstream and upstream [49]. In downstream, OLT utilizes methods such as TDM, WDM, TWDM, etc. to multiplex data to ONUs over the optical distribution network. In the upstream it receives and separates the data from all ONUs. OLT is responsible for preventing any interference in data transmission and it also has to ensure that the optical power is sufficient to send the data across the network, up to 20 km [49].

The ONU is normally housed in an outdoor equipment shelter, and requires local power source and emergency battery backup [49]. ONU has to interact with optical signal on the access network side and electrical signal

on the user's end. This means that the conversion of optical and electrical signal to each other takes place at ONU.

In a point-to-point (P2P) architecture, where there is a single optical port dedicated to the subscriber, OLT and ONU are the only main components in the access network. However, in a point-to-multipoint (P2MP) configuration, the line is shared between multiple users. This necessitates the inclusion of a third component beside OLT and ONU, called Remote Node (RN).

RN consists of intermediate devices like splitters/combiners, AWGs, Ethernet switches or optical amplifiers, depending on the network architecture [80].

If the equipment used in RN is electrically powered the network is classified as Active Optical Network (AON), otherwise it is a Passive Optical Network (PON) [20]. In a PON, electronically powered devices are only needed at the central office and user's end which drastically reduces the costs for installment and maintenance and improves the reliability of the network. This makes PON the ideal option compared to AON.

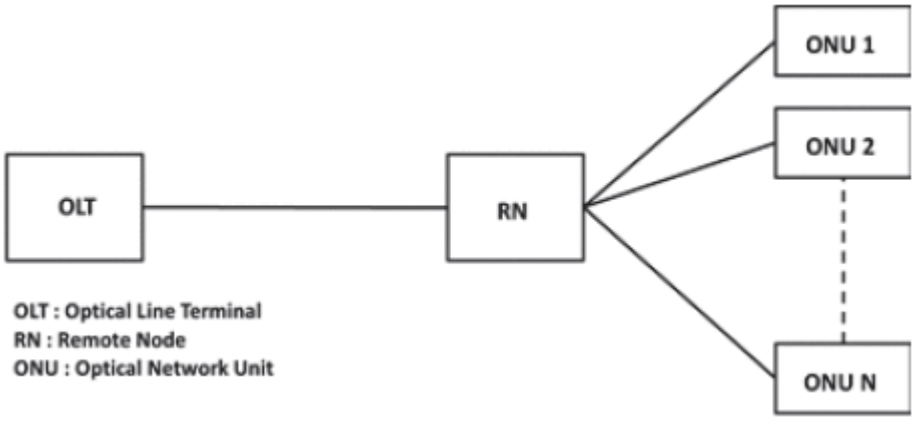

Figure 2.3: Basic representation of a passive optical network [58].

2.3 PON Evolution

Different types of PON have been introduced over the past years as the result of consistent demand for improved performance.

After the initial success of implementing the idea of PON, in 1995 asynchronous transfer mode passive optical network (ATM-PON/APON) was

established as the most promising access technology by FSAN [33]. APON provided 155 Mbps downstream and upstream.

Later the improved version of this model, Broadband PON was introduced, which upgraded the downstream data rate to 622 Mbps.

IEEE 802.3*ah* introduced Ethernet PON (EPON) in 2001 which carries all data encapsulated, in Ethernet frames [19]. EPON supports up to 1 Gbps in downstream and upstream [69].

Around the same time in 2003, the first recommendation for general features of Gigabit-capable PON (GPON) was proposed by FSAN, with a maximum of 2.4 Gbps downstream and upstream [19].

EPON and GPON are superior to APON/BPON in terms of reach, bandwidth and number of supported ONUs [19]. It should be noted that GPON demonstrates certain advantages compared to EPON such as splitting ratio, line rate, and bandwidth efficiency [19].

GPON capacity was later improved by the introduction of 10G-PON. Asymmetric 10G-PON classified as XG-PON1 provided 10 Gbps downstream and 2.5 Gbps upstream while symmetric 10G-PON known as XG-PON2, provided 10 Gbps downstream and upstream [48].

IEEE also continued their development by presenting 10 Gigabit Ethernet passive optical network (10G-EPON), offering 10 Gbps in downstream and 10 and 1 Gbps in upstream [84].

At the moment NG-PON2 defined by ITU-T is the next step in fiber access evolution. NG-PON2 has 40 Gbps capacity and utilizes both time and wavelength domains [63].

2.4 Photodetection in PON

Once the optical signal is delivered, it needs to be converted back to electricity, so that the information can be processed. This transformation is performed by the photodiodes, which need to match the network requirements in their performance.

Photodiode's viability is determined by several factors including their speed, efficiency, and optical detection capacity. Parameters such as sensitivity, responsivity, and bandwidth are introduced to make the evaluation of these important qualities possible.

In passive optical networks, pin and avalanche photodiodes are two available options to perform photodetection in the receiving module. Compared

to avalanche photodiodes (APDs), pin devices are generally less costly and their fabrication is simpler; however, their sensitivity, which represents the minimum power required for the signal to be detected, is generally inferior to APDs. The higher sensitivity in APDs is due to their internal gain amplification which doesn't exist in pin photodiodes. Compensating lower sensitivity in the photodiode by increasing the transmitting power is costly [15]. Moreover, using an amplifier in combination with the photodiode will introduce Johnson noise from the equivalent resistance due to the electronics [32]. This makes avalanche photodiodes a promising choice for this application.

Traditionally, group III-V materials such as InP have been used for APDs, which have demonstrated higher sensitivity compared to pin photodiodes ($\simeq$ 10 dBm) [47]. With the demand in bandwidth increasing and the required bit rates exceeding 10 Gb/s, mentioned APDs no longer satisfy the performance criteria as their gain-bandwidth drops for higher bit rates.

Si-Ge APDs demonstrate higher sensitivity and gain-bandwidth for these bit rates. Silicon is a better medium for avalanche multiplication due to its lower ionization coefficient ($\simeq 0.1$). Also, germanium is a viable absorbing material in telecommunication wavelengths ($\simeq 1.3{-}1.55\mu m$). Moreover, using a silicon based photodiode, improves its compatibility with other components and makes the device mass production easier.

One of the main challenges for these structures is obtaining high quality growth of germanium on silicon which strongly determines the quality of the device. Si-Ge APDs demonstrate higher dark current compared to III-V APDs which is another issue that needs to be addressed. Higher dark current is mainly due to the lattice mismatch between Ge and Si ($\simeq 4\%$) [47]. Integrating Si-Ge APD in a waveguide structure have shown to result in dark current and responsivity levels, comparable to other APDs, minimizing the structure's flaws [46].

In next chapters we introduce basics of pin and avalanche photodiodes and continue by modeling their operation.

Chapter 3

Avalanche Photodiode

As mentioned earlier, APDs are an ideal option for transforming the optical signal into electricity compared to pin photodiodes and therefore, this work focuses on design and optimization of an APD. In this chapter we explain how an avalanche photodiode works and what are the most important parameters defining its performance. We will also present the major design approaches, made in the recent years to enhance the quality of avalanche receivers.

3.1 Impact Ionization

APDs key advantage to pin photodiodes, is their superior sensitivity which is due to their internal gain mechanism.

In a photodetector, photons incident on the device generate electron-hole pairs in the absorbing layer, given that photons have enough energy. For an avalanche photodiode, in the presence of a sufficiently large electric field, a free carrier's energy can exceed the band gap energy and therefore, is capable of generating an electron-hole pair, in a process which is called impact ionization. The consecutive generation of electron-hole pairs may repeat several times, meaning that an incident photon can initiate the generation of multiple electron-hole pairs, as opposed to only one in case of pin photodiodes. This is the origin of the internal gain for APDs, which is lacking in pin photodiodes.

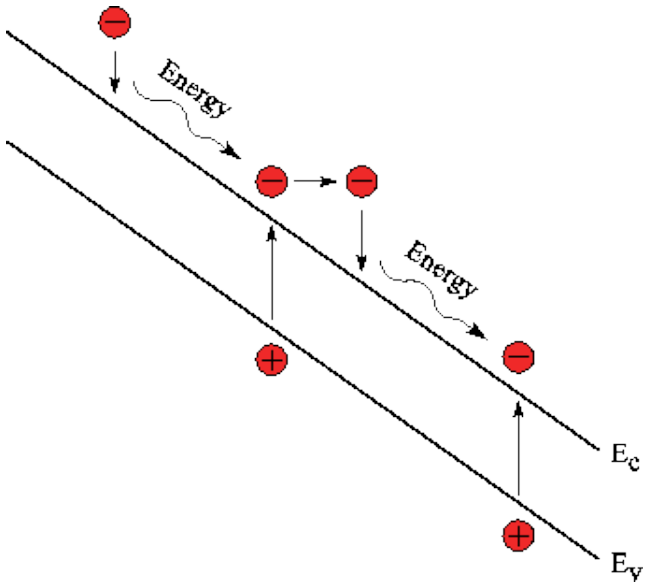

Figure 3.1: An initial electron creating an electron-hole pair. Due to presense of high electric field the secondary carriers can gain enough energy to initiate more generations. [3]

The ionization rate is defined as the number of electron-hole pairs generated by a carrier per unit distance travelled [56]. Impact ionization rate for electrons is represented by α, and impact ionization rate for holes is represented by β. It can be shown that assuming equal effective masses for electrons and holes, the minimum energy required for the particle to initiate an ionization is $1.5 \cdot E_g$ where E_g is the bandgap [56].

In a local model for impact ionization, the ionization rates only depend on the local electric field [56] [61]. This relation can be expressed as [21]:

$$\alpha = ae^{-b/E} \tag{3.1}$$

$$\beta = ce^{-d/E} \tag{3.2}$$

where a,b,c, and d are ionization coefficients and E is the electric field. Higher electric fields help the carriers to gain the required energy for ionization over a smaller distance, and therefore increase the ionization rate.

The ratio between electron and hole impact ionization rates is an important parameter characterizing the performance of the avalanche photodiode.

This ratio is referred to as the impact ionization ratio, or k-value:

$$k = \frac{\beta}{\alpha} \tag{3.3}$$

For a better performance, it is desirable to have most of the carriers entering the high field region, be of the more strongly ionizing type [60]. Meaning that when $\alpha > \beta$ a small k-value ($\alpha >> \beta$), and for $\alpha < \beta$ a large k-value ($\alpha << \beta$) is preferred. In sections 3.4 and 3.5 the critical influence of k-value on noise and bandwidth is addressed.

3.2 Multiplication Gain

Each avalanche process sequence is initiated by the generation of an electron-hole pair. Being influenced by the local electric field, the generated electron and hole will move in opposite directions, where the electron will go through an average of $\alpha \cdot dx$ and the hole will go through an average of $\beta \cdot dx$ impact ionizations. Each of the carriers generated secondarily, can initiate an avalanche sequence themselves. Therefore, the average total number of electron-hole pairs generated by an initial pair formed at x is given by [60]:

$$M(x) = 1 + \int_0^x \alpha M(x') \cdot dx' + \int_x^w \beta M(x') \cdot dx' \tag{3.4}$$

Where w is thickness of the multiplication layer and $0 < x < w$. By solving this equation, $M(x)$ is eventually described by:

$$M(x) = \frac{exp[-\int_x^w (\alpha - \beta) dx']}{1 - \int_0^w \alpha \cdot exp[-\int_{x'}^w (\alpha - \beta) dx''] dx'} \tag{3.5}$$

3.3 Dark Current

Dark current is the current that exists in the device even when there is no illumination. It is important to reduce the dark current, as the shot noise associated with it will limit the sensitivity of the photodiode. In section 3.10 we illustrate how dark current influences the noise current and the sensitivity of the device.

To obtain lower dark currents, using high quality materials and fabrication process is even more important in APDs compared to pin photodiodes,

given the higher electric field [59]. There are two components to dark current in an APD, the leakage current flowing through the periphery (I_{du}), and the multiplied component which flows through the device (I_{dm}) [13]. Therefore, the total dark (I_d) current can be written as:

$$I_d = I_{dm} \cdot M + I_{du} \tag{3.6}$$

Diffusion, generation-recombination, and band-to-band tunneling, are the three main contributors to the dark current [29]:

Diffusion

The dark current caused by diffusion, is due to the thermally generated minority carriers diffusing into the depletion region and towards the opposite side. This component of dark current can be written as:

$$I_{diff} = I_s(e^{qV/kT} - 1) \tag{3.7}$$

where I_s is the saturation current, V is the applied reverse bias voltage, K is the Boltzmann constant, and T is the temperature in Kelvin. I_s is given by:

$$I_s = q{n_i}^2 A(\sqrt{\frac{D_n}{\tau_n}}\frac{1}{N_A} + \sqrt{\frac{D_p}{\tau_p}}\frac{1}{N_D}) \tag{3.8}$$

where n_i is the carrier concentration, A is the area of depletion region boundary, D_n and D_p are minority carrier diffusion constants, τ_n and τ_p are minority carrier diffusion lifetime, and N_A and N_D are the doping concentration in p and n region.

Generation-Recombination

This component is due to generation-recombination (GR) occurring at traps near the middle of the band gap. Dark current due to GR is given by:

$$I_{gr} = \frac{qn_i AW}{\tau_{eff}}(e^{qv/2kT} - 1) \tag{3.9}$$

W is width of the depletion region and τ_{eff} is the effective carrier lifetime. Given that $I_{diff} \propto {n_i}^2 \propto e^{-E_g/kT}$ and $I_{gr} \propto n_i \propto e^{-E_g/2kT}$, it is expected for the GR current to be dominant in lower temperatures and the diffusion current to be more significant in higher temperatures.

Band-to-band Tunneling

There is a high possibility for band-to-band tunneling when excessively high electric field is applied to materials with low band gap. For a direct band-gap semiconductor, dark current resulting from band-to-band tunneling (I_{tun}) is calculated by:

$$I_{tun} = \xi \cdot e^{\frac{\theta \cdot {m_e}^{1/2} {E_g}^{3/2}}{qhE_m}} \tag{3.10}$$

Where m_e is the free electron mass, E_g is the bandgap, E_m is the maximum electric field, and θ is given by:

$$\theta = \alpha(\frac{m_c}{m_0})^{1/2} \tag{3.11}$$

α depends on the shape of the tunneling barrier, and m_c is the effective mass of electron. ξ is also given by:

$$\xi = \frac{2{m_e}^{1/2} \cdot q^3 \cdot E_m \cdot V \cdot A}{h^2 {E_g}^{1/2}} \tag{3.12}$$

The only temperature dependent parameter for I_{tun} is E_g, so it has a considerably less dependency on temperature, compared to I_{diff} and I_{gr}.

3.4 Excess Noise

Another factor that degrades the performance of an avalanche photodiode is the excess noise. An avalanche photodiode can provide an improved signal-to-noise ratio, if the excess noise which is due to random fluctuations of gain doesn't become too excessive [60]. This noise is represented in terms of excess noise figure which is given by [60]:

$$F(M) = M \cdot k + (1 - k) \cdot (2 - \frac{1}{M}) \tag{3.13}$$

where M is the mean gain. Eq. 3.13 shows that excess noise increases for larger k-values and larger multiplication gains (Fig. 3.2). This makes materials such as silicon a more ideal avalanche medium due to their lower k.

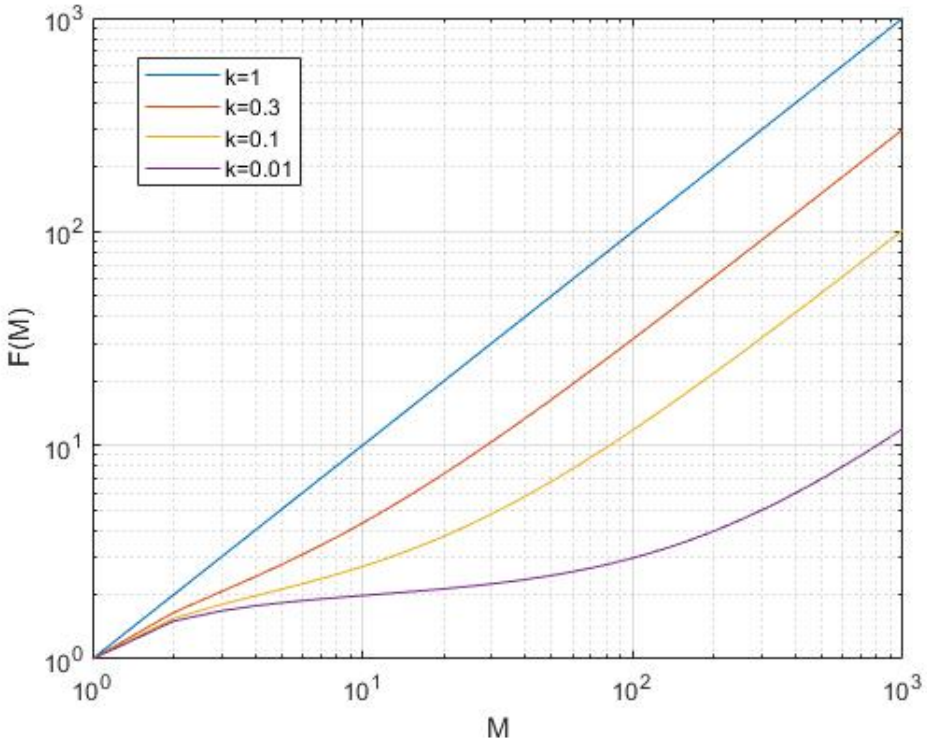

Figure 3.2: Theoretical excess noise as a function of multiplication gain for different k-values [60].

It should be noted that Eq. 3.13 is based on the local model of impact ionization and assumes uniformity of the multiplication region [68]. In section 3.6 we describe how changing the thickness of the avalanche layer, can impact the effective k-value and therefore, the excess noise. Also in section 3.10, we show the influence of excess noise on sensitivity and the optimal operation point.

3.5 Bandwidth

The bandwidth is one of the most important parameters that characterizes the performance of photodiodes. It demonstrates how fast the photodiode can transform the optical signal into electricity, effectively. The 3 dB bandwidth represents the frequency in which the output power falls to half of its

DC value [62]. There are different factors that limit the speed of the device:

RC Limitation

The bandwidth associated with RC limitation is given by:

$$f_{RC} = \frac{1}{2\pi RC} \tag{3.14}$$

Where $R = R_S + R_L$, R_S being the series and R_L being the load resistance, and C is the junction capacitance.

Transit time

Similar to a pin photodiode, generated carriers need to travel across the device and the depletion region in an avalanche photodiode. This process limits the speed response, especially in low gain regime.

The main challenge in addressing the transit time limitation to the bandwidth, is the existing trade-off with responsivity.

The transit time can be reduced by scaling down the thickness of the absorption layer [51] [22]. This will also decrease the probability of impact ionizations in the absorbing layer, which influences the gain-bandwidth product in a negative way [79].

On the other hand, reducing the thickness of the absorbing layer, can lower the asborption of light, and therfore the responsivity. For example the quantum efficiency of a normal incidence InGaAs-InAlAs SACM APD, is 13% higher with a $1.5\mu m$ InGaAs absorption region, compared to a $1\mu m$ one [24].

There are different approaches to improve the responsivity to allow for a thinner absorbing layer. One strategy is to use resonant cavity enhanced (RCE) APDs [53] [26]. This design generally utilizes two mirrors to enhance the amplitude of the internal optical field [26] (Fig. 3.3).

Another technique reported, is the implementation of edge-illuminated refracting facet (RF) [42] [41] [31] [30]. In this design, the incident light is refracted at an angled facet and then absorbed in the absorption layer. Since the light passes through the absorbing layer with a certain angle, the effective absorption length increases [30].

Using a waveguide structure is also an effective method where the incident light is perpendicular to the direction of carrier transit. Waveguide structures for APDs is later explained in section 3.8.

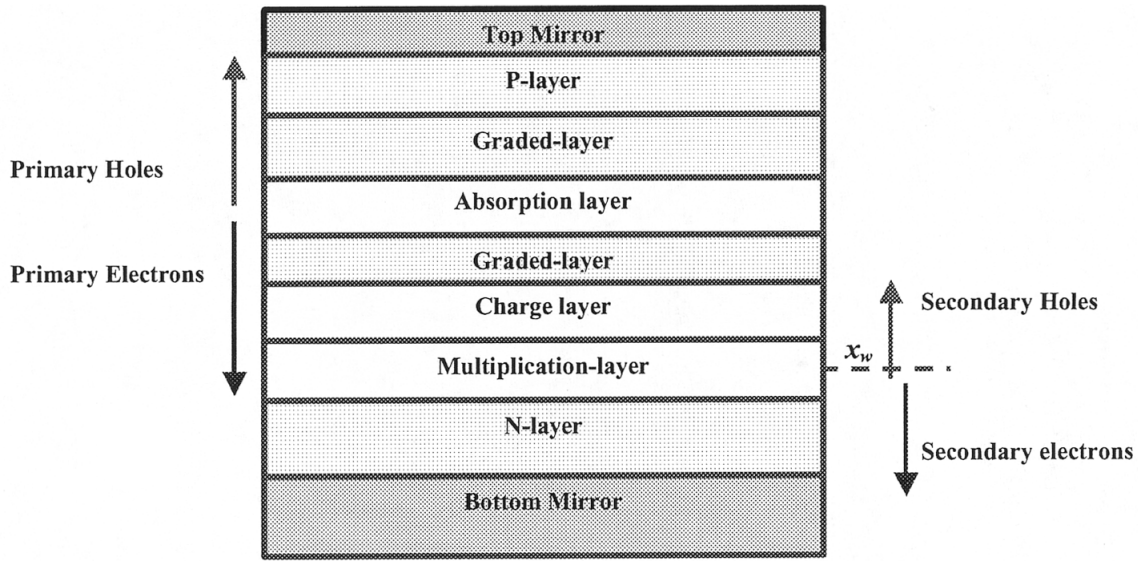

Figure 3.3: Schematic representation of RCE-SACM APD [26].

Avalanche build-up time

The avalanche build-up time is the time required for the multiplication process, which increases with increasing gain [38]. For $M > 1/k$ the effective transit time (τ_1) can be approximated by [27]:

$$\tau_1 = N(k) \cdot \tau \tag{3.15}$$

where N(k) is a function of k, varying from 1/3 at $k = 1$, to 2 at $k = 0.001$, and τ is the actual carrier transit time across the multiplication region. For $M < 1/k$, transit time remains the significant limitation on the bandwidth [27].

Fig. 3.4 demonstrates how the avalanche build-up limits the bandwidth as the gain increases. The bandwidth begins to drop as the effect of avalanche build-up time becomes more significant, and then decreases linearly as M exceeds $1/k$. As expected, the decline in bandwidth begins at higher gains as the k-value decreases, which results in a higher gain-bandwidth product.

The trade-off between gain and bandwidth, caused by the build-up time, translates into a trade-off between sensitivity and bandwidth, since APD owes its superior sensitivity to presence of the multiplication mechanic [39].

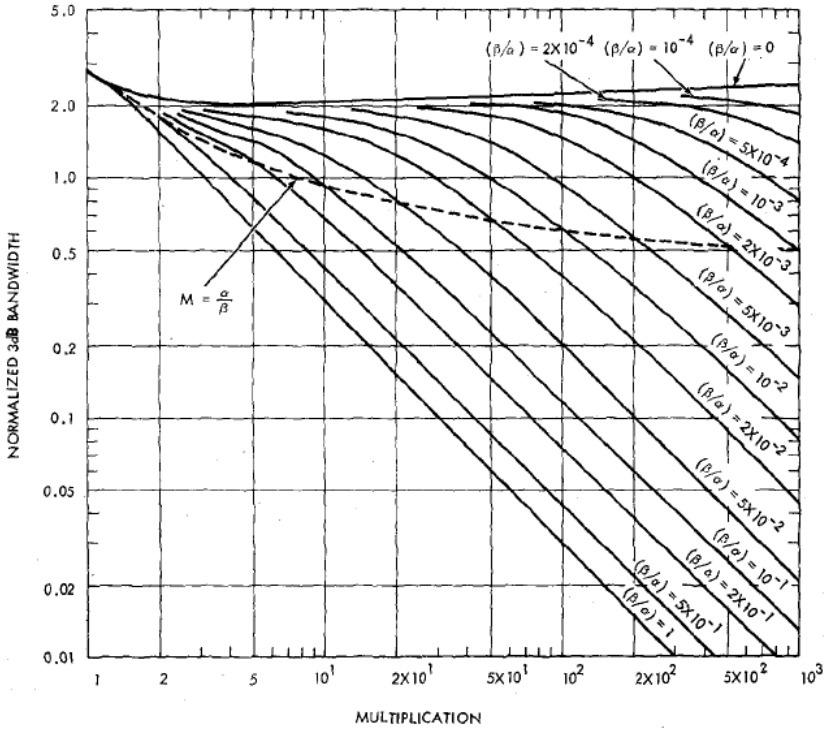

Figure 3.4: Calculated 3 dB bandwidth as a function of multiplication gain, for different k-values. The dashed line indicates where $M = 1/k$ (edited). [27]

3.6 Sub-micron Scaling of the Multiplication Layer

One approach that has been effective in reducing the multiplication noise and enhancing the gain-bandwidth product, is reducing the thickness of the multiplication layer below 1 micron. The success of this approach, which has been reported for various materials such as InP, GaAs, InAlAs, Si, AlGaAs, SiC, GaP, and GaInP [18], is due to the non-local nature of impact ionization.

The distance required for carriers to gain the required energy for impact ionization is called "dead space". By making the multiplication layer thickness small enough, the dead space magnitude becomes comparable to the multiplication region. This will reduce the number of impact ionization sequences that result in a gain significantly higher than the average gain.

Therefore, the gain becomes more deterministic, resulting in a lower effective k-value and excess noise [82].

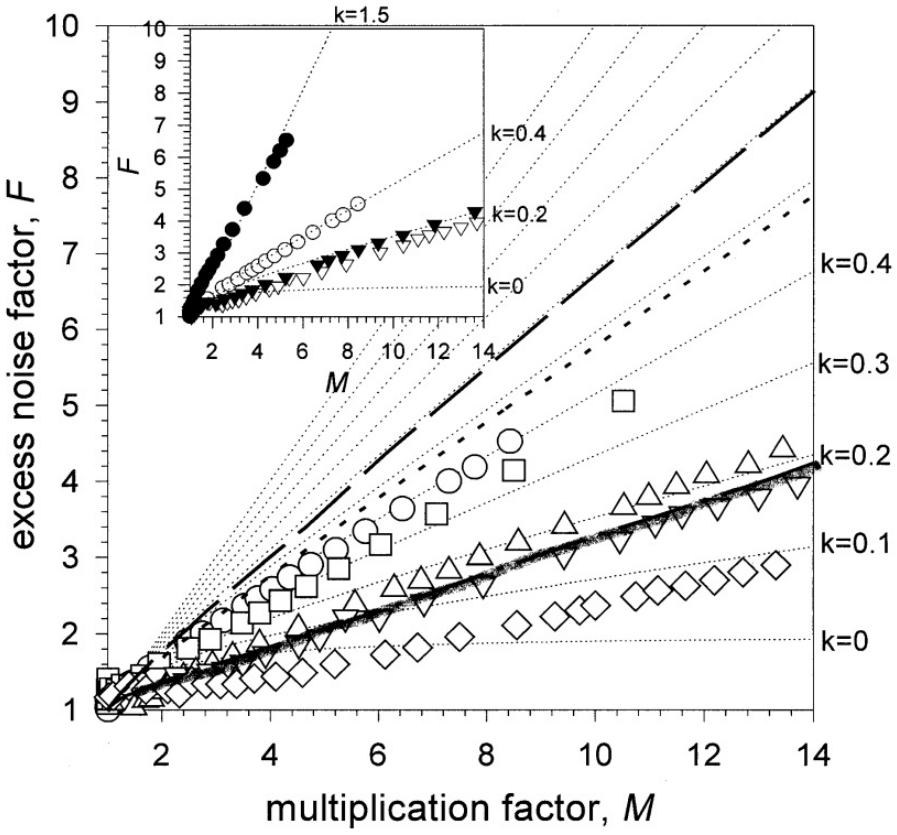

Figure 3.5: Measured (symbols) and calculated (lines) excess noise factors for different multiplication layer thickness (w) as a function of multiplication factor. w = 850 nm (○, dashed line), w = 490 nm (□, dotted line), w = 90 nm (△, dash-dotted line), w = 49 nm (▽), and w = 26 nm (◇). The inset presents the excess noise factors for electron-hole initiated multiplication (black symbols) and purely by electrons initiated multiplication for w = 850 nm (●, ○) and w = 49 nm (▼, ▽). Curves for different k-values are also represented as dotted lines. [73]

In an interesting work reported by Chee Hing Tan et al., gain and excess noise factor was measured for AlGaAs avalanche photodiodes with different multiplication layer thickness [73]. Excess noise factor was calculated and

measured for multiplication layers, ranging from 26 nm to 850 nm, and then compared to calculations for different k-values between 0 and 1 (Fig. 3.5). By applying this design approach, at M≃ 15.5 an outstanding excess noise factor of ≃ 3.3 was demonstrated for a multiplication layer of 26 nm.

3.7 Impact Ionization Engineering (I^2E)

As mentioned earlier using a material with low k-value for multiplication layer, is of great importance to obtain desirable performance regarding noise and bandwidth.

Another approach to enhance the performance of an APD, is utilizing a design technique referred to as impact ionization engineering (I^2E). I^2E structures provide greater localization to impact ionization events, which makes the multiplication process more deterministic, and therefore decreases the excess noise. This is achieved by abrupt change in required energy for impact ionization, as carriers move from materials with wide band gap to materials with narrow band gap [18].

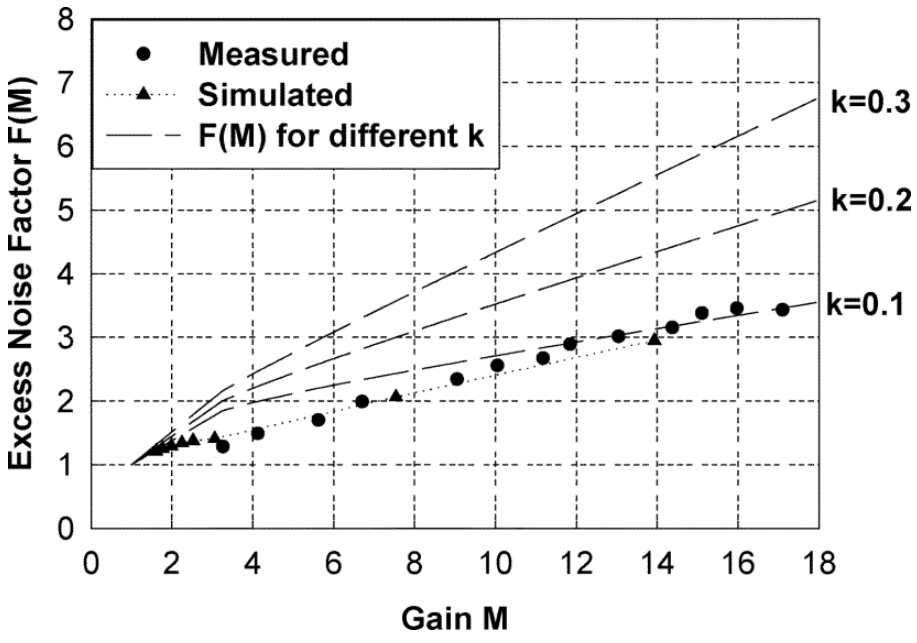

Figure 3.6: measured and simulated excess noise factor as a function of gain. [25]

The effectiveness of this approach has been demonstrated in several works, using material combinations such as GaAs/AlGaAs and InAlAs/InAlGaAs [82] [52] [37] [25]. For instance, Duan et al. reported an I^2E SACM APD with an $In_{0.52}Al_{0.48}As - In_{0.53}Ga_{0.17}Al_{0.3}As$ multiplication region [25]. Simulated and measured results for this structure is shown in Fig. 3.6. As demonstrated, by utilizing impact ionizing engineering, the structure presents an effective k-value of 0.1.

As presented in 3.6, measurements and calculations suggest that, decreasing the multiplication layer thickness, decreases the effective k-value and therefore the excess noise factor. Also having the multiplication initiated only by electrons, result in a better performance compared to mixed injection (electrons and holes).

3.8 Waveguide Integration

An effective design approach is the integration of waveguide structure. It addresses the trade-off between bandwidth and responsivity since the incident light is perpendicular to the direction of carrier transit, and responsivity becomes a function of device length rather than thickness [51].

Waveguide structure is also a decent option for germanium based photodetectors due to its compact size [46] [12] [78]. This can reduce the dark current, which is a known issue for germanium photodiodes [12].

Depending on the utilized architecture, the light might directly enter the absorbing layer, or be coupled by evanescent wave coupling. Different designs are shown in Fig. 3.7 and 3.8.

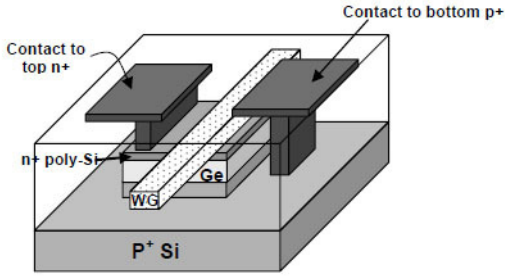

Figure 3.7: Ge/Si waveguide pin photodetector. The waveguide is placed on top of the photodetector and light is coupled using evanescent coupling. [12]

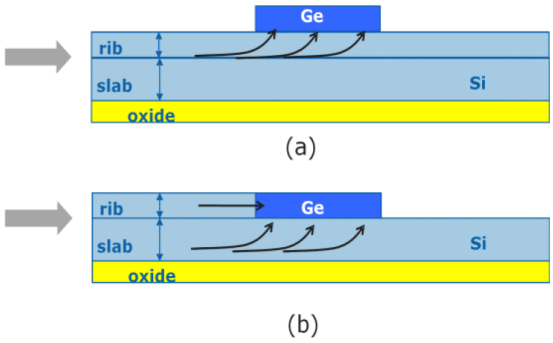

Figure 3.8: Ge/Si waveguide avalanche photodetector. a) evanescent-coupled and b) butt-coupled device. [46]

3.9 SACM APD

The early generation of avalanche photodiodes operated as strongly reverse biased pin diodes. In these devices the absorption and multiplication took place in the same layer. The absorbing material needs to have a sufficiently small bandgap to absorb the incident photons, while effective multiplication requires significantly high electric fields. This leads to strong band-to-band tunneling which causes high dark current.

To address this issue, the absorption and multiplication layers were then separated in SAM (Separate Absorption Multiplication) devices where the high electric field could be limited only to the multiplication layer. Therefore materials with wider bandgaps could be used in this layer to prevent band-to-band tunneling.

As stated before, reducing the thickness of multiplication layer can enhance the performance of the device by improving sensitivity and bandwidth, which increases the electric field within the structure. This demands a field separation between absorption and multiplication layers, introduced by charge layer presented in SACM (seperate absorption charge multiplication) APDs.

3.10 Sensitivity and Optimal Operation Point

Avalanche photodiodes are known to be a promising choice in optical communication networks, due to their capacity to demonstrate higher sensitivity compared to pin photodiodes. Although achieving higher sensitivity in APDs is possible as a result of the internal gain mechanism, the excess noise associated with gain has a negative impact on sensitivity. We proceed to investigate the existing trade-off between sensitivity and multiplication gain, which is necessary in order to obtain the optimal settings for the device.

Sensitivity in a receiver is defined as the signal corresponding to a predefined signal-to-noise ratio, SNR [67]. When operating, the photodiode generates a current i which fluctuates above and below its average $\bar{i}$. These fluctuations are regarded as noise and emerge as a results of several factors such as photon noise, photoelectron noise, gain excess noise, and receiver circuit noise [67]. SNR of the current i is given by:

$$SNR = \frac{\bar{i}^2}{{\sigma_i}^2} \tag{3.16}$$

where σ_i is the standard deviation. SNR is related to gain and excess noise factor through the following relation [67]:

$$SNR = \frac{M^2\bar{m}^2}{M^2F\bar{m} + {\sigma_q}^2} \tag{3.17}$$

where σ_q is a circuit noise parameter and $\bar{m}$ is the mean number of detected photons given by:

$$\bar{m} = \frac{\eta\Phi}{2B} \tag{3.18}$$

Here, Φ is the mean photon flux, and η and B are quantum efficiency and bandwidth of the photodiode. Eq. 3.17 suggests a negative influence of excess noise on sensitivity, which is expected. We can rewrite Eq. 3.17 by replacing F, using Eq. 3.13 [67]:

$$SNR = \frac{M^2\bar{m}}{kM^3 + (1-k)(2M^2 - M) + {\sigma_q}^2/\bar{m}} \tag{3.19}$$

Using this equation, we plot SNR as a function of multiplication gain, for $\bar{m} = 1000$ and $\sigma_q = 500$, and for different k-values (Fig. 3.9) [67].

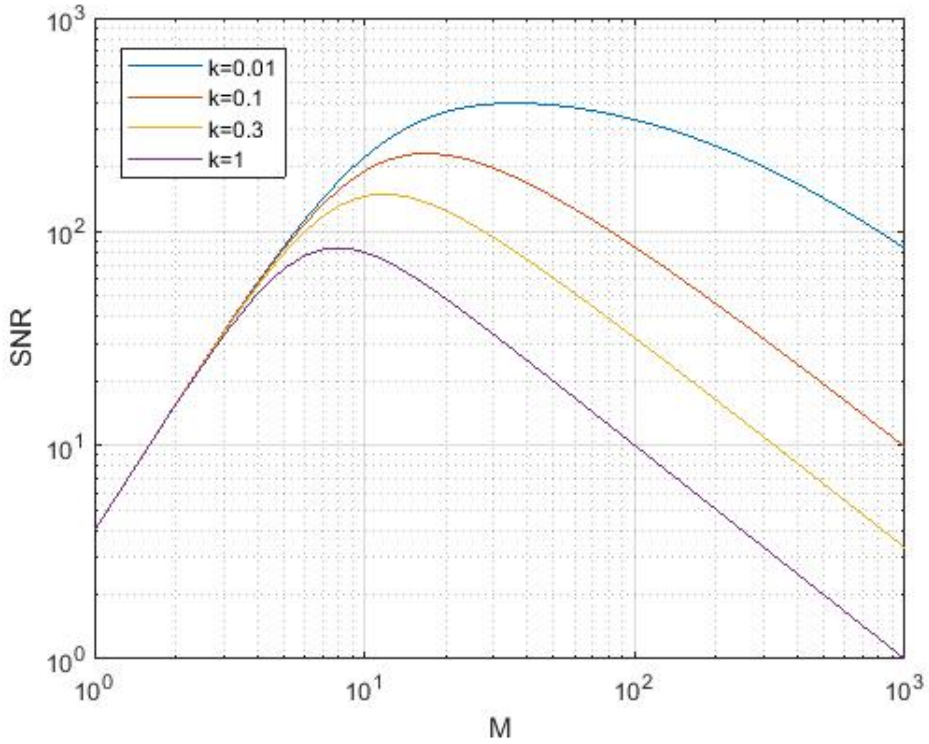

Figure 3.9: Theoretical SNR as a function of multiplication gain for different k-values. [67]

Fig. 3.9 shows that for practical k-values ($k \neq 0$) the SNR initially increases for larger gains, but then reaches its maximum and drops thereafter. This matches our expectations, considering the relation between multiplication gain and excess noise, as established in section 3.4. Therefore, the optimal multiplication gain is well below its maximum.

Fig. 3.9 also illustrates that attaining a higher sensitivity is possible by having a smaller k-value.

3.11 Noise Equivalent Power

Shot noise, bulk leakage current, and Johnson noise contribute to noise in avalanche photodiodes [34]. Noise equivalent power (NEP) is defined as the incident signal power, required to obtain a signal equal to the noise in a one

Hz bandwidth [66]. NEP for a stand-alone APD is given by:

$$NEP = \frac{\sqrt{S}}{R(\lambda) \times M} \tag{3.20}$$

Where $R(\lambda)$ is the unity-gain responsivity at wavelength λ and S is the noise power spectral density given by:

$$S = 2 \cdot q \cdot I_1 \cdot M^2 \cdot F \tag{3.21}$$

Here, q is the electron charge and I_1 is the total current before multiplication. As expected, S and therefore noise equivalent power increase for larger excess noise factors. Consequently, a lower NEP will be maintained for lower k-values and multiplication gains. Fig. 3.10 illustrates the dependency of NEP on multiplication gain and k-value, given $R = 0.8$ A/W and $I_1 = 1nA$.

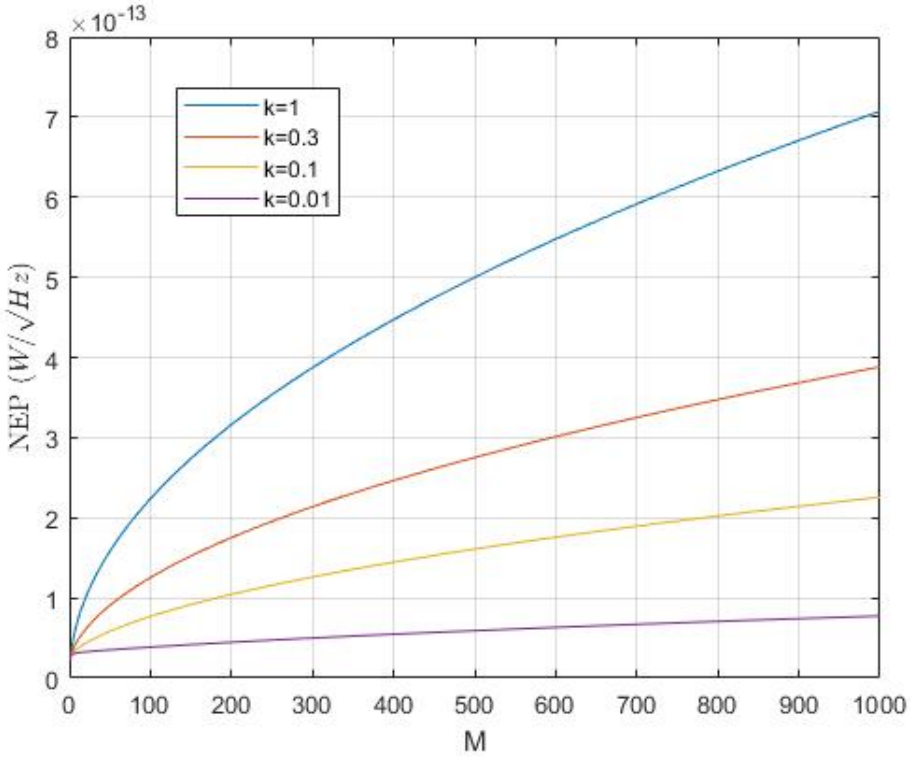

Figure 3.10: Theoretical NEP as a function of multiplication gain for different k-values [2]. R= 0.8 A/W, $I_1 = 1nA$.

Noise equivalent power is also dependent on wavelength, due to the responsivity being wavelength dependent [5]. The minimum NEP is attained for the wavelength with highest responsivity [5].

Chapter 4

Lateral PIN Photodiode

4.1 Introduction

In this chapter we summarize and replicate a previously performed analytic modeling of a lateral pin photodiode [9] [10] [11]. We investigate the relation between design and performance parameters in this structure and study what adjustments are necessary in dimensions, doping, and applied voltage, in order to obtain the intended performance.

4.2 Structure

The device we are analyzing is a thin-film SOI lateral multifinger (i.e. alternating *pini...nip* regions) photodiode [11]. Schematic of one finger (*pin*) is presented in Fig. 4.1. In this configuration the intrinsic region, low doped silicon, is located between highly doped p and n regions. The three regions are formed on a buried oxide (BOX) layer which prevents the slow vertical diffusion of carriers generated under the depletion region in the Si substrate. Light is incident from top which passes through a layer of SiO_2 before reaching the i region and the photogenerated current is collected using electrodes, placed on p and n regions.

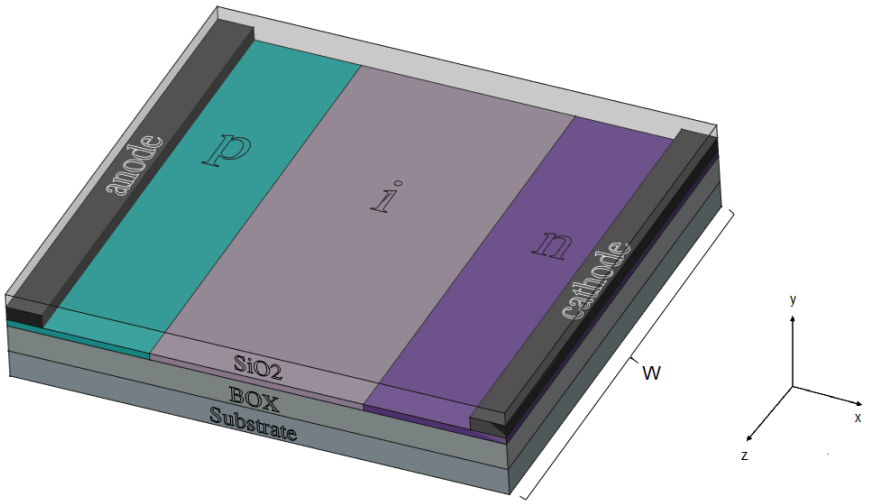

Figure 4.1: lateral PIN photodiode, 3D view.

4.3 Quantum Efficiency

Photodetectors are used in communication networks to receive and detect optical signals and interpret the input by transforming it to electrical signal. The efficiency of this process determines the quality of the designed device and its viability, which is addressed using External Quantum Efficiency (EQE), also known as incident photon to current efficiency (IPCE). EQE is the ratio of output photocurrent density (in electrons per unit area and time) to the intensity of incoming monochromatic light in photons per unit area and time [16]. With a known radiant power input P_{in} (in watts) and output photocurrent I_{ph} (in amperes), External Quantum Efficiency is given by [83]:

$$EQE = \frac{I_{ph} \cdot h \cdot c}{P_{in} \cdot n \cdot q \cdot \lambda} \tag{4.1}$$

where h is Planck's constant ($\simeq 6.62 \times 10^{-34} m^2 kg/s$), c is the velocity of light ($\simeq 3 \times 10^8 m/s$), n is the refractive index of air, q is the electron charge ($\simeq 1.6 \times 10^{-19} C$), and λ is wavelength of the incident light in nm. EQE indicates what portion of incident photons, are converted to electrons and then collected at electrodes:

$$EQE = \frac{N_{collected}}{\phi_{incident}} \tag{4.2}$$

where $N_{collected}$ is number of charge carriers collected at electrodes per unit time t, and $\phi_{incident}$ is number of photons incident on the device per unit time. In this report, the evaluation of this criteria has been divided into three parts, each part describing an independent factor that contributes to the drop of efficiency:

1) The conversion of light into electricity happens in the absorption layer. Photons excite electrons and generate electron-hole pairs, which when collected at the electrodes will result in electrical current. Generated holes and electrons are prone to recombination in their way from the intrinsic region to the electrodes, which will result in a decreased generated current. In section 4.3.1 we address the efficiency of this process by introducing Internal Quantum Efficiency (IQE) and explaining how it relies on different design parameters.
2) The incident light needs to be absorbed in order to contribute to the conversion process. In section 4.3.2 we discuss how the amount of absorbed light depends on the design of the structure and the optical properties of certain layers.
3) The pin device doesn't only consist of intrinsic region, meaning that light is also incident on areas which are not photosensitive. This consideration is implemented in section 4.3.3, where its dependency on design and its effects on performance is investigated.

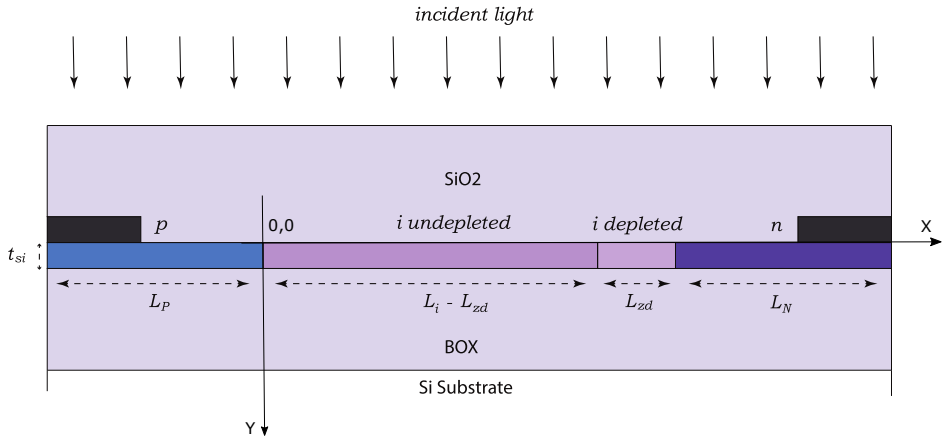

Figure 4.2: lateral pin photodiode, side view.

4.3.1 Internal Quantum Efficiency (IQE)

Internal Quantum Efficiency, also referred to as absorbed photon to current efficiency (APCE) is an internal measure to study the physics of charge generation and transport in devices [16], and is defined as the number of electrons (or holes) collected per absorbed photon [76]:

$$IQE = \frac{N_{collected}}{\phi_{abs}} \tag{4.3}$$

where $N_{collected}$ is number of collected carriers per unit time and ϕ_{abs} is number of absorbed photons in the intrinsic region per unit time. Absorbed photons generate electrons, which travel to the electrodes even without applied external voltage and produce photocurrent when collected.
An IQE of unity indicates that all generated electrons have avoided recombination in their path, and are therefore collected at the electrodes.
We can replace ϕ_{abs} with $N_{generated}$, total number of photo-generated electrons per unit time. We proceed to rewrite Eq. 4.3:

$$IQE = \frac{I_{ph}}{q \cdot N_{generated}} \tag{4.4}$$

The amount of photo-generated current in p and n regions is negligible, because generated carriers in these regions have bad life time due to high doping and the few generated carriers will recombine quickly [10] [65]. Therefore, almost all of the electrons are generated in the intrinsic region, meaning that $N_{generated}$ corresponds to generation of electrons in the intrinsic region.

We introduce $G(x, y, z)$, number of photo-generated electrons per unit volume and time ($m^{-3}s^{-1}$). Given the uniformity of incident light, generation is considered constant along x and z direction. Therefore it can be presented as $G(y)$, demonstrating the dependency of generation on y. Thereafter, $N_{generated}$ is given by:

$$N_{generated} = L_i \cdot W \int_0^{t_{si}} G(y) \cdot dy \tag{4.5}$$

where L_i is length of the intrinsic region, W is width of the device ($\simeq 75\mu m$), and t_{si} is the thickness of the absorbing layer ($\simeq 80nm$). Non-uniformity of generation along the y direction can be represented by G_n, defined as number

of photo-generated electrons per unit volume and time, averaged along the y direction.

$$G_n = \frac{1}{t_{si}} \int_0^{t_{si}} G(y) \cdot dy \tag{4.6}$$

meaning that Eq. 4.5 is now:

$$N_{generated} = G_n \cdot L_i \cdot W \cdot t_{si} \tag{4.7}$$

$W \cdot t_{si}$ is the area of p/i and i/n regions interfaces which we replace with A:

$$A = W \cdot t_{si} \tag{4.8}$$

Noting that total photo-generated current density (J_{ph_t}) is given by:

$$J_{ph_t} = \frac{I_{ph}}{A} \tag{4.9}$$

Eq. 4.4 can be written as:

$$IQE = \frac{J_{ph_t}}{q \cdot G_n \cdot L_i} \tag{4.10}$$

It is the generation in un-depleted and depleted regions that contribute to the total photo-generated current density. J_{ph_t} can therefore be described as sum of current density evaluated at the depleted and un-depleted region interface $J_{ph}(x = L)$, plus the total photo-generated current density in the depleted region:

$$J_{ph_t} = J_{ph}(L) + q \cdot G_n \cdot L_{zd} \tag{4.11}$$

where L_{zd} is length of the depleted region and an IQE of unity is assumed for this part. $J_{ph}(L)$ and L_{zd} need to be determined before we can derive IQE as a function of design parameters. We start by focusing on the depletion region and deriving L_{zd} as a function of doping levels and applied bias voltage in section 4.3.1. In section 4.3.1 we study the carrier concentration and current density in the un-depleted region of absorbing layer in order to calculate $J_{ph}(L)$.

Depletion Region

In a pin photodiode an intrinsic semiconductor is sandwiched between heavily doped p+ and n+ regions. The intrinsic region in fact corresponds to a

p- doping of about $10^{-15} cm^{-3}$ and forms a pn junction with the n region followed by emergence of depletion region [10]. Total negative space charge per unit area in the p-side will precisely equal the total positive space charge per unit area in the n-side, given the overall space charge neutrality of the semiconductor, meaning that [72]:

$$N_A x_p = N_D x_n \tag{4.12}$$

where N_A and N_D are the doping level of p- and n+ regions in cm^{-3} and x_p and x_n are length of the depletion region in p- and n+ regions. It should be noted that given the big difference of doping levels between these two regions ($N_A \ll N_D$), almost all of the depletion region is formed in the intrinsic region ($x_p \gg x_n$). Depletion region length is given by:

$$L_{zd} = x_p + x_n \tag{4.13}$$

Total potential variation over the depletion region, called the built-in potential ($V_{built-in}$), is given by:

$$V_{built-in} = \frac{1}{2} E_m L_{zd} \tag{4.14}$$

where E_m is the maximum field that exists at the i and n regions interface and is given by:

$$E_m = \frac{q N_D x_n}{\epsilon_{si}} = \frac{q N_A x_p}{\epsilon_{si}} \tag{4.15}$$

where e_{si} is the permittivity of silicon ($\simeq 1.03 \times 10^{-12} \frac{F}{m}$). Using Eqs. 4.12 to 4.15 and assuming an applied bias voltage of V_d, depletion region length (L_{zd}), can be derived as a function of applied bias voltage and doping of p, i, n regions, given by the following relation:

$$L_{zd} = \sqrt{\frac{2 e_{si}}{q} \frac{(V_{built-in} - V_d) \cdot (N_A + N_D)}{N_A \cdot N_D}} \tag{4.16}$$

The built-in potential can also be derived by:

$$V_{built-in} = U_t \cdot log(\frac{N_a \cdot N_d}{n_i^2}) \tag{4.17}$$

where U_t is the thermal voltage ($\simeq 25mV$ at room temperature) and n_i is the intrinsic carrier concentration. U_t is given by:

$$U_t = \frac{kT}{q} \tag{4.18}$$

where k is the Boltzmann constant $(\simeq 8.617 \times 10^{-5} eV \cdot K^{-1})$, and T is the temperature in Kelvin.

Un-depleted region

When working with semiconductors, we might observe effects such as drift, diffusion, and generation and recombination of carriers. Continuity equations describe the device while considering all of these effects. The basic continuity equation for electrons is:

$$\frac{\partial n}{\partial t} = \frac{1}{q}\frac{\partial J_n}{\partial x} + (G_n - R_n) \tag{4.19}$$

where J_n is current density. Given the presence of both drift and diffusion effects:

$$J_n = J_{n-drift} + J_{n-diff} \tag{4.20}$$

where $J_{n-drift}$ and J_{n-diff} are drift and diffusion current density.
Drift current occurs as a result of the force that carriers experience when an electric field is applied. Drift current density of electrons is given by:

$$J_{n-drift} = qn\mu_n E \tag{4.21}$$

where μ_n is electron mobility ($\simeq 1400\frac{cm^2}{Vs}$ for silicon) and E is the applied electric field.
Diffusion current is a result of variation of carrier concentration within the semiconductor. Electron travel in the absorption layer is governed by diffusion according to Fick's first law [65]:

$$\Gamma_n = -D_n\frac{dn}{dx} \tag{4.22}$$

where Γ_n is the net electron flux, D_n is the electron diffusion coefficient, x is the lateral position of the electron (Fig. 4.2), and $\frac{dn}{dx}$ is the photo-generated

electron concentration gradient. The diffusion coefficient is related to the mobility of the electron in the intrinsic layer by the Einstein relationship, which is generalized for carriers away from the band edges [65]:

$$D_n = U_t \cdot \mu_n \tag{4.23}$$

Therefore diffusion current density is:

$$J_{n-diff} = -q \cdot \Gamma_n = qD_n \frac{dn}{dx} \tag{4.24}$$

where the negative sign corresponds to electrons carrying a $-q$ charge. Using Eqs. 4.25, 4.21 and 4.24, current density (J_n) in Eq. 4.19 can be replaced using the following relation:

$$J_n = q\mu_n nE + qD_n \frac{dn}{dx} \tag{4.25}$$

R_n in Eq. 4.19 is the net recombination rate of electrons in a p-type semiconductor, along the x direction. Once photons are absorbed in the intrinsic region, electrons are excited and the thermal equilibrium is disturbed. Thermal equilibrium can be re-established through recombination of electron and holes. The net recombination rate is given by:

$$R_n = \frac{n_p - n_{po}}{\tau_n} \tag{4.26}$$

where n_p is electron density in a p-type semiconductor after injection of excess carriers, n_{po} is electron density in a p-type semiconductor at thermal equilibrium, and τ_n is lifetime of excess minority carriers, the electrons (in this case $\simeq 1\mu s$). By substituting Eqs. 4.25 and 4.26 into 4.19, continuity equation for minority carriers in a p-type semiconductor (n_p), under low-injection condition is:

$$\frac{\partial n_p}{\partial t} = n_p \mu_n \frac{\partial E}{\partial x} + \mu_n E \frac{\partial n_p}{\partial x} + D_n \frac{\partial^2 n_p}{\partial x^2} + G_n - \frac{n_p - n_{po}}{\tau_n} \tag{4.27}$$

Now we apply the continuity equation to the un-depleted region of the pin structure that we are studying. The mentioned equation will be reduced to:

$$\frac{\partial n_p}{\partial t} = D_n \frac{\partial^2 n_p}{\partial x^2} + G_n - \frac{n_p - n_{po}}{\tau_n} = 0 \tag{4.28}$$

It should be noted that D_n and τ_n are related through diffusion length of electrons in intrinsic region (L_{Dni}), which can be derived by:

$$L_{Dni} = \sqrt{D_n \cdot \tau_n} \tag{4.29}$$

To solve this equation, we need to apply the boundary conditions at $x = 0$ and $x = L$. The boundary condition at $x = 0$, the $p+/p-$ interface, is:

$$n_p(x = 0) = n_{po} + G_n = \frac{n_i^2}{N_a} + G_n \tag{4.30}$$

In order to derive the boundary condition at $x = L$, let us consider the depletion region. As mentioned earlier there is a built-in voltage across this region given by Eq. 4.17. At thermal equilibrium the majority carrier density and doping concentration are almost equal ($N_A = n_{po}$, $N_D = n_{no}$) meaning that Eq. 4.17 can be written as:

$$V_{bi} = U_t \cdot log(\frac{p_{po} \cdot n_{no}}{n_i^2}) = U_t \cdot log(\frac{n_{no}}{n_{po}}) \tag{4.31}$$

where we used the fact that $p_{po}n_{po} = n_i^2$. Therefore we have:

$$n_{no} = n_{po}e^{V_{bi}/U_t} \tag{4.32}$$

which relates the electron density across the depletion region, through the built-in potential. By applying a bias voltage of V (forward or reverse), Eq. 4.32 turns into:

$$n_n = n_p e^{(V_{bi}-V)/U_t} \tag{4.33}$$

Given the assumption that the device is operating under low-injection condition, we have $n_n \simeq n_{no}$. By substituting this condition and Eq. 4.32 into Eq. 4.33, the second boundary condition is given and we have:

$$n_p(x = L) = n_{po}e^{V_d/U_t} \tag{4.34}$$

Enabling us to solve Eq. 4.28:

$$n_p(x) = n_{po} + G_n \cdot \tau_n + (n_{po}(e^{V_d/U_t} - 1) - G_n \cdot \tau_n)\frac{sinh(x/L_{Dni})}{sinh(L/L_{Dni})} \tag{4.35}$$

Thereafter, and by using Eq. 4.25, current density in the un-depleted region is given by:

$$J_n(x) = q\frac{D_n}{L_{Dni}} \cdot \frac{n_{po}((e^{V_d/U_t} - 1) - G_n \cdot \tau_n)}{sinh(L/L_{Dni})} \cdot cosh(\frac{x}{L_{Dni}}) \tag{4.36}$$

Current density is composed of a term which is present without illumination (dark term) and also the photo-generated term, caused by illumination. Using Eq. 4.36, photo-generated current density for point x along the lateral direction is given by:

$$J_{ph}(x) = -q \cdot \frac{D_n \cdot G_n \cdot \tau_n \cdot cosh(\frac{x}{L_{Dni}})}{L_{Dni} \cdot sinh(\frac{L}{L_{Dni}})} \tag{4.37}$$

L, length of the un-depleted region is equal to $L_i - L_{zd}$ as demonstrated in Fig. 4.2.
Using Eq. 4.11 and 4.37, Eq. 4.10 turns into:

$$IQE = \frac{L_{Dni} \cdot coth(\frac{L}{L_{Dni}}) + L_{zd}}{L_i} \tag{4.38}$$

directly relating IQE to design parameters.
Eq. 4.38 indicates that Internal Quantum Efficiency is independent of wavelength and input power and is strongly dependent on L_{zd} and L_i. In addition to its strong influence on IQE, total length of the intrinsic region (L_i) can also be set independently, making it one of the main design parameters.

Using this relation, dependency of IQE on intrinsic region length has been investigated which is presented in Fig. 4.3. L_{zd} is approximately $2\mu m$, given applied bias voltage of $-3V$, doping of $\simeq 10^{20} cm^{-3}$ for p and n region and doping of $\simeq 10^{15} cm^{-3}$ for i region. IQE drops as L_i exceeds the length of depletion region (L_{zd}), impacting External Quantum Efficiency (EQE) in a negative way. The results suggest that in order to attain a high IQE, L_i needs to approximate L_{zd}, however, we need to study how L_i impacts other performance parameters as well, before determining the optimum length.

4.3.2 Reflection and Transmission Losses

When light is moving from one medium to another, it can reflect back, transmit through, or get absorbed in the new medium. It is the absorbed light that will result in photo-generated current in a photo-receiver, and therefore

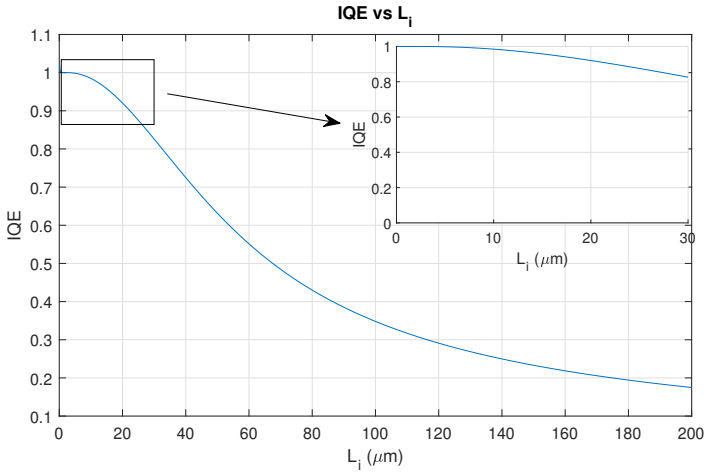

Figure 4.3: Internal Quantum Efficiency for $0 < L_i < 200\mu m$.

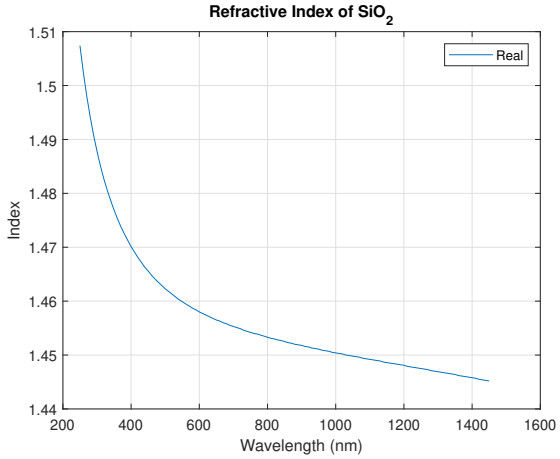

Figure 4.4: Refractive index profile of SiO_2.
[57] [74]

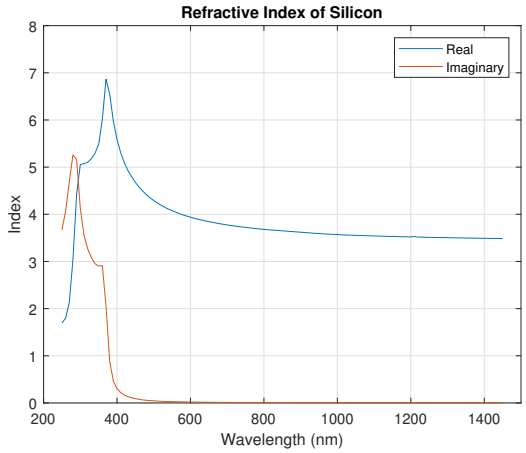

Figure 4.5: Refractive index profile of Si.
[14]

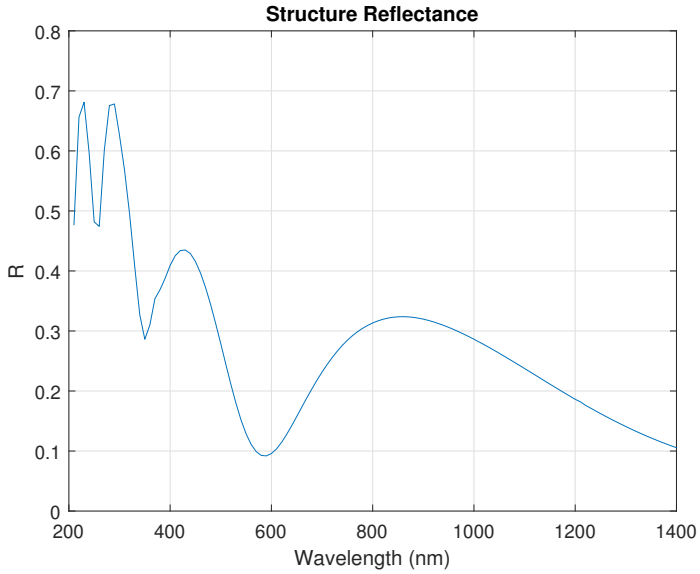

Figure 4.6: Reflectance of the structure given SiO_2 thickness of 300nm.

its importance should be emphasized when designing the device. This can be implemented using η given by:

$$\eta = \frac{P_{abs}}{P_{in}} \tag{4.39}$$

Where P_{in} is the optical power density (by unit of area) incident to the photosensitive area, while P_{abs} is the part that is absorbed by the device along the thickness of the i region [11]. This value can be derived by:

$$\eta = (1 - R) \cdot (1 - T) \tag{4.40}$$

Where R represents the portion of incident light reflecting back from the device and T corresponds to transmittance of light in the absorbing layer. As implied in Eq. 7, the portion of light, absorbed in the intrinsic region can be derived through calculating and excluding the reflectance and transmittance terms.

Calculating Reflectance [17]

We begin by introducing a general model, a multi-layer thin film structure consisting of N materials, numbered $0, 1, ..., N-1$ (light starts from layer 0), where the first and last layers (0 and $N-1$) are semi-infinite and others are finite. We define:

$$\delta_i = d_i \cdot k_{zi}; \tag{4.41}$$

where δ_i represents the phase that comes from passing through layer i, d_i is the thickness of layer i, and k_{zi} is given by:

$$k_{zi} = \frac{2 \cdot \pi \cdot n_i(\lambda)}{\lambda} \tag{4.42}$$

where λ is the wavelength and $n_i(\lambda)$ is the refractive index of the layer i material in the given wavelength. It should be noted that normal incident is assumed (light is shining perpendicularly on the surface), which also means that there is no difference between s and p polarization.

For layer i, M_i is given by:

$$M_i = \begin{bmatrix} e^{-j\delta_i} & 0 \\ 0 & e^{-j\delta_i} \end{bmatrix} \cdot \begin{bmatrix} 1 & r_{i,i+1} \\ r_{i,i+1} & 1 \end{bmatrix} \cdot \frac{1}{t_{i,i+1}} \tag{4.43}$$

where $r_{i,i+1}$ and $t_{i,i+1}$ are reflection and transmission coefficients for the interface between layer i and $i+1$.
M_{total} is derived using:

$$M_{total} = \frac{1}{t_{0,1}} \cdot \begin{bmatrix} 1 & r_{0,1} \\ r_{0,1} & 1 \end{bmatrix} \cdot M_1 \cdot M_2 \cdot ... \cdot M_{N-2} \tag{4.44}$$

The total reflectance coefficient is given by:

$$r = \frac{M_{total\,21}}{M_{total\,11}} \tag{4.45}$$

Meaning that reflectance of the structure is determined by:

$$R = rr^* \tag{4.46}$$

In the pin structure that is being evaluated, as illustrated in Fig. 4.2 there is an SiO_2 layer between air and the absorbing layer. Thus, $N = 3$ and layers 0,1, and 2 are air, SiO_2, and Si. δ_1 will be calculated at each wavelength for

a $d_1 = 300nm$. Refractive index profile of SiO_2 (Fig. 4.4) will be used in Eq. 4.42. Therefore, M_1 can be calculated using Eq. 4.43, and Eq. 4.44 will turn into:

$$M_{total} = \frac{1}{t_{0,1}} \cdot \begin{bmatrix} 1 & r_{0,1} \\ r_{0,1} & 1 \end{bmatrix} \cdot M_1 \tag{4.47}$$

where $r_{0,1}$, and $r_{1,2}$, are reflectance coefficient of air/SiO_2 and SiO_2/Si interface, and $t_{0,1}$, and $t_{1,2}$ are the transmission coefficient for these two interfaces. When light is moving from medium a to b, assuming that the second medium might absorb light, the reflectance coefficient at each wavelength is given by [50]:

$$r_{a,b} = \sqrt{\frac{(n_b - n_a)^2 + k_b^2}{(n_b + n_a)^2 + k_b^2}} \tag{4.48}$$

Where n_a and n_b are real part of refractive index for mediums a and b, and k_b is the imaginary part of refractive index for medium b.
Therefore, using Eq. 4.48 and refractive index profiles of SiO_2 and Si (Fig. 4.4 and 4.5), $r_{0,1}$ and $r_{1,2}$ will be derived. Calculating $t_{0,1}$ and $t_{1,2}$ can be skipped, given that in Eq. 4.45, both $M_{total21}$ and $M_{total11}$ are multiplied by $\frac{1}{t_{0,1}}$ and $\frac{1}{t_{1,2}}$.
Reflectance of the structure (R), is presented in Fig. 4.6. It should be noted that given the low level of doping for Si ($\simeq 10^{15} cm^{-3}$), its effect on refractive index profile is negligible. Reflection losses are significantly reduced using anti-reflection coatings, made of several thin layers with different refractive indices [65].

Therefore, the specific fluctuations in reflectance of the structure demonstrated in Fig. 4.6 is influenced by the properties of materials and their thickness. The peaks in reflectance profile of each material is a consequence of its specific band structure.

Calculating Transmittance

Transmittance is dependent on the absorption coefficient of the i region and on its thickness (Fig. 4.7 presents the absorption profile of Si). In order to calculate how much of the light is not absorbed and keeps transmitting through, we use:

$$T(\lambda) = e^{-\alpha(\lambda) \cdot t_{si}} \tag{4.49}$$

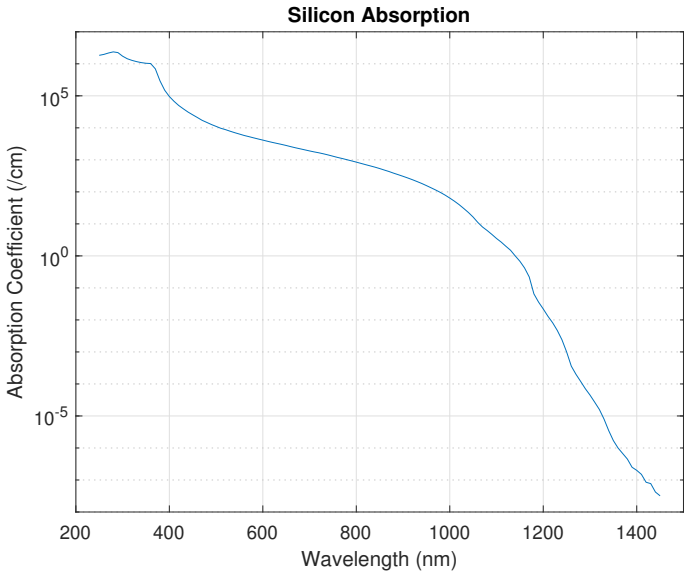

Figure 4.7: Absorption coefficient profile of silicon. [36] [35]

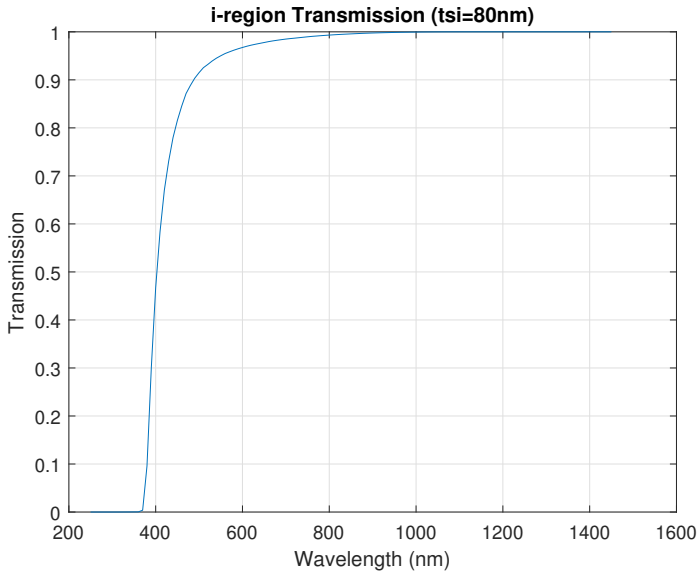

Figure 4.8: Transmittance in the intrinsic region.

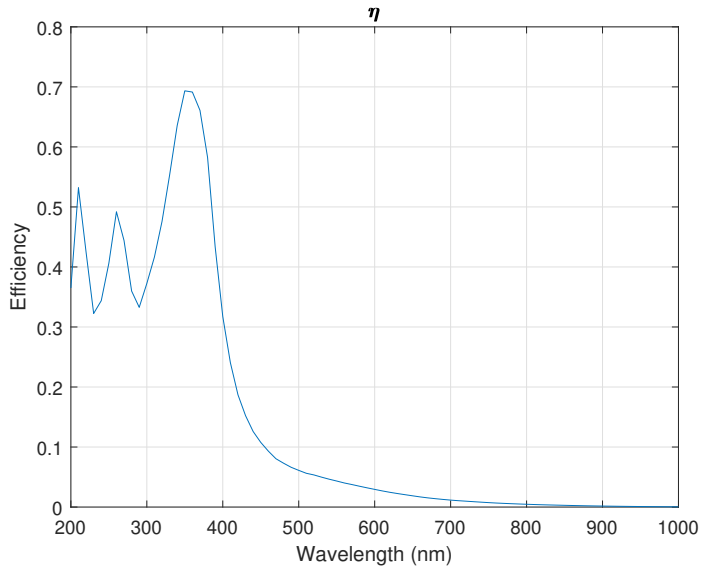

Figure 4.9: $\eta = (1 - R) \cdot (1 - T)$.

Where t_{si} is the thickness of the absorption layer, $\alpha(\lambda)$ is the absorption coefficient of the intrinsic region at wavelength λ, and $T(\lambda)$ is the transmittance at the same wavelength. Transmittance in i region is demonstrated in Fig. 4.8. T rapidly approaches unity once wavelength exceeds $400nm$, strongly limiting the performance of the device.
Combining derived results for R and T and using Eq. 7 we obtain η (Fig. 4.9).

4.3.3 Photosensitive Area

As mentioned before, incident light needs to be absorbed in the i region in order to contribute to generation of electrons. When describing the exposure of the device to the input light, the area covering the intrinsic region is referred to as the photosensitive area. This is because any photon incident on other areas (area covering the p or n region) will not be absorbed. We

apply this consideration by defining α_{ph} as:

$$\alpha_{ph} = \frac{A_{ph}}{A_{total}} \tag{4.50}$$

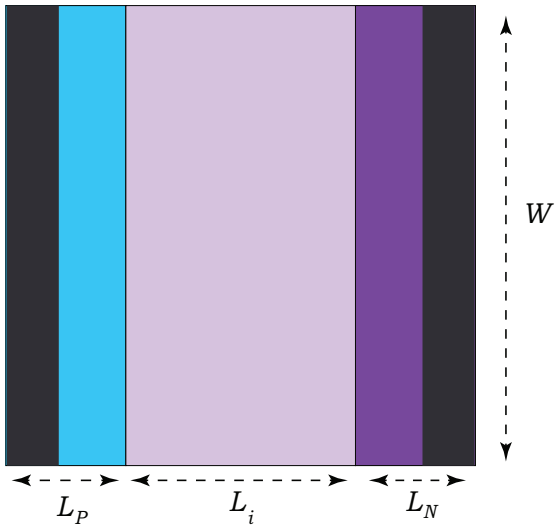

Figure 4.10: *pin* photodiode, top view.

and using it in our calculations. Here, A_{ph} is the photosensitive area and A_{total} is the total area of the device. Considering the dimensions of the device, presented in Fig. 4.10, A_{ph} and A_{total} can be derived using:

$$A_{ph} = W \cdot m \cdot L_i \tag{4.51}$$

$$A_{total} = W \cdot (m \cdot L_i + (m+1) \cdot L_{PN}) \tag{4.52}$$

Where we make the assumption:

$$L_P = L_N = L_{PN} \tag{4.53}$$

W is width of the device and m is the number of fingers which is given by:

$$m = \frac{L_t - L_{PN}}{L_t + L_{PN}} \tag{4.54}$$

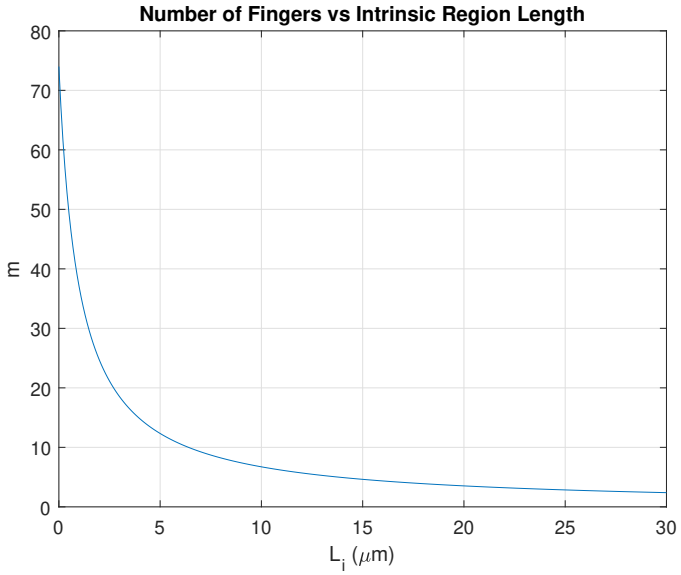

Figure 4.11: Number of fingers vs intrinsic region length; L_t = 75μm, L_{PN} = 1μm.

L_t being the total length of the chip. We expect m to decrease with the increase of L_i. Dependency of number of fingers as a function of L_i has been demonstrated in Fig. 4.11.

Implementing α_{ph} in our calculation of efficiency, External Quantum Efficiency EQE will be:

$$EQE = \alpha_{ph} \cdot \eta \cdot IQE \tag{4.55}$$

Utilizing different CMOS technologies will change the efficiency of the device. By increasing the complexity of the fabrication process and its resolution, we can decrease L_{PN} which will also influence the effective area (Fig. 4.12 and 4.13).

As shown in Fig. 4.14 and 4.15, the optimum L_i has a lower value for a device with smaller L_{PN}; This will be beneficial for the trade off between speed and responsivity.

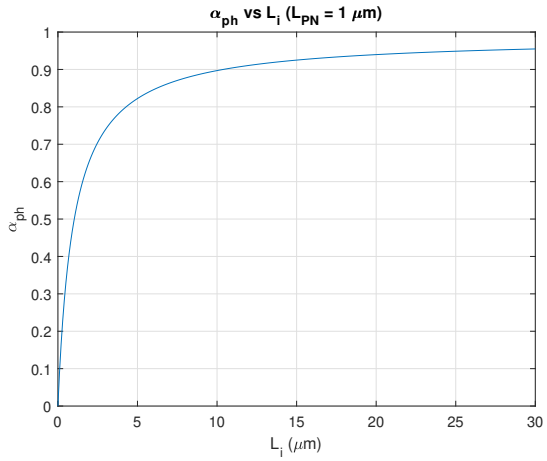

Figure 4.12: α_{ph} vs L_i; $L_{PN} = 1\mu m, V_d = -3V, W = 75\mu m, L_t = 75\mu m, t_{si} = 80nm$.

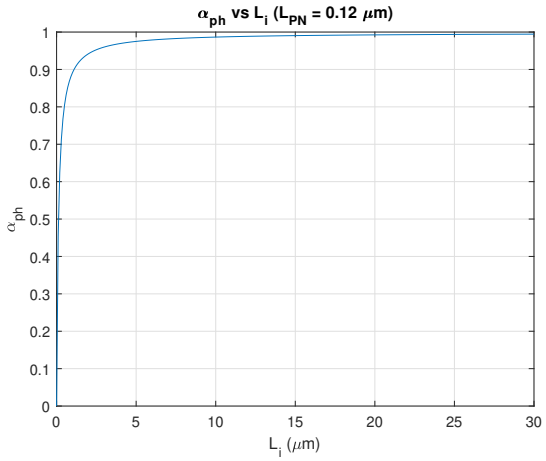

Figure 4.13: α_{ph} vs L_i; $L_{PN} = 0.12\mu m, V_d = -3V, W = 75\mu m, L_t = 75\mu m, t_{si} = 80nm$.

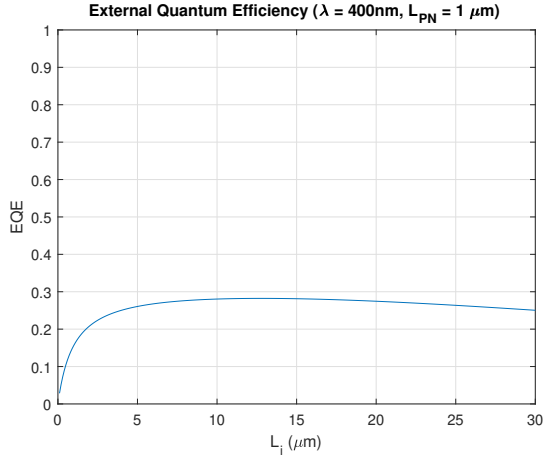

Figure 4.14: External Quantum Efficiency vs L_i; $L_{PN} = 1\mu m$.

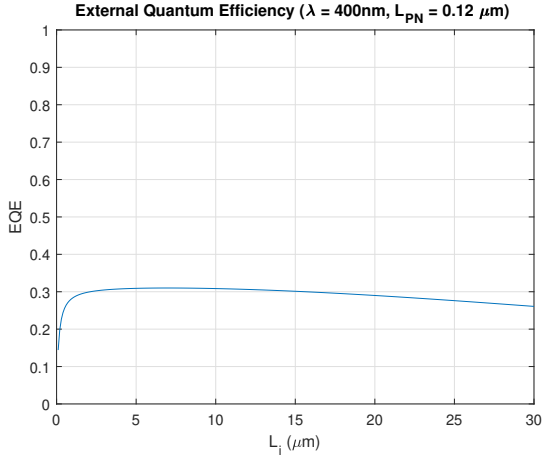

Figure 4.15: External Quantum Efficiency vs L_i; $L_{PN} = 0.12\mu m$.

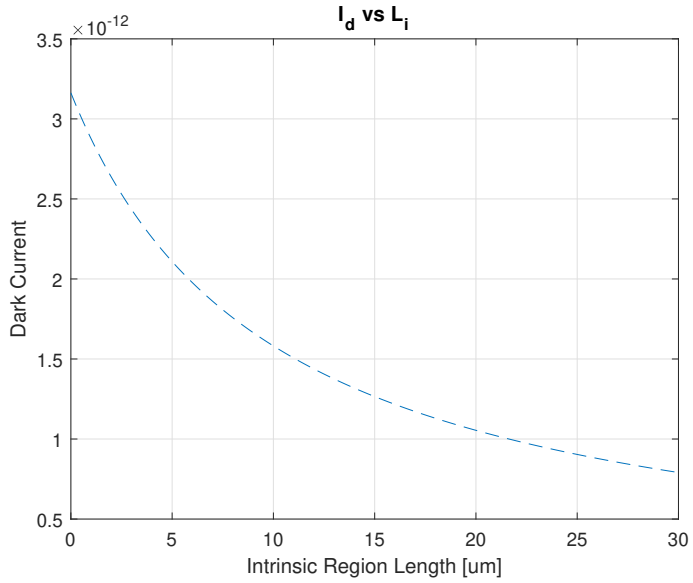

Figure 4.16: Dark current vs L_i.

4.4 Dark Current

We introduced dark current in section 3.3 and mentioned that minimizing it improves sensitivity. As demonstrated earlier, light penetration depth gets smaller as wavelength decreases. In the lateral pin diode, the depletion region is formed starting from the top and continues to the depth of the junction, and the remaining silicon substrate is not used for photodetection and only contributes to increase the dark current due to thermal generation. This highlights the benefit of implementing the photodetector in SOI wafers and emphasizes the importance of buried oxide layer (BOX) [64]. The dark current in the device is dominated by surface generation current.

$$I_{rg} = \frac{q \cdot ni}{2\tau_{eff}} \cdot m \cdot W \cdot t_{si} \cdot L_{zd} \cdot (e^{\frac{V_d}{2U_t}} - 1) \tag{4.56}$$

The dark current is proportional to the area and thickness of the absorbing layer. Increasing the length of the intrinsic region will decrease the number of fingers and consequently the generated dark current. When determining the optimum length the corresponding dark current, quantum efficiency and speed should be considered (Fig. 4.16).

4.5 Considerations

When implementing the physical modeling, it should be noted that minority carriers concentration and density has to be modeled, due to existence of un-depleted region and the carrier concentration and generation terms are not constant along Y axis.

Recombination phenomena consists of volume and surface recombinations, however, due to t_{si} being small compared to L_{Dni}, the majority of volume recombination can be modeled by current density along X axis.

Current density and carrier concentration is composed of dark term (present without illumination), and photo-generated term (due to illumination). As mentioned earlier any photo-generated current in p and n layer is negligible; Thus, total photo-generated current density is sum of photo-generated current in the depletion region, and also electron current density evaluated at the end of un-depleted region.

4.6 Conclusion

Conclusion about the effects of each design parameter on performance can be summarized as:

L_i **and** L_{zd}**:** Length of the intrinsic and depleted region determines the Internal Quantum Efficiency (Q_I), and thus performance of the device.

N_a**,** N_d**, and** n_i**:** Doping of three regions, determine the built-in voltage ($V_{built-in}$) and depletion length (L_{zd}). Intrinsic region doping also influences sensitivity.

L_{PN}**,** m**, and** L_i**:** Length of p, i, and n regions, and number of fingers directly influence the Effective Area (A) and Total Quantum Efficiency (QE_t).

W**,** L_i**, and** t_{si}**:** Dark current is strongly dependent on width of the diode, length of intrinsic region, and its thickness.

V_d **trade off:** Applied bias voltage enhances transit of carriers and lowers capacitance, however, exceedingly high voltages will result in breakdown.

L_{zd} **trade off:** A higher depleted region length will result in higher absorption of light, however, it increases the transit time and decreases the speed of device.

Chapter 5

SiGe SACM Waveguide Avalanche Photodiode

In this chapter we present a p-i-p-i-n design for a silicon germanium waveguide APD. Steady state and transient simulations are performed and important parameters such as current, responsivity, bandwidth, and excess noise factor are obtained. Simulation samples provided by Lumerical, served as helpful and insightful guidelines for performing the simulation and creating the structure [1] [8]. The first sample demonstrated steady state simulation of a p-p-i-n device reported by Huang et al. [44], while the other was a transient simulation of a vertical photodiode [54]. We begin this chapter by introducing the proposed structure.

5.1 Structure

The photodiode has an SACM layout. Light is led to the device using a waveguide structure and is then absorbed in the germanium layer. The photodiode is based on $250nm$ SOI, which is highly n doped. This part is followed by $100nm$ of intrinsic and $50nm$ of p doped silicon. The germanium layer grown on the silicon will have a thickness of $400nm$, consisting of 350 nm of intrinsic region and 50 nm of p doped layer. The structure is shown in Fig. 5.1 and 5.2 with dimensions specified.

Doping levels and the thickness for each layer is demonstrated in Table 5.1. The layer numbers in this table corresponds to Fig. 5.1. Also refractive index of each material is listed in Table 5.2 and then graphically presented

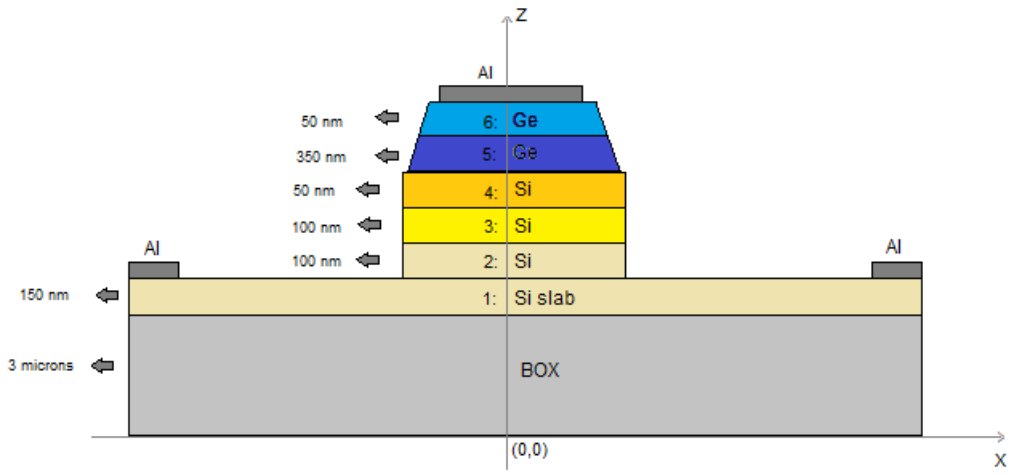

Figure 5.1: Layers thickness and doping profile.

in Fig. 5.3. These indices represent the unperturbed state where no carriers are introduced. The influence of doping levels on refractive index can be implemented using Drude model [40] [71] [70]:

$$\Delta n = -\frac{q^2\lambda^2}{8\pi^2 c^2 \epsilon_0 n}[\Delta N_e/m^*_{ce} + \Delta N_h/m^*_{ch}] \tag{5.1}$$

$$\Delta k = \frac{q^3\lambda^3}{16\pi^3 c^3 \epsilon_0 n}[\Delta N_e/m^{*2}_{ce}\mu_e + \Delta N_h/m^{*2}_{ch}\mu_h] \tag{5.2}$$

where q is the electronic charge, ΔN_e and ΔN_h are the free carrier densities for electrons and holes, ϵ_0 is the permittivity of free space, n is the unperturbed refractive index, m^*_{ce} and m^*_{ch} are the conductivity effective mass of electrons and holes, and μ_e and μ_h are the electron and hole mobility.

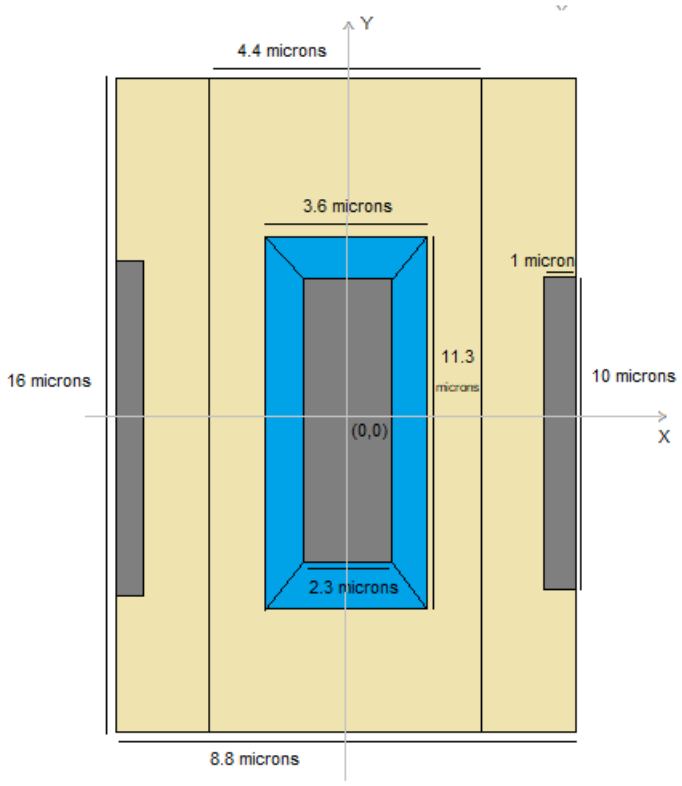

Figure 5.2: Design details, top view.

Layer Number	Dopant Type	Doping Level (cm-3)	Layer Thickness (nm)
1	n	10^{20}	150
2	n	10^{20}	100
3	i	10^{15} (p type)	100
4	p	2×10^{17}	50
5	i	10^{15} (p type)	350
6	p	10^{19} – 10^{17} Diffusive doping	50

Table 5.1: Dopant type, doping level and thickness of layers in the silicon germanium photodiode.

Material	(n,k)	Wavelength (nm)
Si	(3.48,0)	1550
SiO2	(1.44,0)	1550
Ge	≃(4.275,0.005)	1550

Table 5.2: Refractive index of materials used in the silicon germanium avalanche photodiode.

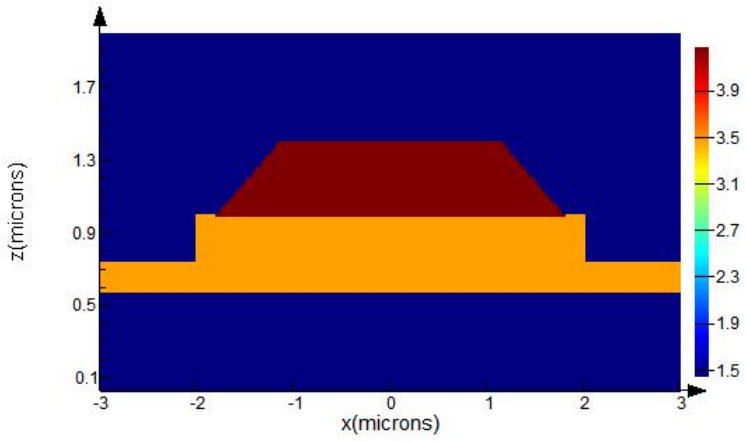

Figure 5.3: Refractive index basic representation.

5.2 Simulation

When modeling, the aim is to predict the performance of the device before it is fabricated, as accurately as possible. By successfully anticipating ideal design parameters, fabricating high quality devices becomes more feasible. Therefore, it is important to avoid simplifying assumptions as much as possible. Here we used FDTD and DEVICE modules of Lumerical to perform simulations on the structure and to obtain opto-electrical behaviors of the device. Field and temperature dependency of carriers mobility and non-uniformity of doping levels for each material are implemented in the simulation to ensure a higher accuracy for the simulation.

First, Finite Difference Time Domain method (FDTD) is applied to the structure. FDTD is a numerical modeling technique which solves Maxwell

equations in time domain. After applying light to the structure and performing the optical simulation, generation along the absorbing layer is obtained. Importing the generation term into the DEVICE module, enables us to perform the electrical simulation in order to acquire dark current, photocurrent, responsivity, gain, bandwidth, and excess noise factor.

5.2.1 Optical Simulation and Generation

First, the structure is created in FDTD simulation environment, where each component is included by defining its geometry and material property. Germanium and silicon ($400nm$ and $250nm$) are placed on $150nm$ silicon slab and enclosed by dielectric. Fig. 5.4 presents the structure defined in FDTD simulation environment.

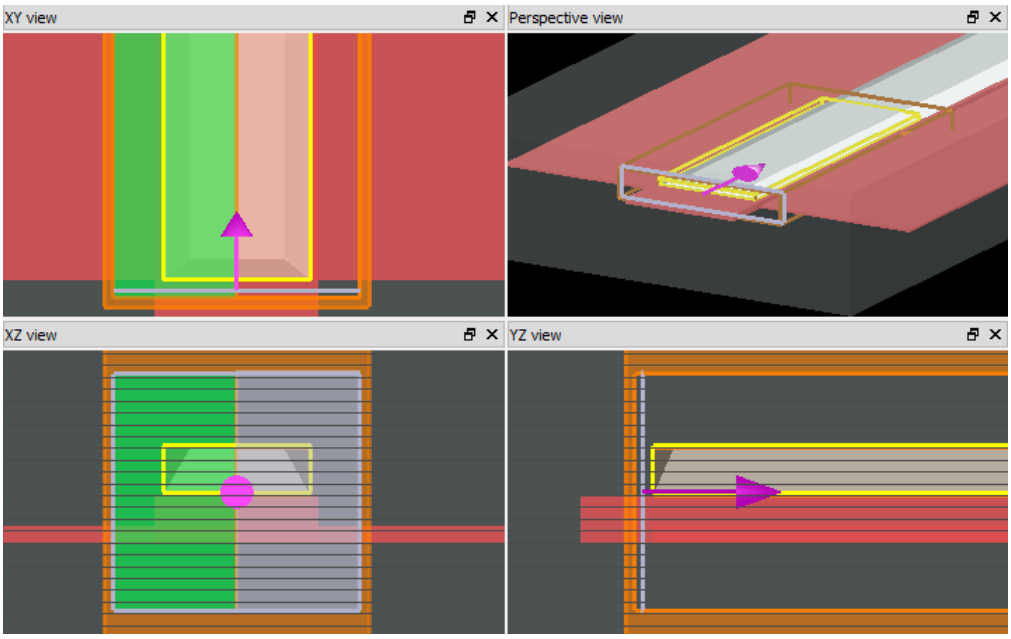

Figure 5.4: Structure implemented in FDTD environment.

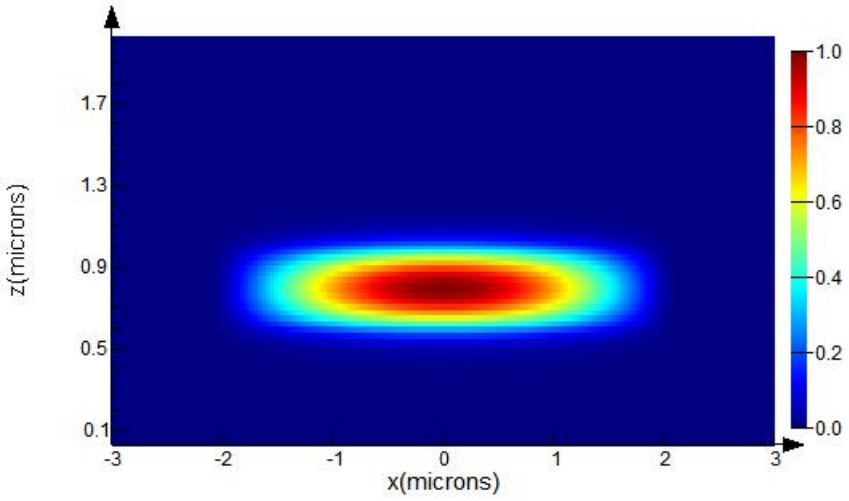

Figure 5.5: Light source with fundamental mode, XZ plane.

Initially, optical simulation is performed to obtain the generation rate. Light source with fundamental mode has been used to illuminate the structure (Fig. 5.5). After executing the simulation, electric field and generation rate of carriers are obtained along the absorbing layer and for different cross sections (Figures 5.6 - 5.9). After this, generation needs to be averaged along the y axis (Fig. 5.10 and 5.11) to be imported for electrical simulation. The results are shown for $z = 1.04\mu m$ and $z = 1.34\mu m$ (the germanium layer starts at $z = 1\mu m$ and ends at $z = 1.4\mu m$).

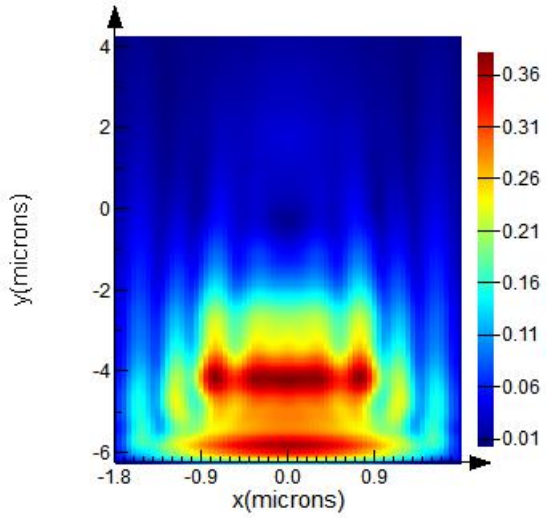

Figure 5.6: Electric field, top view $z = 1.04\mu m$.

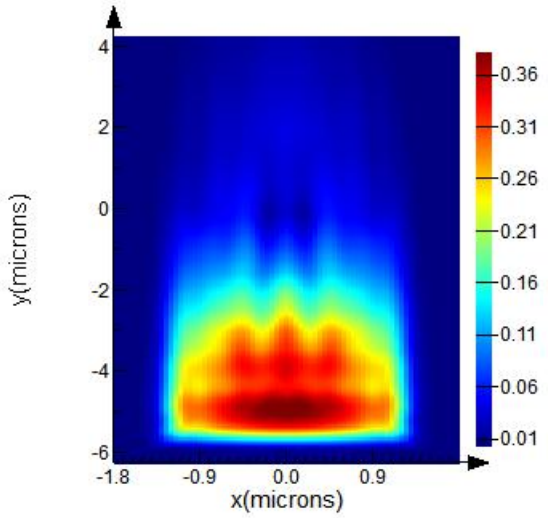

Figure 5.7: Electric field, top view $z = 1.34\mu m$.

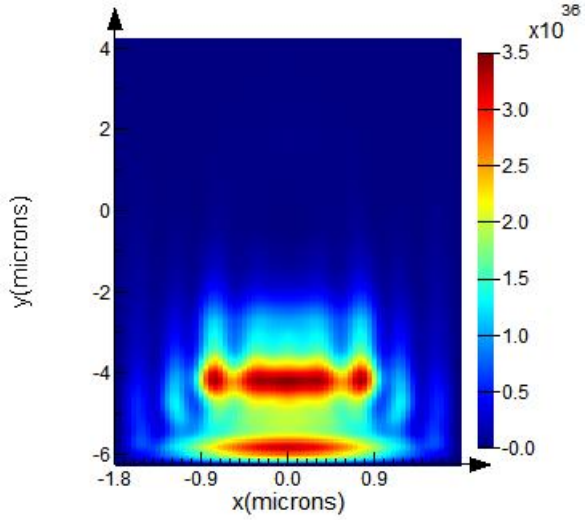

Figure 5.8: Generation in absorbing layer, top view $z = 1.04\mu m$.

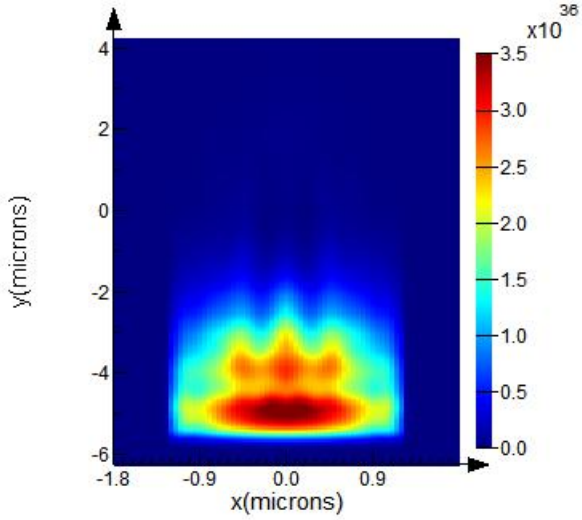

Figure 5.9: Generation in absorbing layer, top view $z = 1.34\mu m$.

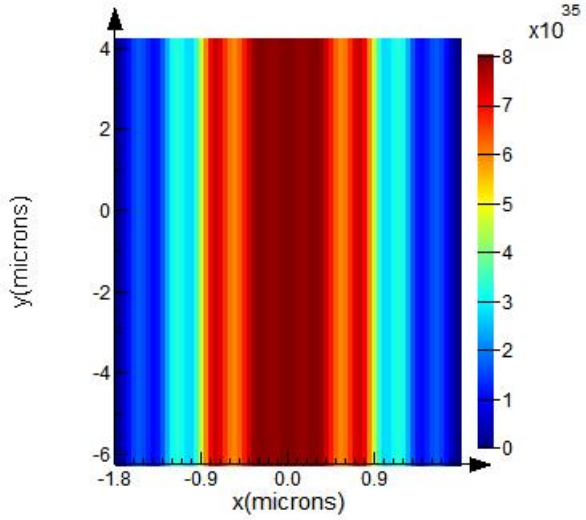

Figure 5.10: Generation in absorbing layer, averaged along y direction, top view z = $1.04\mu m$.

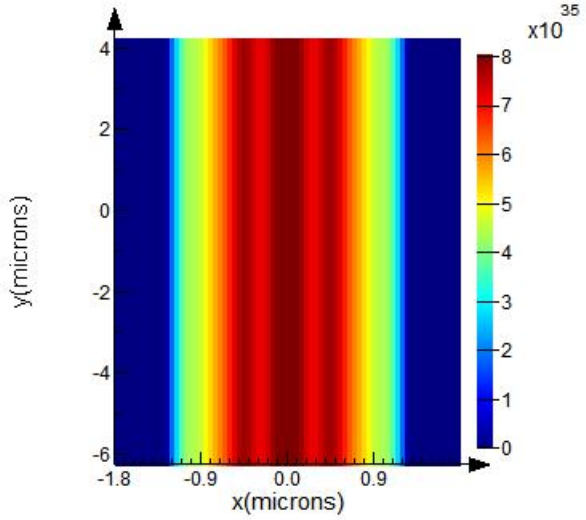

Figure 5.11: Generation in absorbing layer, averaged along y direction, top view z = $1.34\mu m$.

5.2.2 Electrical Simulation

The next step is to perform the electrical simulation in DEVICE environment. Fig 5.12 shows the structure implemented. Steady state and transient simulations are performed separately and for a temperature of $300K$.

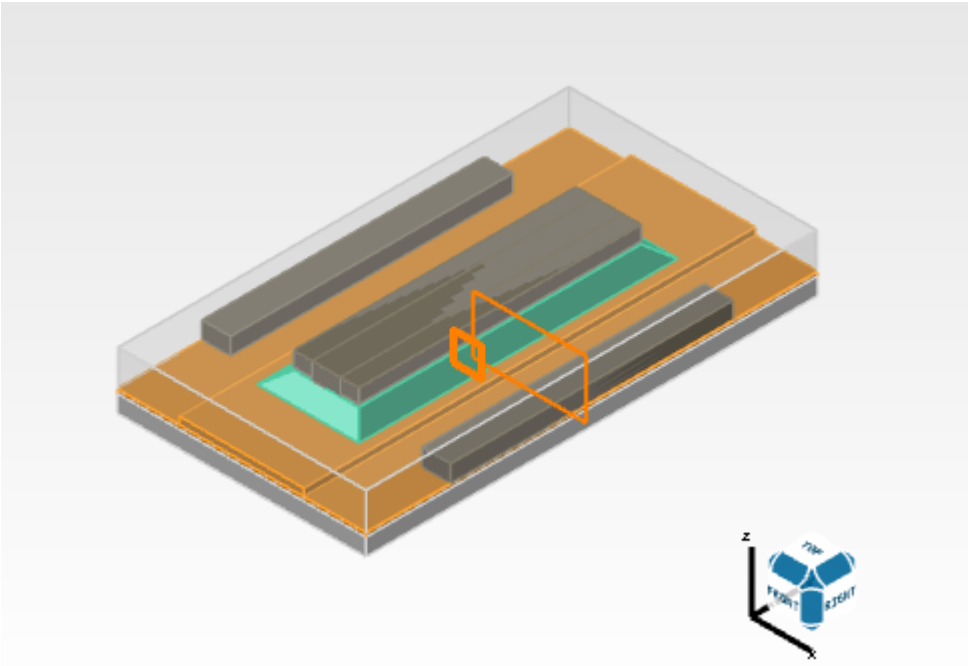

Figure 5.12: Implemented design in Lumerical DEVICE environment.

Utilizing the averaged generation rate enables us to perform a 2-dimensional simulation instead of a $3D$ simulation, using the uniform geometry of the structure along y axis.

To perform the electrical simulation, doping for each layer is applied separately while using appropriate doping distribution. It is important to consider a diffusive doping (as opposed to uniform doping) for a layer when necessary, to ensure accurate results. Diffusive doping with a Gaussian distribution has been employed for p doped germanium layer, whereas a constant doping has been applied to other layers.

Surface recombination has also been included for each interface, to enhance the accuracy of the results. Hurkx model has been used for representing recombination which represents both trap-assisted tunneling and band-to-band tunneling.

By implementing impact ionization and band-to-band tunneling the avalanche multiplication is modelled. Thereafter, current and its dark component are achieved by solving the Poisson and drift-diffusion equations.

5.3 Results

In this section we present the obtained performance parameters for the proposed p-i-p-i-n photodiode. It is vital to ensure that these results, are accurate approximations for the performance of the fabricated device. Later in this chapter, two examples of comparison between these simulations and actual measurements are presented in section 5.3.3 and 5.3.6. Moreover, to methodically investigate the reliability of our results, we begin by evaluating the impact of different mesh settings on accuracy.

5.3.1 Mesh and Accuracy

When performing the simulation, the mesh settings has an essential part in determining the accuracy of the simulation. Setting a finer mesh can enhance the accuracy, however, it will also increase the simulation time. Therefore, it is important to closely observe the impact of mesh settings on obtained results and pick an appropriate setting for the simulation. The simulation adopts an adaptive mesh strategy where it starts with coarse mesh and proceeds to use finer mesh in sensitive regions. The initial mesh size and the lower limit are respectively determined by maximum edge length and minimum edge length. Fig. 5.13 shows the mesh generated and how the size gets smaller for edges and more critical areas.

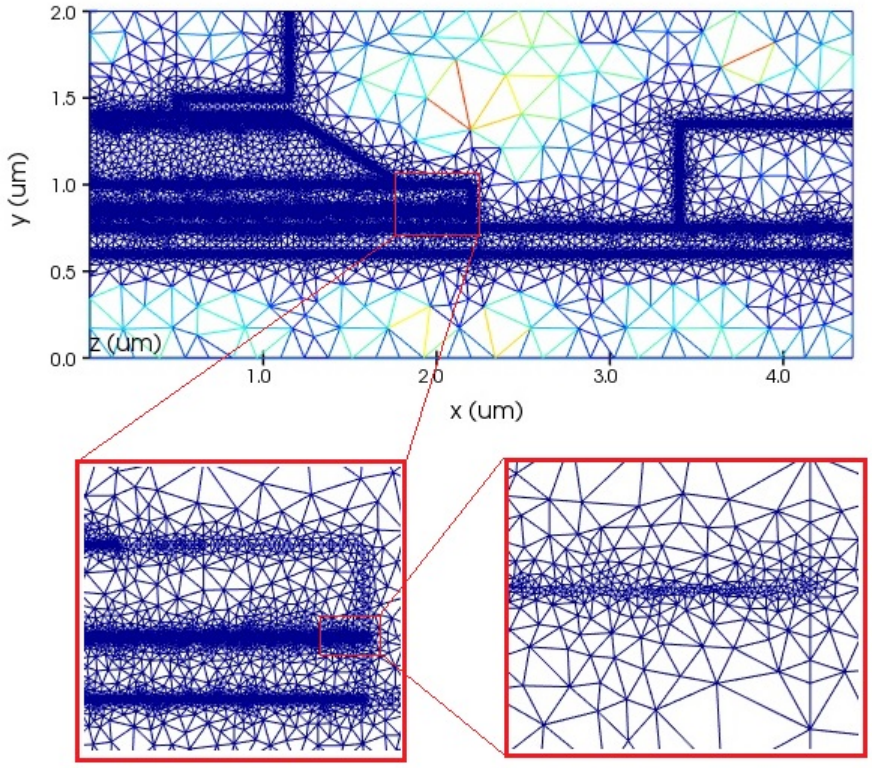

Figure 5.13: Generated mesh. maximum edge length = 200 nm, minimum edge length = 500 pm.

We used dark current as a baseline for our observation regarding the relation between mesh and the accuracy of our results. We provide more details about obtaining dark current in section 5.3.3. Fig. 5.14 shows the dark current of the device as a function of applied bias voltage. Then the same results are obtained for different mesh minimum edge length, ranging between 15 nm and 100 pm. Fig. 5.15 shows the derived dark current as a function of mesh accuracy, for two different voltages. The data points are provided in table 5.3.

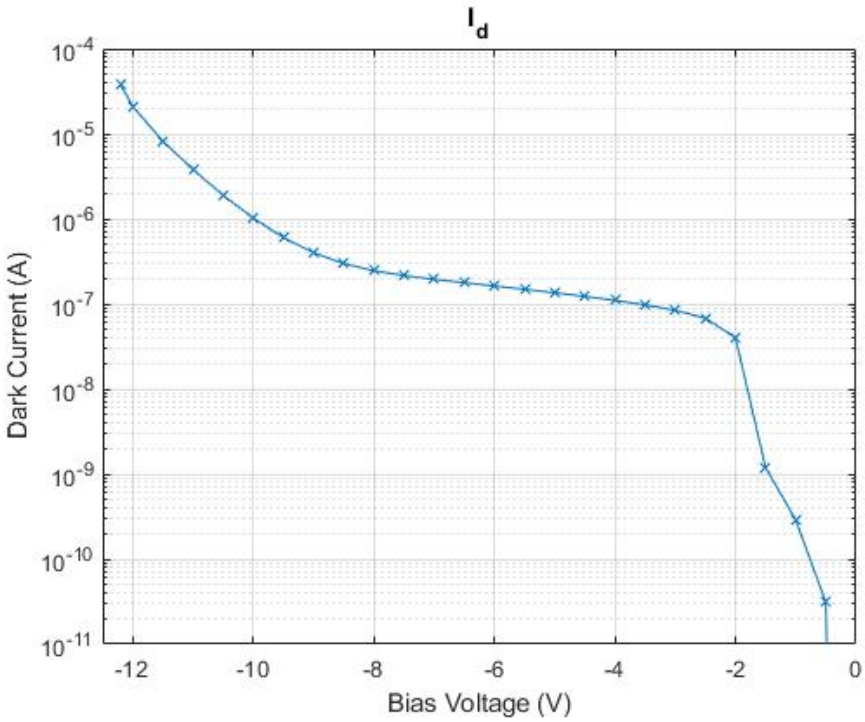

Figure 5.14: Dark current as a function of applied bias voltage.

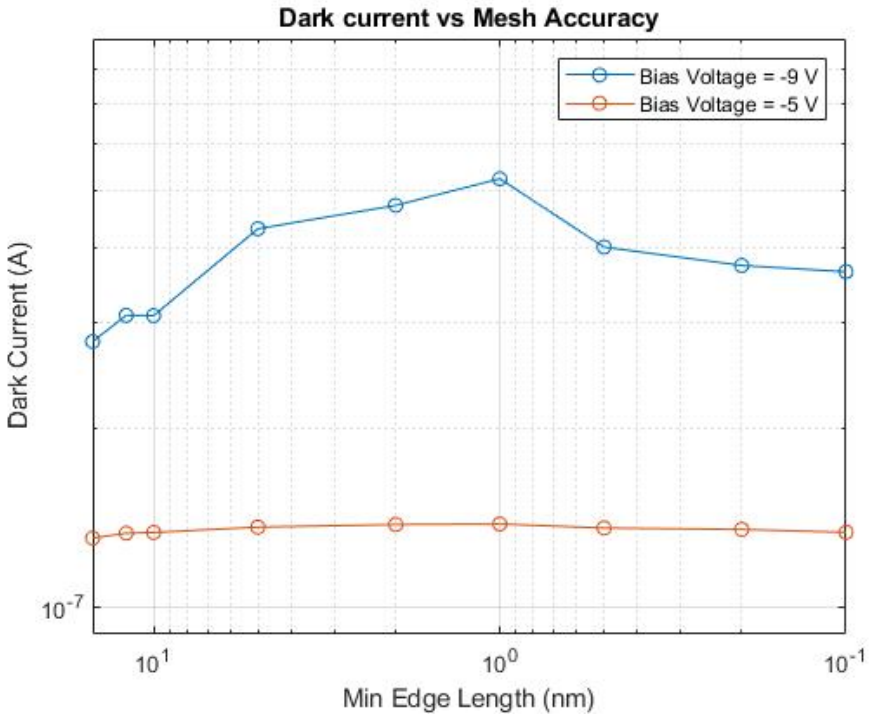

Figure 5.15: Obtained dark current as a function of mesh minimum edge length, for $V = -9$ and $V = -5$.

Mesh Minimum Edge Length	Dark Current at V= -5 V (A)	Dark Current at V= -9 V (A)
15 nm	1.30475e-07	2.79025e-07
12 nm	1.32973e-07	3.08822e-07
10 nm	1.33348e-07	3.08532e-07
5 nm	1.36159e-07	4.31706e-07
2 nm	1.37507e-07	4.72549e-07
1 nm	1.37800e-07	5.23773e-07
500 pm	1.35684e-07	4.02101e-07
200 pm	1.34946e-07	3.74502e-07
100 pm	1.33442e-07	3.65574e-07

Table 5.3: Data points for Fig. 5.15.

We then proceed to apply Richardson extrapolation to the existing data

points. This presents us with the value, which the result would eventually converge to. In this case the dark current converges to $133nA$ for $V = -5V$ and $362nA$ for $V = -9V$.

Using this value, we can derive the relative error for obtained dark current at each mesh setup. Fig. 5.16 shows the dark current relative error as a function of mesh minimum edge length.

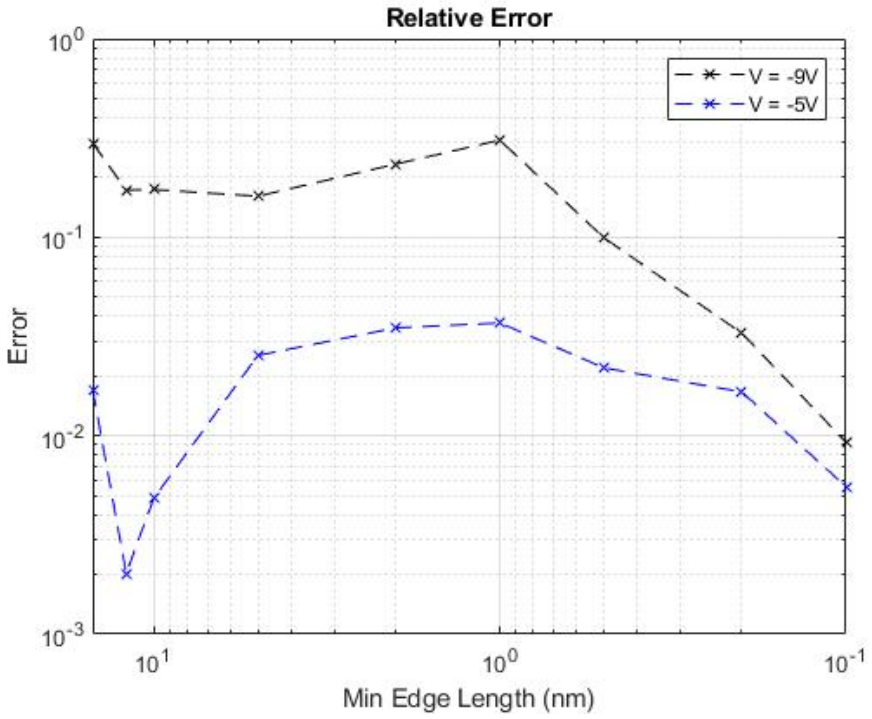

Figure 5.16: Relative error for obtained dark current as a function of mesh minimum edge length, for $V = -9$ and $V = -5$.

As expected, the results suggest a general decline in relative error as the minimum edge length decreases. After obtaining the relative error for each simulation, we can proceed to determine the appropriate mesh settings. The obtained results also provide an essential understanding to the reliability of the simulation. Given the current results we decided to use a minimum edge length of 500 pm for simulating this structure.

The estimated error will determine the number of meaningful digits in the obtained results. For example, given Fig. 5.16 and using table 5.3, we report

a dark current of $1.36 \times 10^{-7}A$ and $4.0 \times 10^{-7}A$ at $V = -5V$ and $V = -9V$.

5.3.2 Electric Field

We can monitor the electric field for different bias voltages to evaluate its effect on activating the structure. Fig. 5.17 shows the electric field at −5V and −9V. As expected, the electric field increases for higher bias voltages.

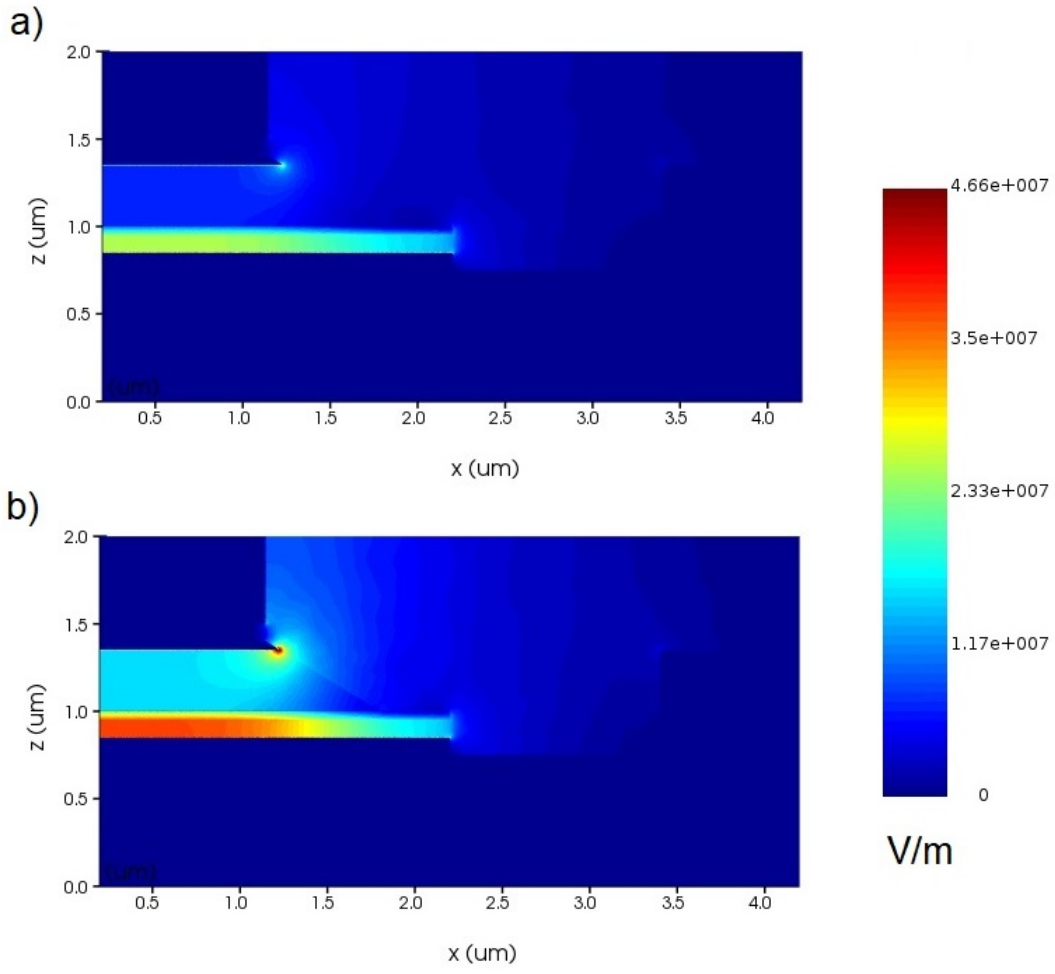

Figure 5.17: Electric field at a) $-5V$ and b) $-9V$, side view.

As demonstrated the electric field remains higher in the silicon avalanche layer, compared to other regions. Having a lower field in germanium will decrease band-to-band tunneling which contributes to dark current. It also decreases the high requirements for doping [44].

5.3.3 Current

The total current is composed of photocurrent and dark current terms (I_p and I_d) and is given by:

$$I = I_p + I_d = (I_p + I_{dm}) \cdot M + I_{du} \tag{5.3}$$

In order to derive dark current (I_d) a separate simulation needs to be performed without illumination. Measurements for currents (I and I_d) are taken from the electrodes, where output current for each applied reverse bias voltage is obtained. A similar procedure presented by Lumerical [1] which is implemented for Huang et al. structure [44], has shown results with close agreement to performed measurements (Fig. 5.18).

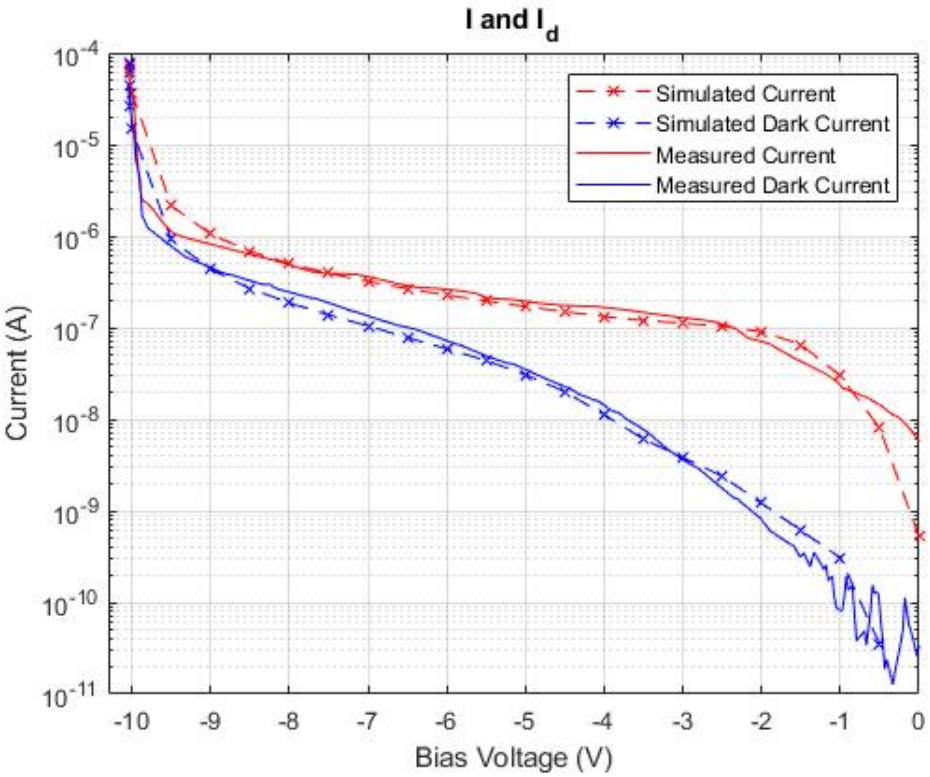

Figure 5.18: A comparison between simulation results and reported measurements for current (I) and its dark component (I_d). Simulation results are presented by Lumerical [1]; Fabricated device and measurements reported by Huang et al. [44].

Fig. 5.19 shows the obtained current as a function of applied bias voltage for the proposed p-i-p-i-n structure. The influence of input power on current is also investigated at the same time.

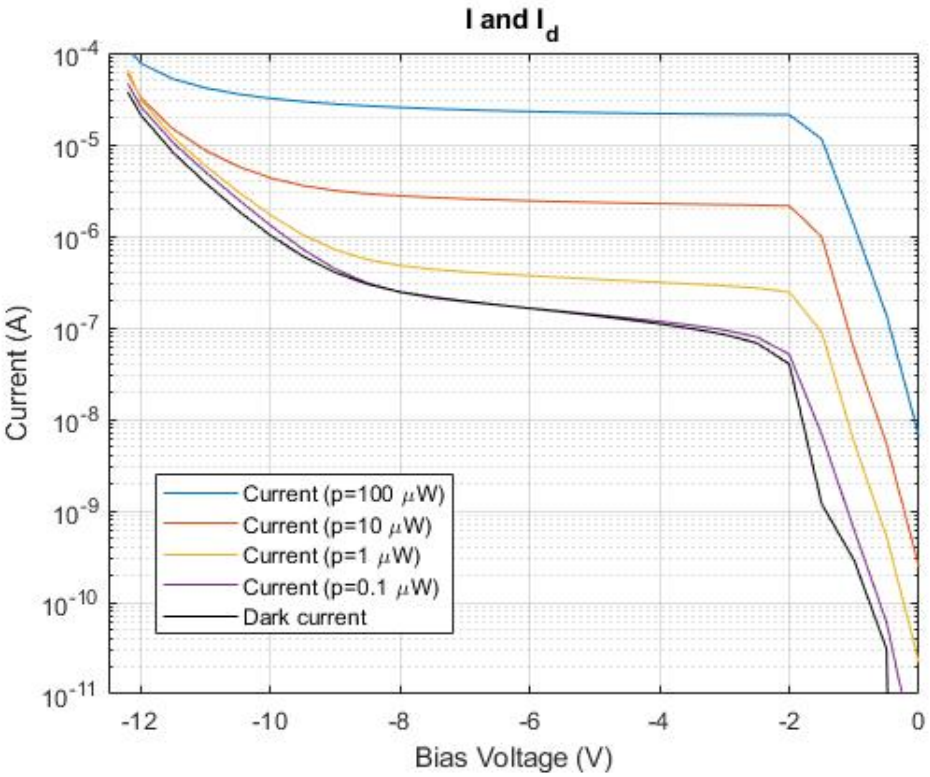

Figure 5.19: Current (for different input powers) and dark current as a function of applied bias voltage. $\lambda = 1550nm$.

As expected, increasing the input power increases the generated photocurrent (I_p), and therefore the current (I). Results suggest a breakdown voltage of approximately −12.2 V. Breakdown voltage is obtained by sweeping the bias voltage and monitoring the simulation convergence. The simulation diverges once the applied bias exceeds the breakdown voltage. The step size is reduced as the voltage approaches the breakdown voltage to enhance the accuracy.

Fig. 5.20 presents photocurrent (I_p) as a function of input power, for $V = -12V$ near breakdown voltage, and $V = -4$ where unity gain is demonstrated (results for multiplication gain is presented in section 5.3.5).

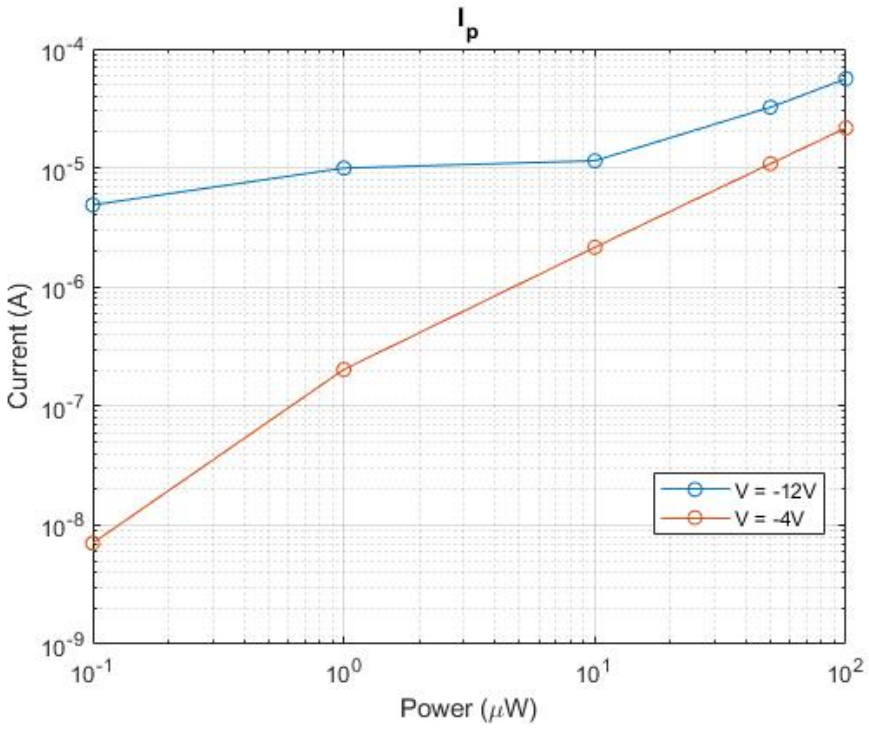

Figure 5.20: Photocurrent as a function of input power for $V = -12V$ and $V = -4V$. $\lambda = 1550nm$.

5.3.4 Responsivity

By using the obtained results for current and implementing the input optical power, responsivity as a function of applied bias voltage is obtained (Fig. 5.21).

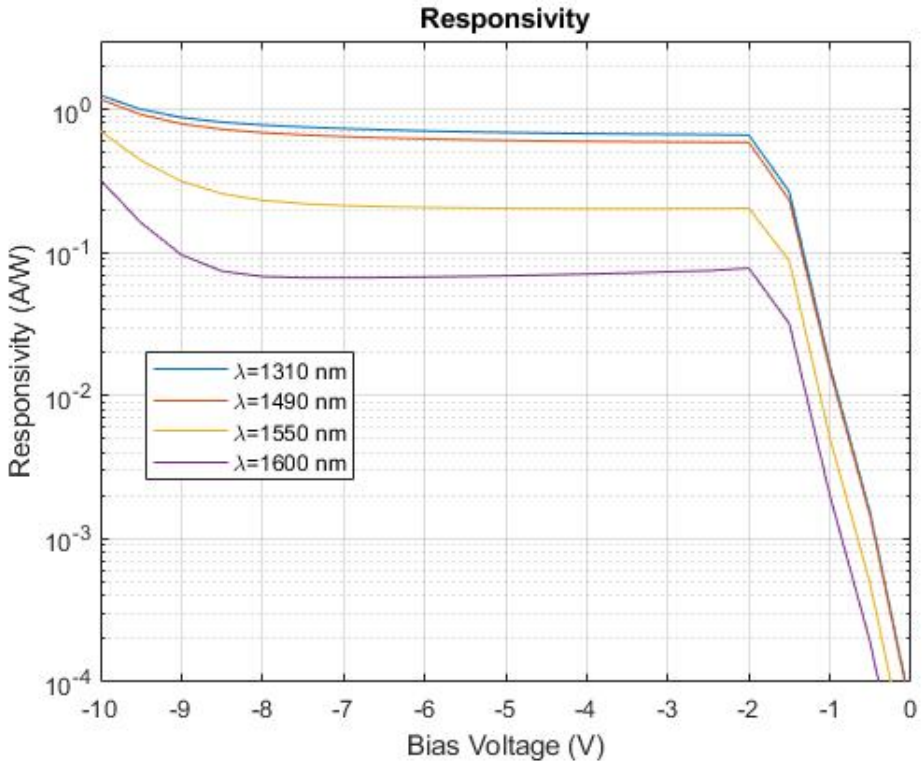

Figure 5.21: Responsivity vs Applied Reverse Bias Voltage for four different wavelengths.

The device demonstrates a higher responsivity at 1310 nm and 1490 nm, and a lower responsivity at 1610 nm, for all voltages. The observed influence of wavelength on responsivity is directly related to the absorption coefficient profile of germanium. The effect of wavelength on responsivity is further demonstrated in Fig. 5.22, where we acquired responsivity as a function of wavelength for two different bias voltages.

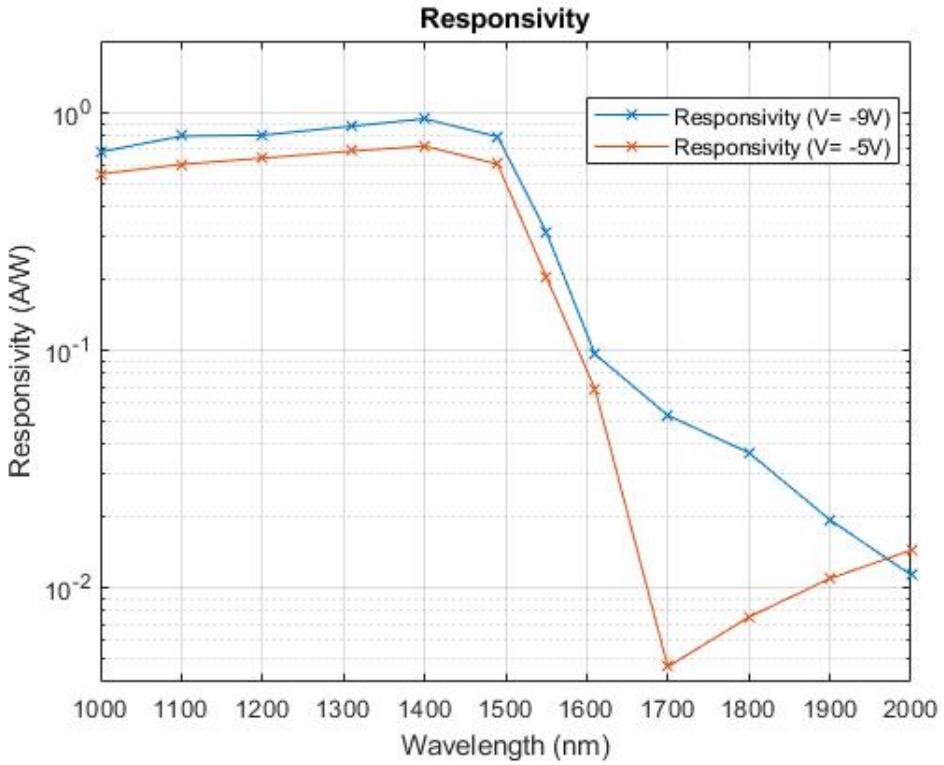

Figure 5.22: Responsivity vs Wavelength for $V = -9V$ and $V = -5V$. Input power = $1\mu W$.

To evaluate these results, we refer to optical simulations performed in FDTD. Fig. 5.23 illustrates the normalized absorbed power as a function of wavelength. The results for responsivity (Fig. 5.22) match the absorption profile at both $V = -9V$ and $V = -5V$. The exception seems to be between $\lambda = 1700nm$ and $\lambda = 2000nm$ for $V = -5V$, where there is a minor increase in responsivity. This can be attributed to the generation rate at these wavelengths being insignificant, which makes the photocurrent comparable to dark current and therefore the results more sensitive to the accuracy. Nevertheless, the negligible responsivity in this regime meets our expectations, ranging from 0.0046 A/W to 0.0143 A/W. The responsivity is 0.2034 A/W at $\lambda = 1550nm$ and 0.6875 A/W at $\lambda = 1310nm$ (for $V = -5V$).

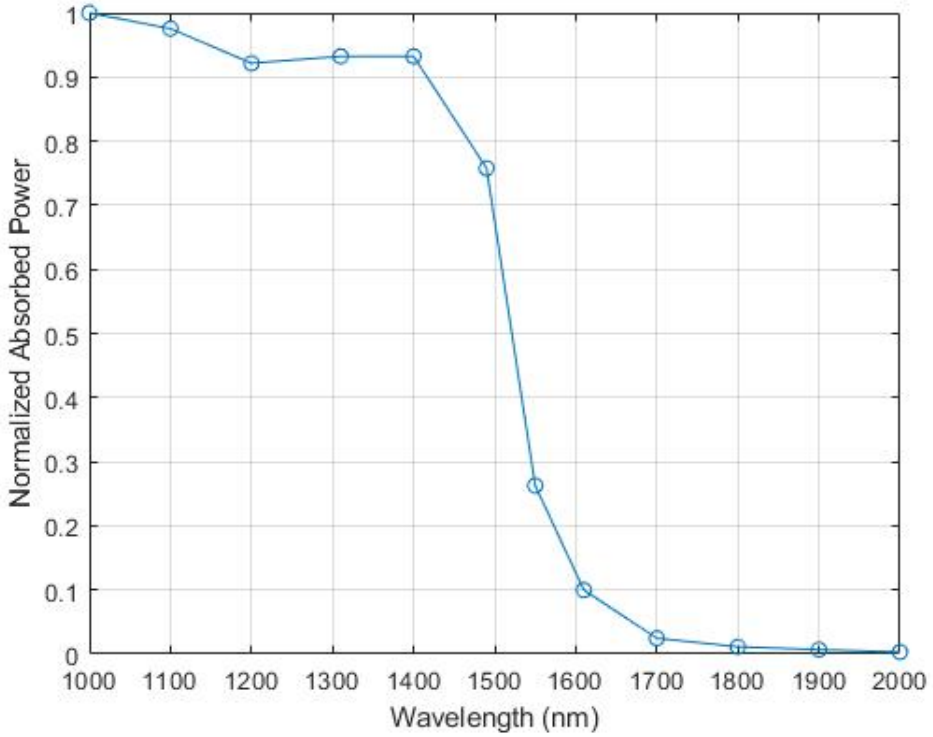

Figure 5.23: Normalized absorbed power derived in FDTD as a function of wavelength.

5.3.5 Multiplication Gain

Obtaining the multiplication gain is an essential part of evaluating the performance of an avalanche photodiode. Fig. 5.24 shows the obtained multiplication gain (M) as a function of bias voltage.

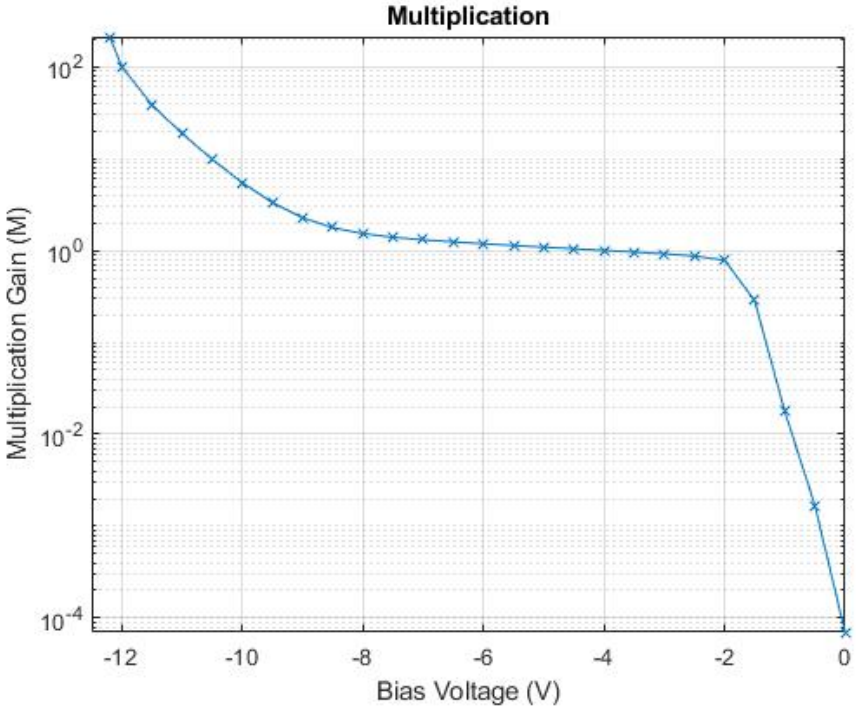

Figure 5.24: Gain as a function of applied bias voltage.

The gain increases significantly as the device approaches breakdown. A maximum gain of 210.66 is reported at $V = -12.2V$.

5.3.6 Transient Response and Bandwidth

We obtain the speed of the device by performing transient simulation. The simulation is initiated with no optical input to allow for the setup to stabilize. Then the input signal is turned on while the output current is being monitored. The impulse response is recorded and by performing Fourier transform, the frequency response is also derived. We begin this part by presenting our results and investigating their reliability by comparing them with other published works. We then include the convergence results for the transient simulation, by using different minimum time steps.

Results

Fig. 5.25 and 5.26 show the impulse response and 3dB bandwidth at V = $-9V$.

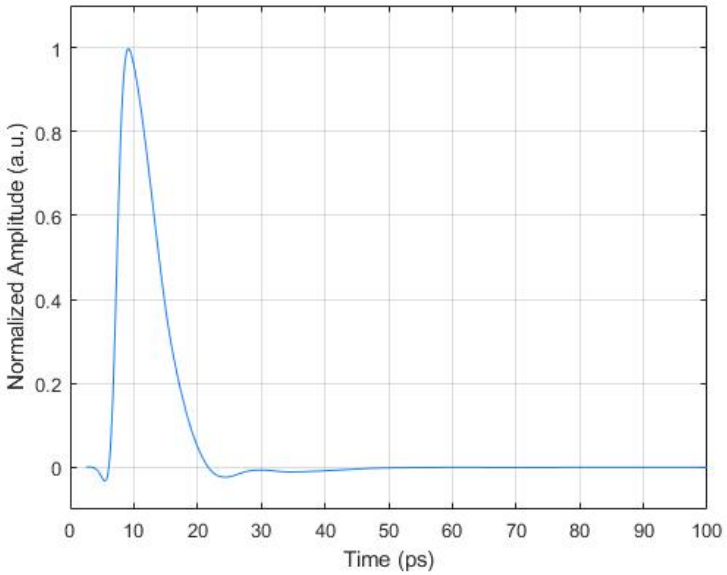

Figure 5.25: Impulse response at V= $-9V$.

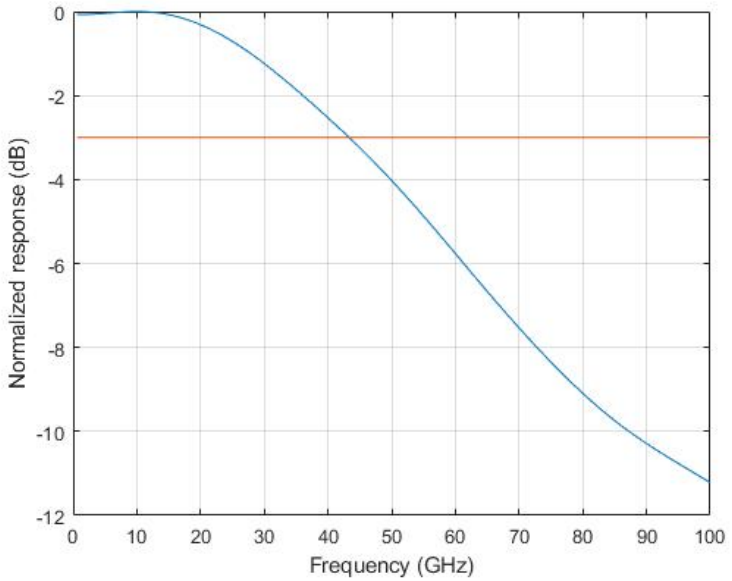

Figure 5.26: 3dB bandwidth for V= $-9V$.

Fig. 5.26 demonstrates a 3dB bandwidth of ≃ 43.3 GHz for the proposed p-i-p-i-n structure. Similarly, an exceptionally high bandwidth of 56 GHz has been reported for a comparable p-i-p-i-n structure presented by Huang et al. [43].

In another case where our results have shown close agreement to reported measurements on fabricated devices, we report a maximum 3dB bandwidth of ≃ 29 GHz for Huang et al. device (steady state simulation provided by Lumerical [1]), where they report a maximum 3dB bandwidth of ≃ 27 GHz [44].

Convergence

An important criteria when performing the transient simulation is the minimum time step. The current results are obtained with a minimum time step of 675 fs. Generally, reducing the time step will enhance the accuracy while increasing the simulation time. However, it is suggested for the time step to be larger than the electron relaxation time [7].

Doped semiconductors typically demonstrate plasma frequencies and carrier scattering rates in high microwave and terahertz frequency regimes; In

lower frequencies comparable to carrier relaxation time, the relation between carriers and field can be reliably modeled using Boltzmann transport equation coupled with Poisson's equation, since the effects of carrier transport and electromagnetic wave propagation are sufficiently decoupled [81]. However, for smaller time settings full-wave dynamics must be considered to adequately model the response [81].

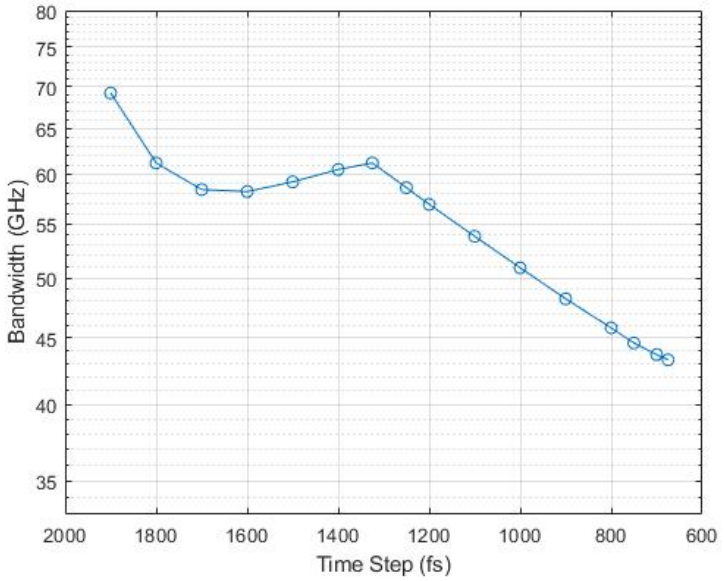

Figure 5.27: Bandwidth as a function of minimum time step.

Here bandwidth is obtained for different minimum time steps (Fig. 5.27). By applying Richardson extrapolation on the data, we derive a convergence value of 43.13 GHz for this device at $V = -9V$.

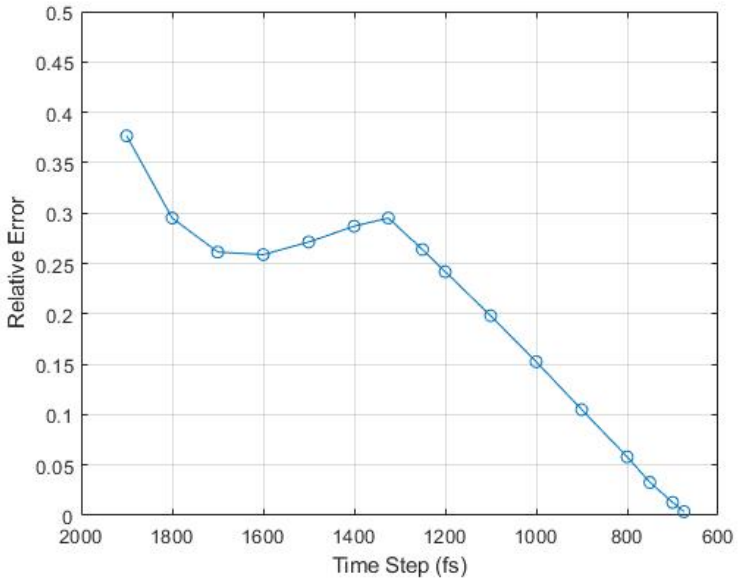

Figure 5.28: Relative error as a function of minimum time step.

5.3.7 Excess Noise Factor

In section 3.4 we presented:

$$F(M) = M \cdot k + (1-k) \cdot (2 - \frac{1}{M}) \tag{5.4}$$

Multiplication gain (M) has been previously obtained for each bias voltage in section 5.3.5. In order to estimate the k-value at each voltage, we use the following model which is also used by Lumerical [75]:

$$k = \Gamma_i \cdot \exp(\frac{-\beta_i}{|E|}) \tag{5.5}$$

This model utilizes charge multiplication measurements on diffused silicon p-n junctions, in order to calculate the ionization rates, α and β. Here for $E > 4\times10^5$ (V/cm), $\Gamma_1 = 0.955$ and $\beta_1 = 4.62\times10^5$ (V/cm), and for $E < 4\times10^5$ (V/cm), $\Gamma_2 = 2.25$ and $\beta_2 = 8.05 \times 10^5$ (V/cm) [75]. Regarding electric field, since impact ionization rates α and β have an exponential dependence on E, the major contribution to ionization integral emerges from fields close to the

maximum electric field E_m. Therefore, k can be associated with an electric field $E = cE_m$ where c is expected to be near unity; Using $c = 0.9$ in performed computations has demonstrated close agreement to measurements [75].

We use the obtained electric field simulation results (Fig. 5.17) to derive E_m and E (58410 data points at each voltage). We limit our data to the avalanche layer and only implement the electric field in the intrinsic silicon region. Table 5.4 shows the obtained $|E|$ and k-value for each voltage and multiplication gain.

Bias Voltage (V)	Multiplication Gain	$\|E\|$ ($\times 10^5$ V/cm)	k
-4	1	3.3461	0.2029
-4.5	1.0408	3.4106	0.2124
-5	1.0838	3.4773	0.2222
-5.5	1.1303	3.5462	0.2324
-6	1.1811	3.6173	0.2663
-6.5	1.2374	3.6905	0.2731
-7	1.3029	3.7656	0.2800
-7.5	1.3885	3.8427	0.2870
-8	1.5217	3.9216	0.2940
-8.5	1.7670	4.0023	0.3011
-9	2.2648	4.0848	0.3082
-9.5	3.3035	4.1688	0.3153
-10	5.4422	4.2544	0.3224
-10.5	9.7652	4.3415	0.3295
-11	18.622	4.4301	0.3366
-11.5	38.3231	4.5200	0.3436
-12	99.0522	4.6112	0.3506

Table 5.4: Obtained $|E|$ and k-value at each bias voltage and multiplication gain.

Using the data shown in table 5.4 we plot the excess noise factor as a function of multiplication gain and bias voltage (Fig. 5.29 and 5.30).

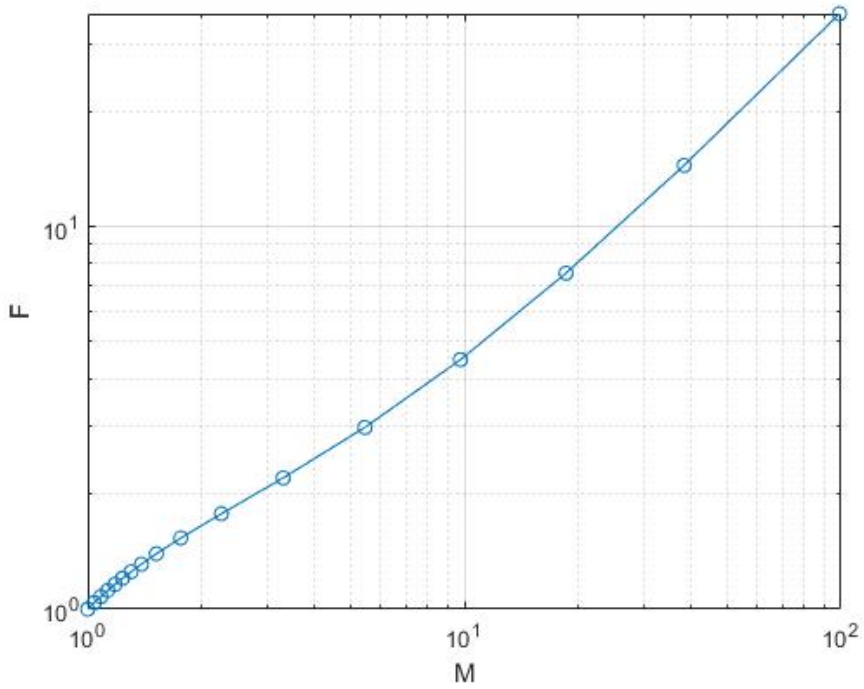

Figure 5.29: Excess noise factor as a function of multiplication gain.

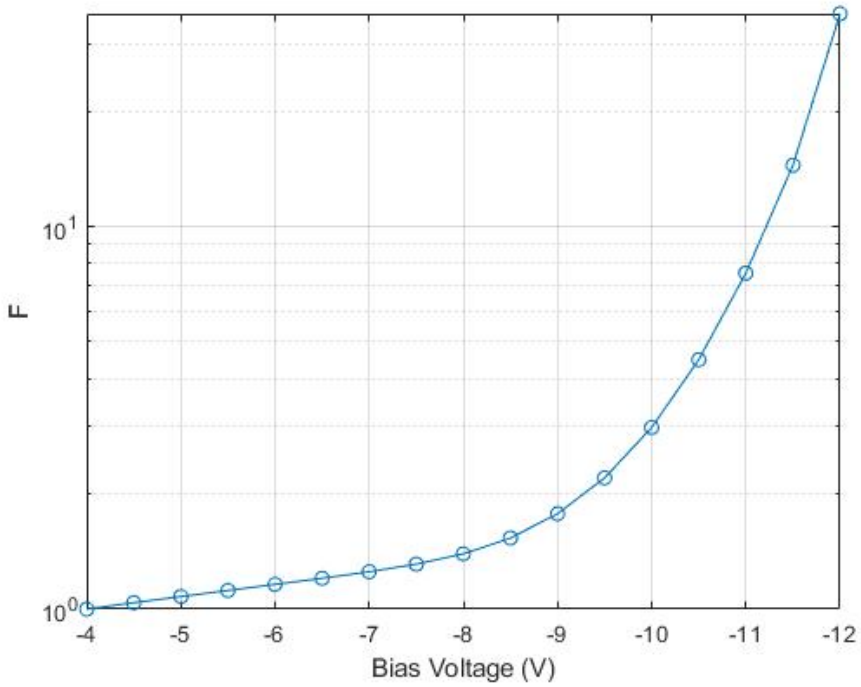

Figure 5.30: Excess noise factor as a function of applied bias voltage.

As illustrated in section 3.10, in addition to excess noise factor and k-value, other information including mean photon flux (Φ) and circuit noise parameter (σ_q) are necessary in order to determine the multiplication gain that will demonstrate maximum sensitivity. Furthermore, it should be noted that using an avalanche photodiode with $M >> 1$ will be advantageous to sensitivity if [67]:

$$\bar{m} < \frac{{\sigma_q}^2}{F-1} \tag{5.6}$$

Otherwise the APD will compromise the sensitivity by introducing excess noise [67].

Obtaining excess noise factor also enables us to implement the contribution of dark current to noise, by calculating total spectral noise current under no illumination:

$$i_N = \sqrt{2q(I_{du} + I_{dm}M^2F)B} \tag{5.7}$$

Here, $q = 1.6 \times 10^{-19}$ C, I_{du} = 110 nA, and at V= $-9V$: I_{dm} = 292 nA,

M = 2.2648, F = 1.7762, and B = 43.3 GHz. Therefore, i_N at V= $-9V$ equals to 195.92 nA.

5.3.8 Noise Equivalent Power

As mentioned earlier, in order to determine the maximum sensitivity and optimal operating gain, more information about the input signal and other noise sources is required. Noise equivalent power (NEP) provides essential information about the contribution of APD to sensitivity, as a stand-alone device. In section 3.11 we presented:

$$NEP = \frac{\sqrt{S}}{R(\lambda) \times M} \tag{5.8}$$

By this point we have been able to obtain all the parameters necessary for deriving NEP; Current, responsivity, multiplication gain, and excess noise factor are attained for every applied bias voltage. Fig. 5.31 and 5.32 show the noise equivalent power in relation to multiplication gain and applied voltage. The unity gain responsivity is 0.202 A/W and I_1 the unmultiplied current is $0.312\mu A$.

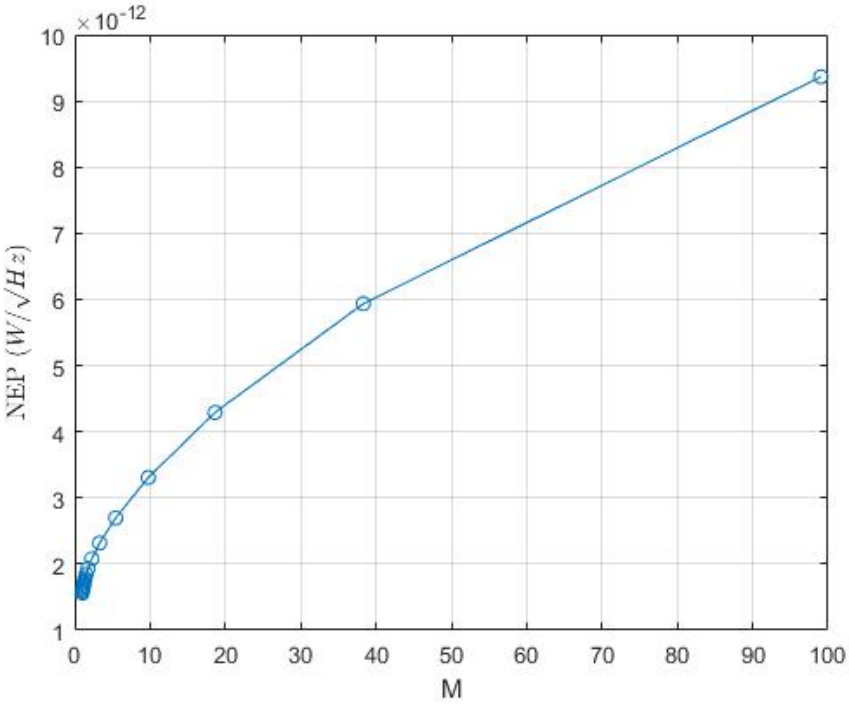

Figure 5.31: Noise equivalent power as a function of multiplication gain.

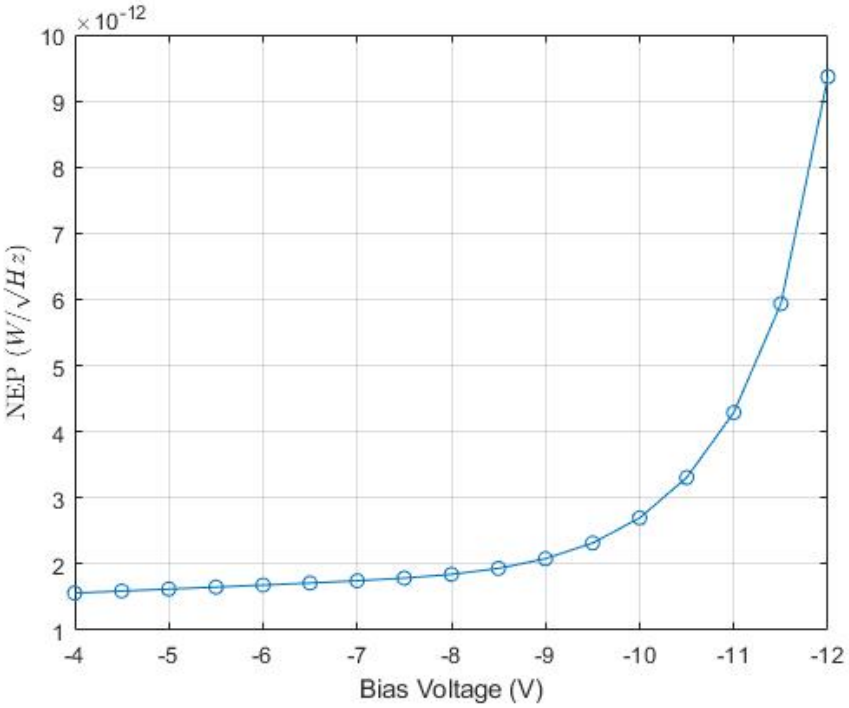

Figure 5.32: Noise equivalent power as a function of applied bias voltage.

As gain increases, excess noise factor becomes larger; This will result in higher values of NEP.

Chapter 6

Fabrication Adjustments and Optimization

In this chapter we adjust our design according to fabrication specifications provided by CMC. This enables us to offer a design which is realizable given the fabrication capacity, currently available to our group. We predict the performance parameters of the design and then proceed to optimize the device within the fabrication limitations. It should be noted that this chapter may contain classified information about the fabrication facility, effected by the NDA contract signed in October 2018.

We begin this chapter by briefly introducing the fabrication specifications. This provides the context, necessary to understand the design adjustments and performed optimization.

6.1 Fabrication Specifications

Fig. 6.1 shows a general representation of the structure we are able to fabricate. The buried oxide layer is followed by silicon and then germanium. There can be three silicon thickness levels of 220 nm, 150 nm, and 70 nm, corresponding to no etching, 70 nm etch and 130 nm etch. The germanium layer has a fixed thickness of 500 nm, and the minimum width for the structure is $3\mu m$

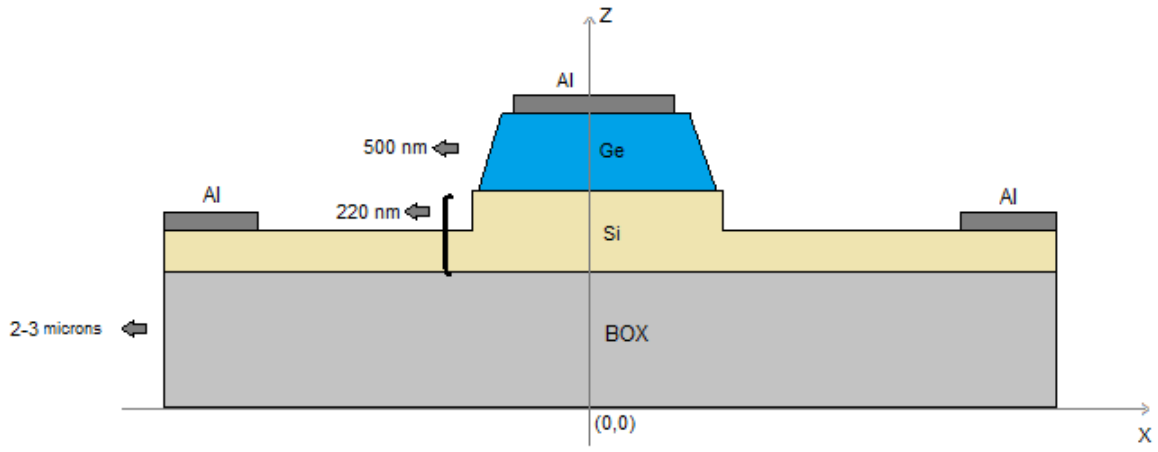

Figure 6.1: A general schematic of the device.

Doping in silicon can only vary horizontally. A vertical p-i or n-i doping is possible in germanium.

6.2 Structure

We began the design for this chapter by implementing several variants of the structure shown in Fig. 6.1, each having minor doping profile or geometric differences. The design shown in Fig. 6.2 demonstrated a superior performance which we will base our simulations and optimization on. In this design the silicon consists of three different doping types across the horizontal direction ($p++$, $p+$, and intrinsic), and the germanium has two different doping types across vertical direction ($n++$ and intrinsic). It should be noted that high doping concentration is necessary for contacts (regions 1,5, and 7). The silicon slab has a thickness of 150 nm (70 nm being etched away), and for the germanium layer we dedicated 50 nm to be $n++$ doped, leaving 450 nm of intrinsic layer.

The width of each components is illustrated in Fig. 6.3. The width

of regions 1/5 and 3 will match the width of the side electrodes and rib waveguide (in this case $1\mu m$ and $5\mu m$).

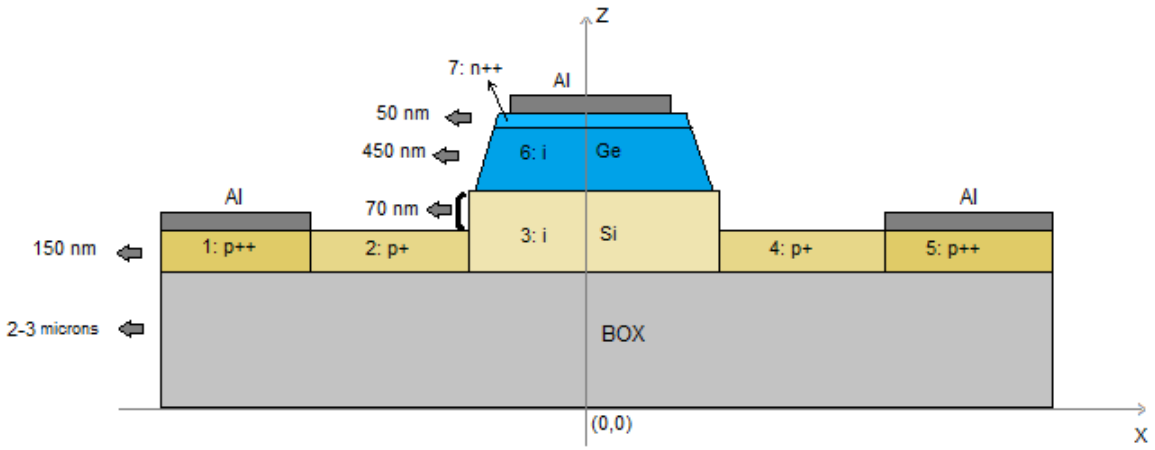

Figure 6.2: The simulated design, side view.

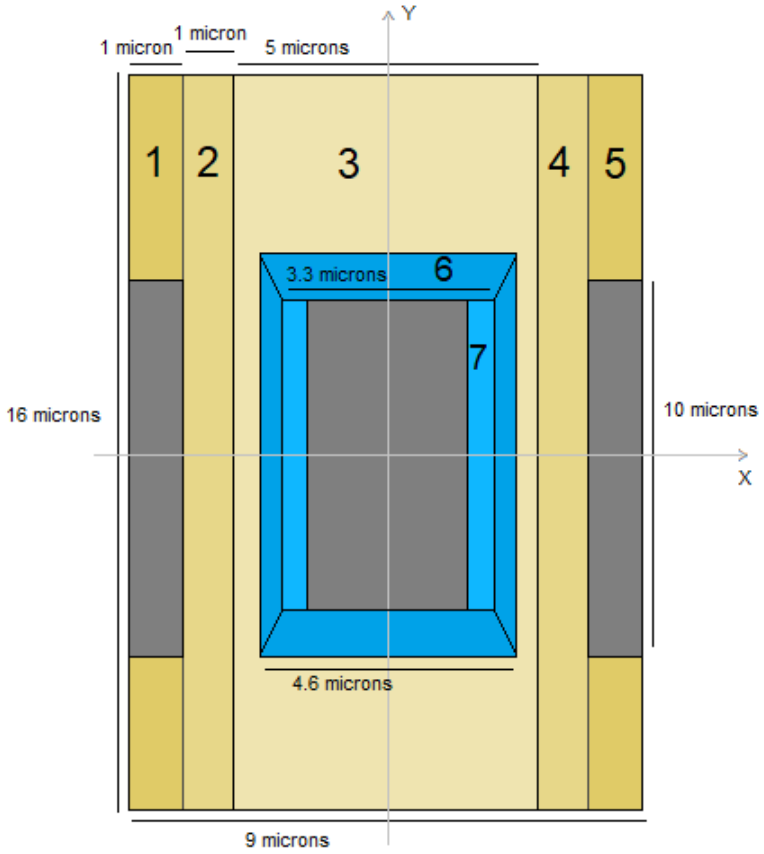

Figure 6.3: The simulated design, top view.

Fig. 6.4 shows a 3D view of the structure, implemented in Lumerical.

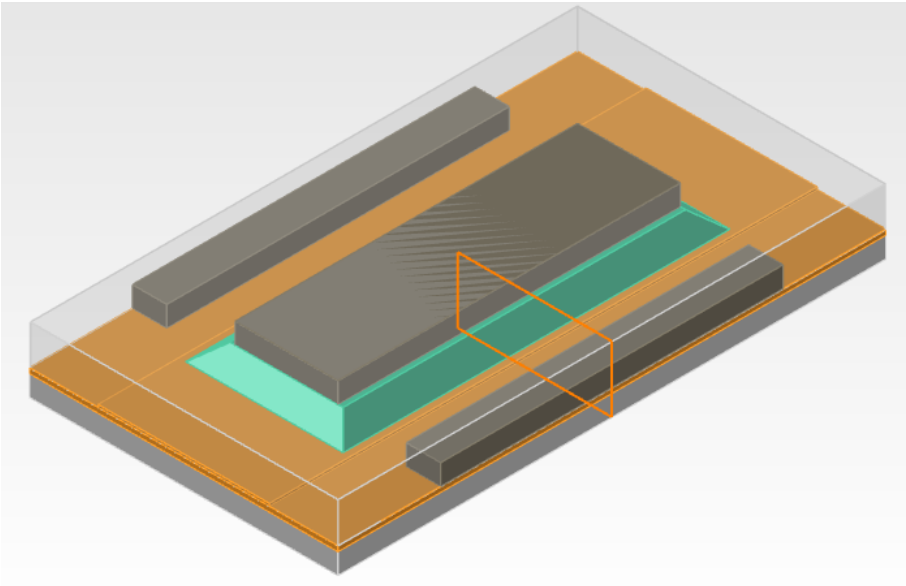

Figure 6.4: The design implemented in Lumerical, 3D view.

6.3 Results

Similar to our work in previous chapter, we utilize the FDTD module of Lumerical for optical simulation, and the DEVICE module for electrical simulation. We performed the simulations by using a similar accuracy, setting the mesh minimum edge length to 1 nm. We continue this chapter by presenting the obtained results for each parameter separately.

6.3.1 Electric Field

The results in Fig. 6.5 suggest that near breakdown voltage (at $V = -20V$), the electric field in silicon intrinsic layer surpasses 10^5 V/cm which is known as the minimum electric field necessary for avalanche impact ionization in silicon. However, unlike the SACM structure demonstrated in chapter 5, the field is not higher in the silicon layer. This is sub-optimal as having a higher field in the germanium layer will lead to unwanted band-to-band tunneling, increasing the dark current of the structure. The results also show high electric field between the intrinsic and p doped regions in silicon.

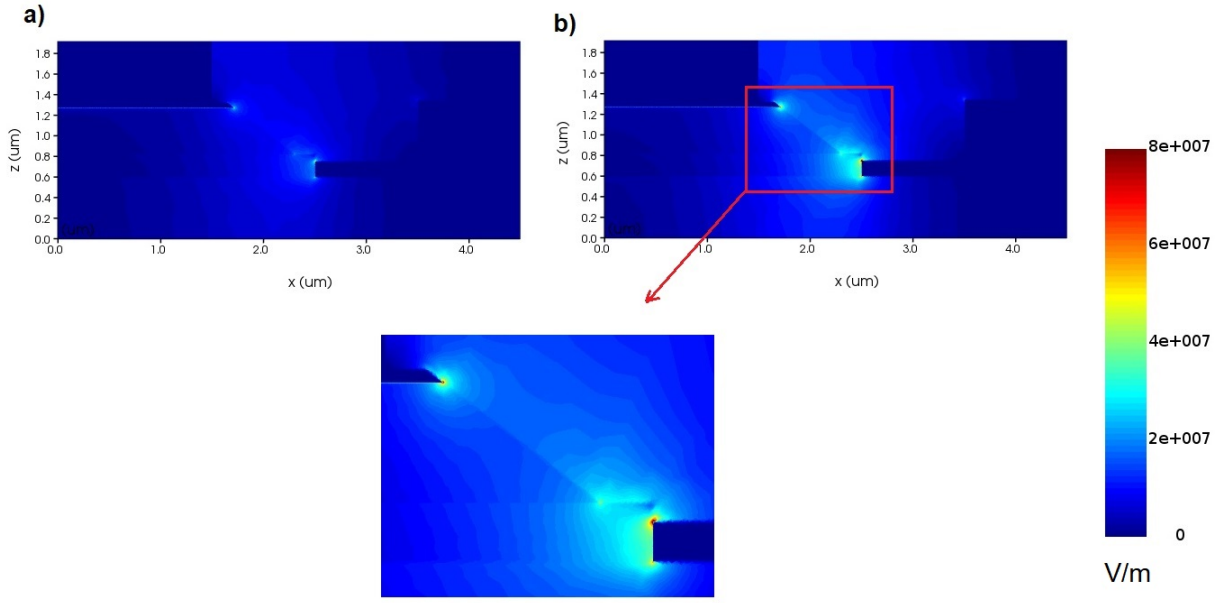

Figure 6.5: Electric field, a) at $V = -10V$ b) at $V = -20V$. Side view.

6.3.2 Current

Current of the device (for input power = $1\mu W$) and its dark component are obtained as a function of applied bias voltage. Thereafter, the dark current is deducted from the total current in order to derive the photogenerated component. Fig. 6.6 shows the photocurrent (I_p) and dark current (I_d) as a function of bias voltage. Current experiences relatively small changes as applied bias is increased, and then ascends rapidly as the device approaches breakdown. This data is used to obtain responsivity.

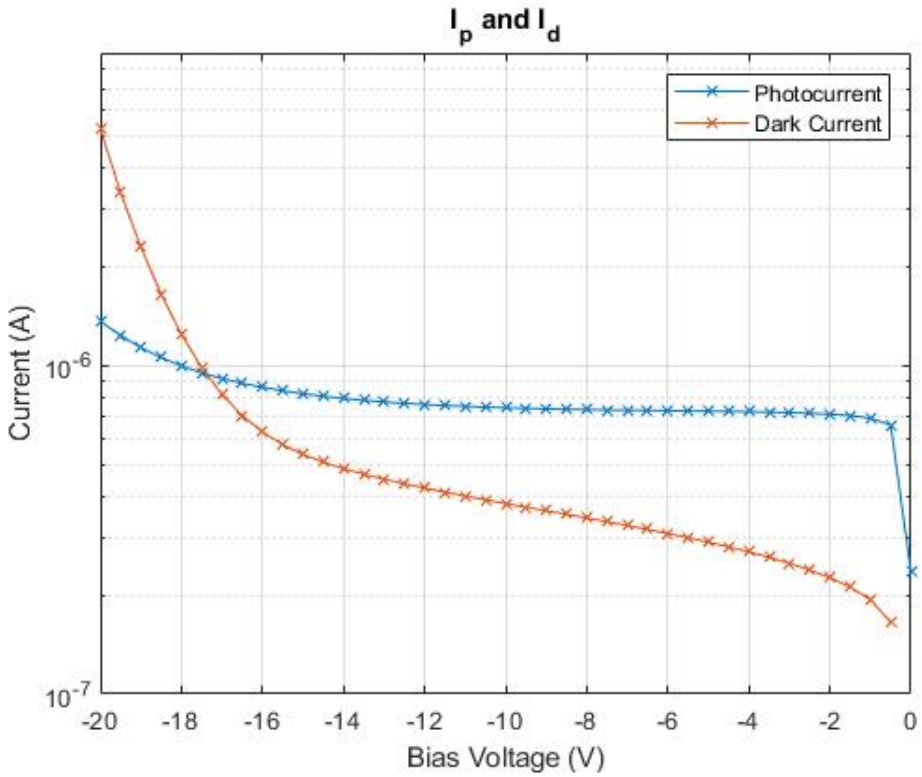

Figure 6.6: Photocurrent (for input power = $1\mu W$) and dark current as a function of applied bias voltage. $\lambda = 1550nm$.

6.3.3 Responsivity

Fig. 6.7 shows the responsivity of the structure as a function of applied bias voltage, for four different wavelengths.

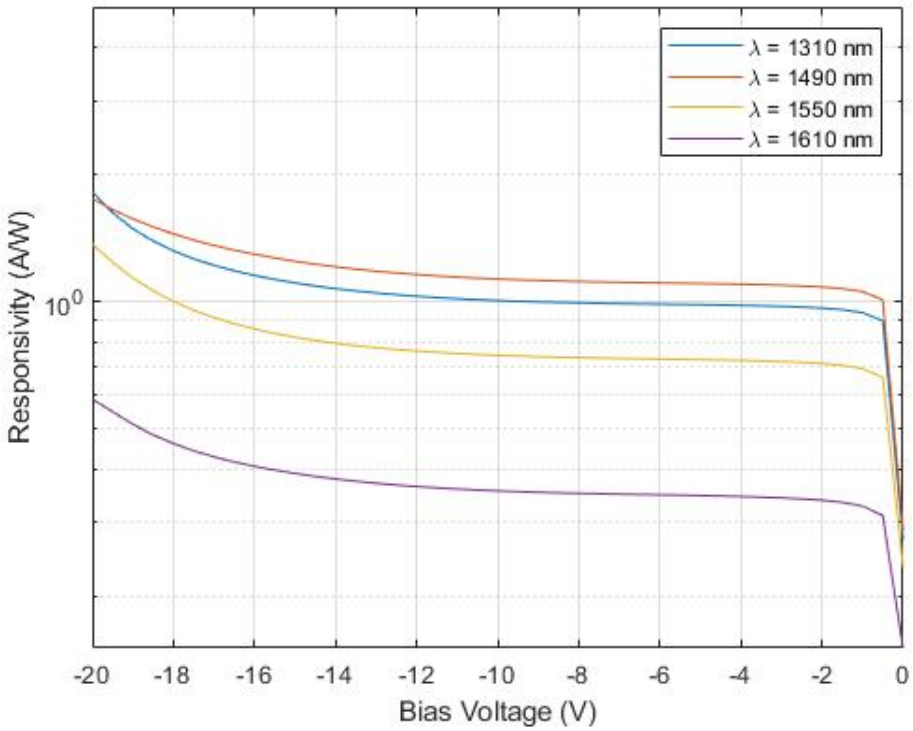

Figure 6.7: Responsivity as a function of applied bias voltage for four different wavelengths. Input power = $1\mu W$.

Compared to the operation at 1550 nm, the results show a higher responsivity for 1310nm and 1490nm, and a lower responsivity at 1610nm, which is expected. This relation between responsivity and wavelength is explained by the absorption coefficient profile of germanium. However, the responsivity at 1490 nm is slightly larger compared to 1310 nm, which doesn't match our expectations.

6.3.4 Multiplication Gain

Fig. 6.8 presents multiplication gain as a function of applied bias voltage. As expected, higher gains will be achieved near the breakdown voltage. The maximum attained multiplication gain for this setting is 6.34.

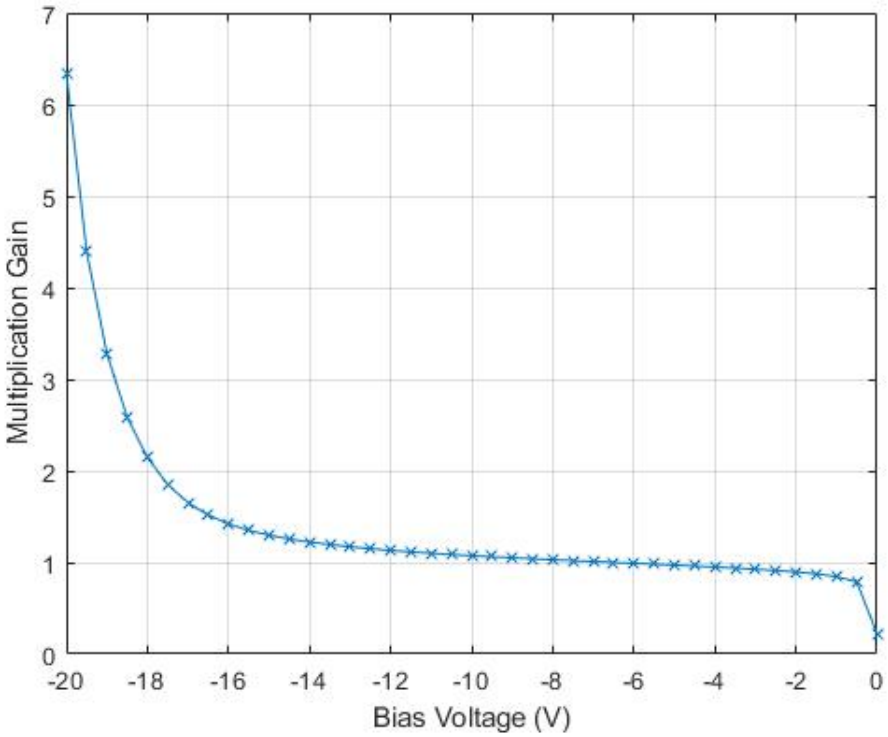

Figure 6.8: Multiplication gain as a function of applied bias voltage. λ = 1550nm, Input Power = 1μW.

6.3.5 Bandwidth

The simulation suggests a 3dB bandwidth of ≃ 17.62 GHz (Fig. 6.9). This value is lower than the bandwidth obtained for the structure in chapter 5. This is expected as in this structure the germanium layer is thicker (500nm compared to 400 nm), and carriers need to travel a longer distance to reach the electrodes. Another factor is the electric field as the higher electric field present in the structure of chapter 5, has a positive impact on the speed of the carriers.

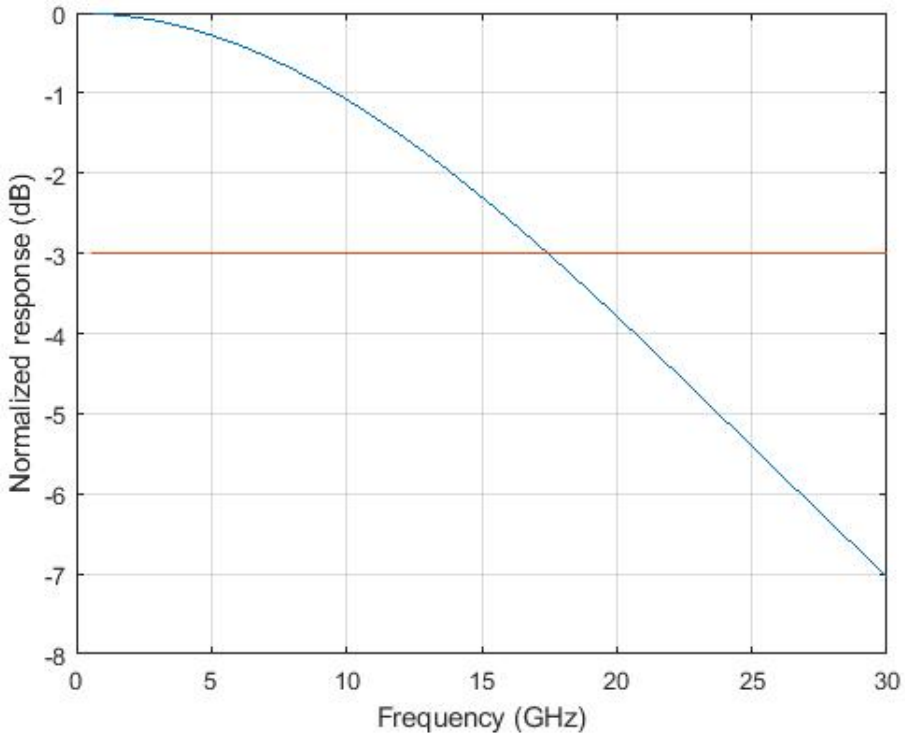

Figure 6.9: 3dB bandwidth for V = $-20V$. λ = $1550nm$ and input power = $1\mu W$.

6.4 Optimization

In this part we investigate how altering different design attributes impact the performance. These parameters are device total length, total width (fixed rib width), rib width, and doping, which are selected according to fabrication specifications. Results for steady state and transient simulations are illustrated to enable device optimization.

6.4.1 Total Length

The initial results are obtained for a length of $25\mu m$. We repeat our simulations for devices with total length of $50\mu m$, $100\mu m$, $150\mu m$, and $200\mu m$.

Photocurrent

Photocurrent is derived by deducting dark current from the total current. Fig. 6.10 illustrates the results at $V = -20V$ and $V = -10V$ for each of these devices. The results indicate that the photocurrent stops increasing for longer structures. This is explained by the effective absorption length of germanium; Device length in shorter structures is sufficient to absorb the majority of incident photons and increasing the length doesn't significantly contribute to further generation.

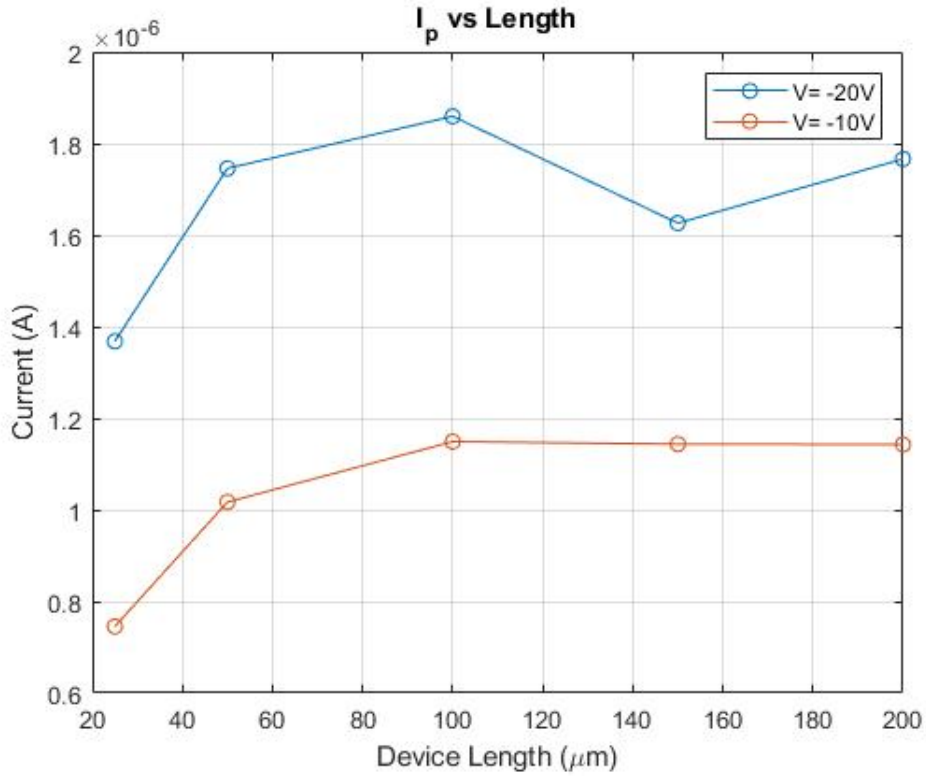

Figure 6.10: Photocurrent as a function of device total length, for $V = -20V$ and $V = -10V$. $\lambda = 1550nm$ and input power $= 1\mu W$.

Bandwidth

The transient simulation is performed near breakdown at $V = -20V$ (Fig. 6.11). The results show minor change in bandwidth as we increase the length,

scaling the device in the y direction. Changing the device dimensions in x or z directions is expected to make a more significant impact on bandwidth, as it has a stronger influence on field distribution and transit distance.

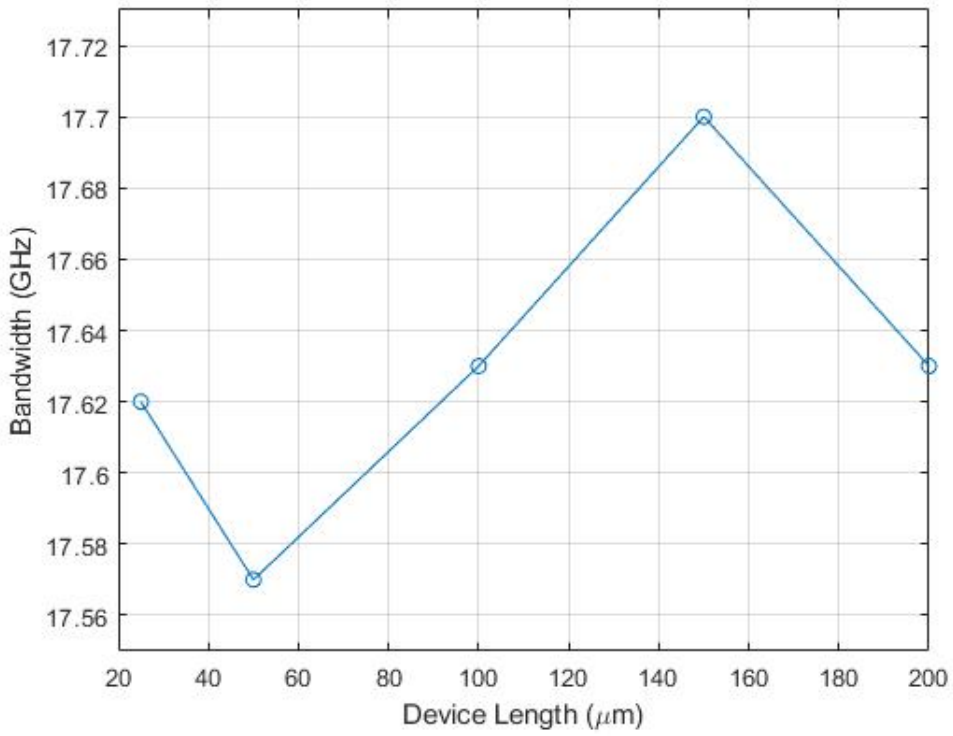

Figure 6.11: Bandwidth as a function of device total length. V = $-20V$, λ = $1550nm$, and input power = $1\mu W$.

6.4.2 Total Width

As shown in Fig. 6.3, our first design has a total width of $9\mu m$, where there is $1\mu m$ distance between the silicon rib and side electrodes. We change this value to $3\mu m$, $5\mu m$, $10\mu m$, and $15\mu m$, increasing the total width of our device to $13\mu m$, $17\mu m$, $27\mu m$, and $37\mu m$.

Photocurrent

No consistent change in photocurrent is observed for wider devices. The results are shown in Fig. 6.12.

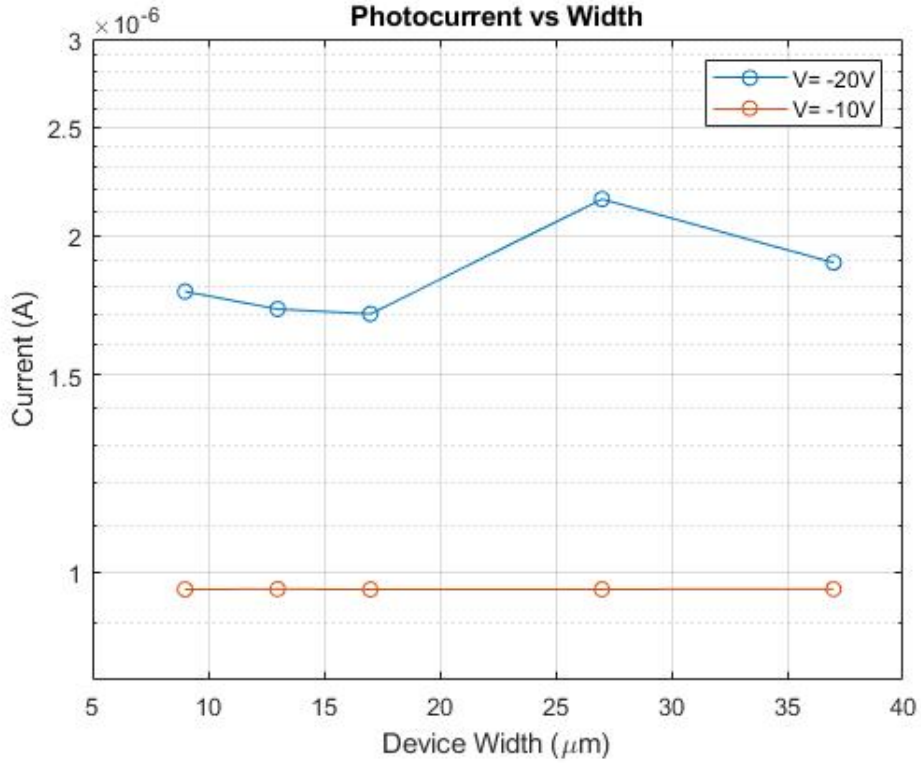

Figure 6.12: Photocurrent as a function of device total width, for $V = -20V$ and $V = -10V$. $\lambda = 1550nm$ and input power $= 1\mu W$.

Bandwidth

The bandwidth drops as we increase the total width (Fig. 6.13). This matches our expectations as the carriers transit length is increased for wider structures.

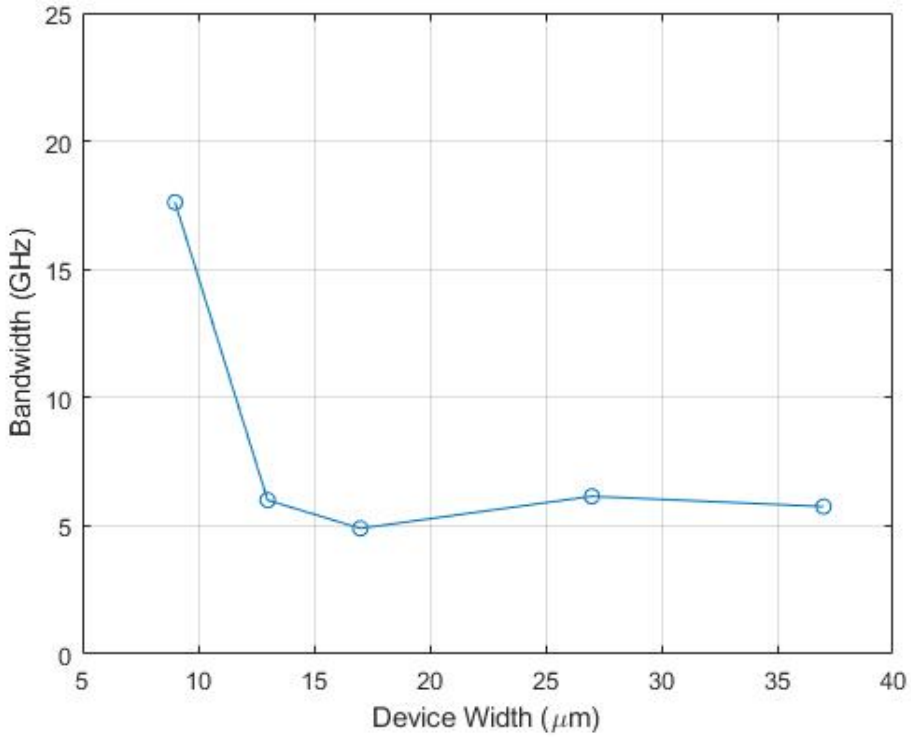

Figure 6.13: Bandwidth as a function of device total width. $V = -20V$, $\lambda = 1550nm$, and input power $= 1\mu W$.

6.4.3 Rib Width

In this part we observe how changing the rib width influences the multiplication gain and bandwidth. The rib width is changed from the previous $5\mu m$, to $7\mu m$ and $9\mu m$. Thereafter the steady state and transient results are obtained for each case.

Multiplication Gain

Results suggest that increasing the rib width slightly decreases the multiplication gain (Fig. 6.14 and 6.15). Maximum obtained gain is 3.89 for rib width of $7\mu m$ and 3.74 for rib width of $9\mu m$. As mentioned before, the maximum multiplication gain derived for rib width of $5\mu m$ is 6.34.

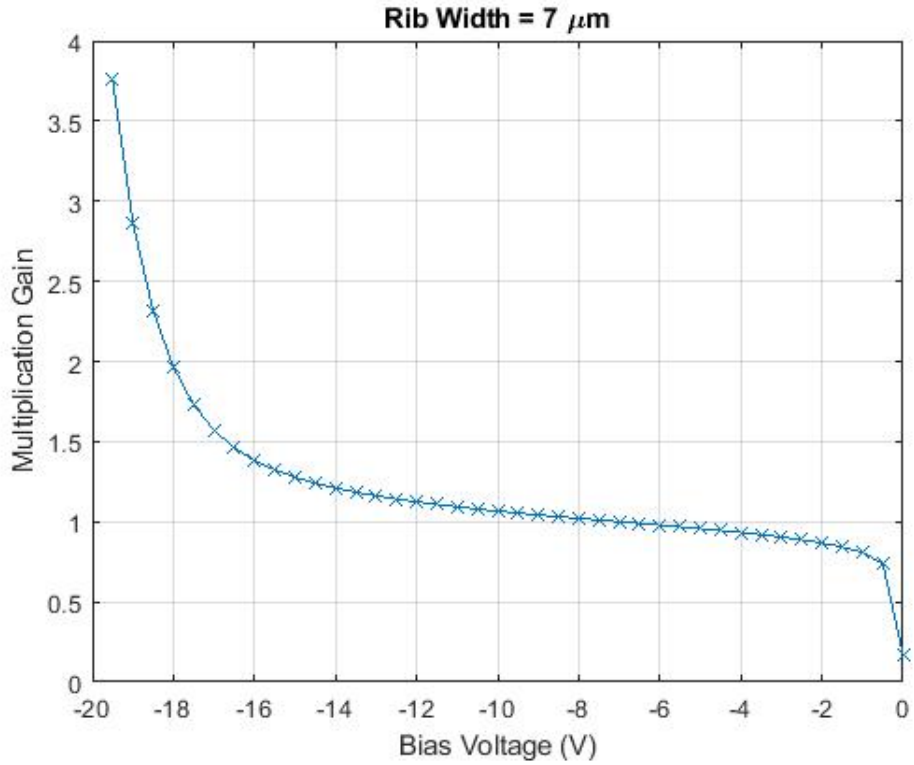

Figure 6.14: Multiplication gain as a function of applied bias voltage for rib width = $7\mu m$. $\lambda = 1550nm$ and input power = $1\mu W$.

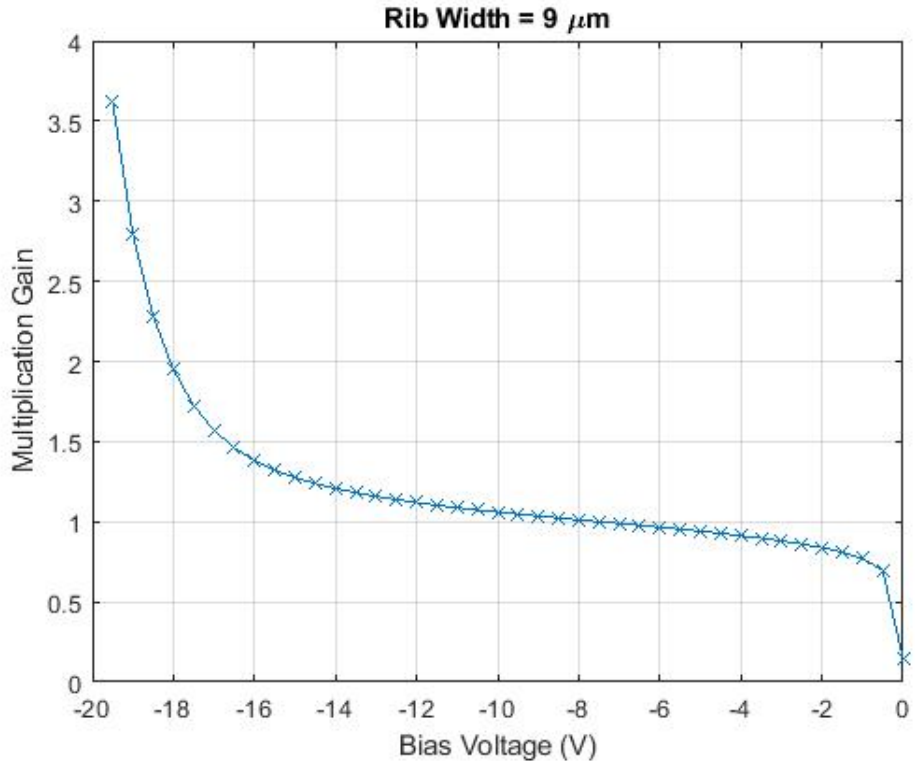

Figure 6.15: Multiplication gain as a function of applied bias voltage for rib width = $9\mu m$. $\lambda = 1550nm$ and input power = $1\mu W$.

Bandwidth

Results demonstrate that increasing the rib width significantly reduces the speed (Fig. 6.16 and 6.17); Bandwidth is ≃ 3.15 GHz for rib width of $7\mu m$ and ≃ 1.35 GHz for rib width of $9\mu m$. Previously a considerably larger bandwidth of ≃ 17.62 GHz has been achieved with a rib width of $5\mu m$.

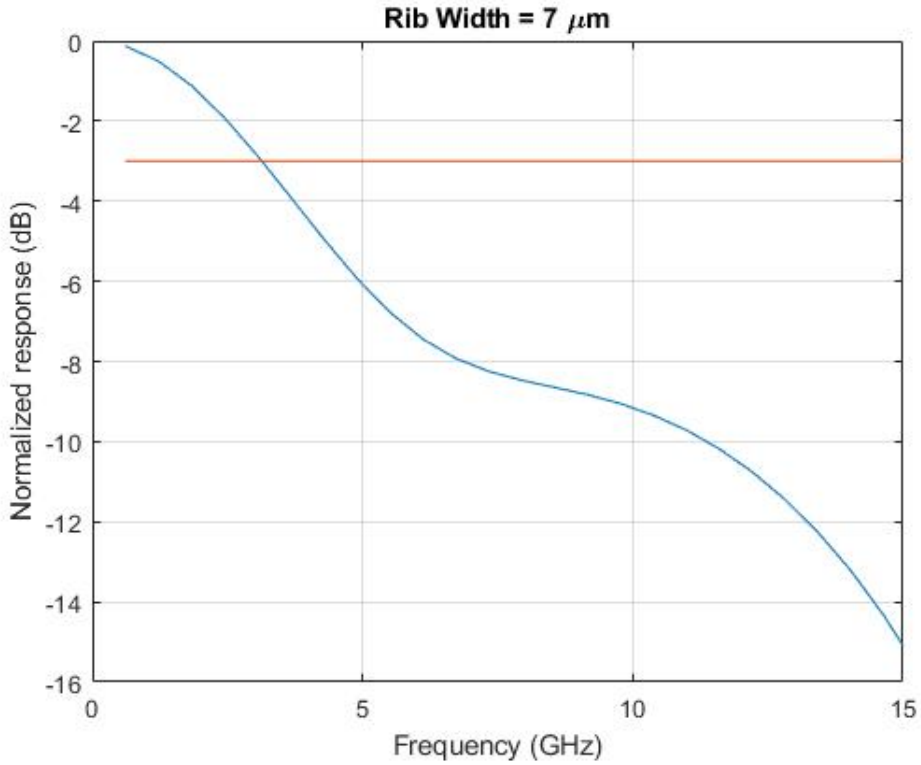

Figure 6.16: 3dB bandwidth for rib width = $7\mu m$. V = $-20V$, λ = $1550nm$, and input Power = $1\mu W$.

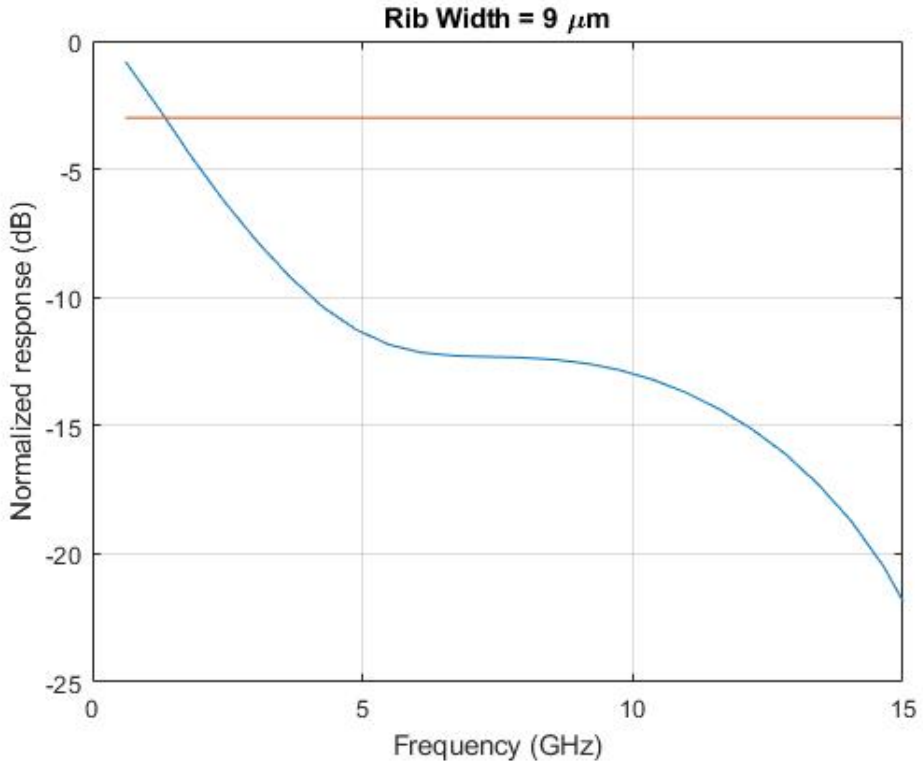

Figure 6.17: 3dB bandwidth for rib width = $9\mu m$. V = $-20V$, λ = $1550nm$, and input power = $1\mu W$.

6.4.4 Doping

The doping of the intrinsic silicon layer in Fig. 6.2 is changed to p doping which changes the breakdown voltage to $\simeq -7.5V$. Again, we observe the impact on multiplication gain and bandwidth.

Multiplication Gain

The multiplication gain as a function of applied bias voltage is shown in Fig. 6.19. This structure demonstrates a maximum gain of 14.86. We continue by deriving the gain-bandwidth product for this structure.

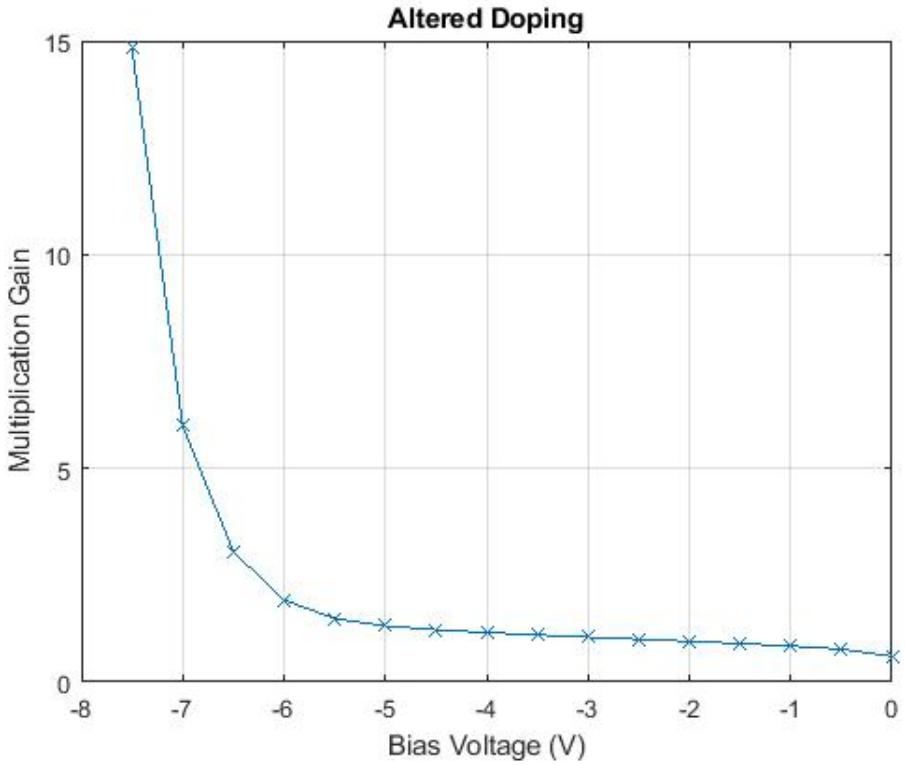

Figure 6.18: Multiplication gain as a function of applied bias voltage for structure with altered doping. $\lambda = 1550nm$ and input power $= 1\mu W$.

Bandwidth

Transient simulation is also performed for the structure. This device is faster having a 3dB bandwidth of $\simeq$ 21.37 GHz compared to the previous $\simeq$ 17.62 GHz (Fig. 6.19).

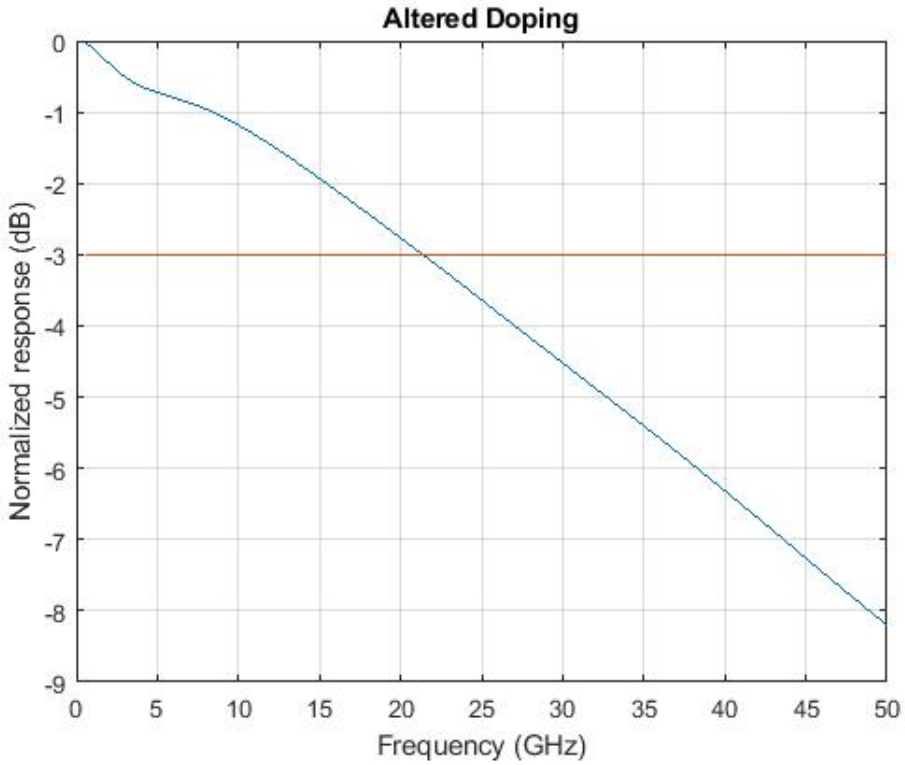

Figure 6.19: 3dB bandwidth for structure with altered doping. $V = -7.5V$, $\lambda = 1550nm$, and input power $= 1\mu W$.

6.4.5 Gain-bandwidth product

Gain-bandwidth product is obtained for the structure introduced in section 6.4.4, where the intrinsic silicon layer is replaced with p doping. Several variations of the structure with different lengths and rib widths are implemented, and gain and bandwidth are derived for each case.

Length

Fig. 6.20 illustrates the gain-bandwidth product as a function of device length, starting from $20\mu m$.

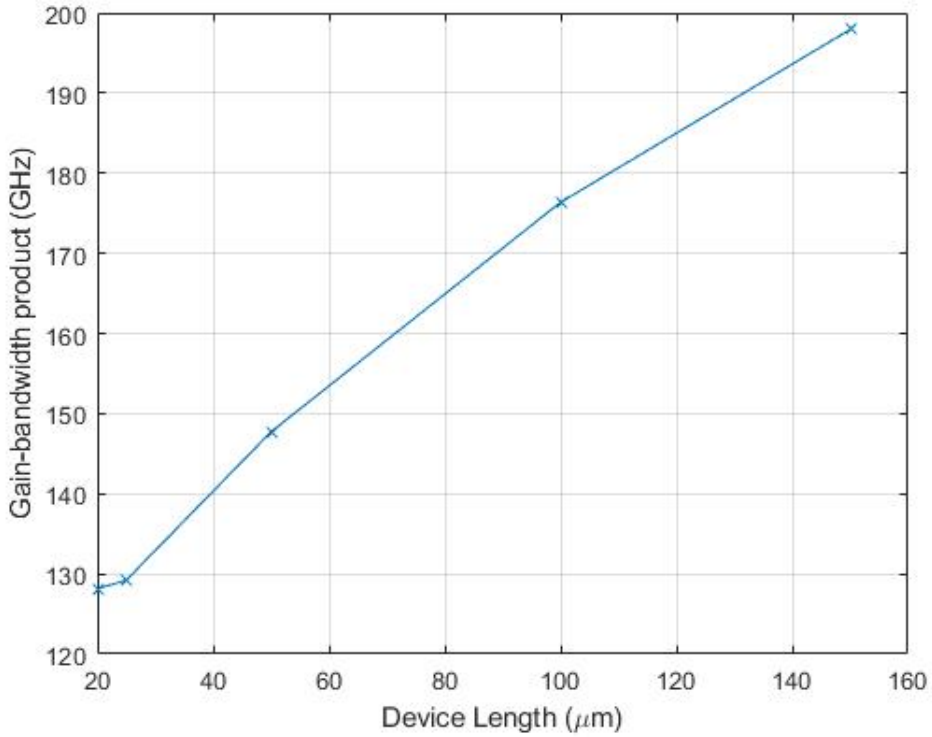

Figure 6.20: Gain-bandwidth product as a function of device length. V = $-7V$, $\lambda = 1550nm$, and input power = $1\mu W$.

The gain-bandwidth product increases with length, due to increase in multiplication gain and despite the drop in bandwidth. This is while in similar works the germanium length is set to $25\mu m$ or less [28]. Our results suggest that the increased multiplication gain after $25\mu m$ is mainly due to increase in dark current; A consistent increase in dark current as a function of length, has been previously reported for a similar device [23].

Rib Width

Fig. 6.21 demonstrates the gain-bandwidth product as a function of rib width. Given the fabrication constraints 5 μm is the minimum feasible rib width.

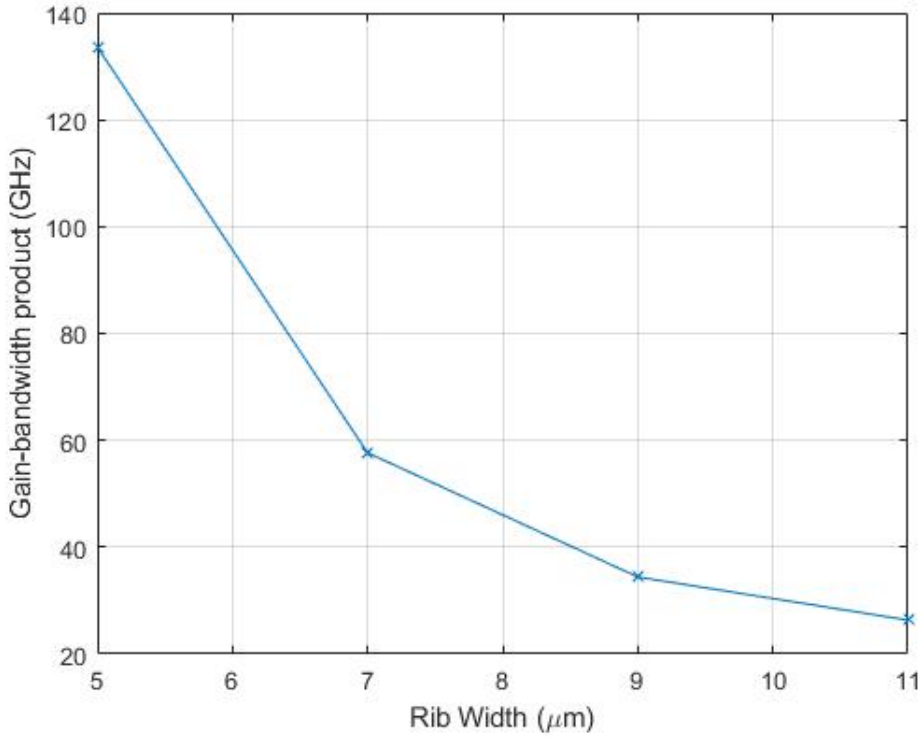

Figure 6.21: Gain-bandwidth product as a function of rib width. $V = -7$, $\lambda = 1550nm$, input power $= 1\mu W$, and total length $= 25\mu m$.

The highest gain-bandwidth product is achieved for the minimum rib width. This is expected as both gain and bandwidth drop for wider devices.

Considerations

Regarding the obtained gain-bandwidth product, it is important to note the following: First, our calculations for multiplication gain include the dark current (see Appendix A). This can lead to overestimation of gain and therefore gain-bandwidth product, especially in devices with high dark current. Second, the results are obtained near breakdown which doesn't necessarily correspond to optimal operating voltage. Moreover, bandwidth is expected to drop for higher gains due to avalanche build-up time and the accuracy of predictions regarding gain-bandwidth trade-off is important in this case; While regarding maximum bandwidth, we have demonstrated close agree-

ments between our predictions and fabricated devices performance, the drop in bandwidth as a function of gain also plays a critical role in the anticipated gain-bandwidth value.

6.4.6 Conclusion

The optimization results suggest that the photocurrent doesn't increase for longer devices (dark current does), while increasing the total width impacts the bandwidth in a negative way. Moreover, increasing the rib width decreases the multiplication gain and bandwidth. Therefore, using smaller dimensions for total length, total width, and rib width is suggested. These observations agree with our understanding about the dynamics of the photodiode and provides a useful guideline in determining the design before fabricating. Also a higher bandwidth is attained by replacing the intrinsic silicon layer with a p doped one. This suggests that further improvement to performance is feasible by adjusting the design.

Chapter 7

Conclusion

In this thesis, we demonstrated the capacity to reliably model the steady state and transient operation of a photodiode, using Lumerical. A silicon germanium SACM waveguide avalanche photodiode was proposed and simulated, and its critical peformance parameters including current, responsivity, multiplication gain, excess noise factor, and bandwidth was obtained. We illustrated close agreement between our results and measurements reported on fabricated devices, in multiple cases. We also studied the reliability of our results by applying convergence test, using different mesh settings and Richardson extrapolation.

The utility of our work was further developed by investigating the dependency of performance on operating wavelength and input power, and design parameters such as avalanche layer thickness. We eventually utilized our methods to model and optimize a design, attainable according to the fabrication capacity available to our group at the time.

For the future, silicon germanium SACM waveguide avalanche photodiodes are a promising choice for meeting the requirements in optical access networks. There seems to be a substantial room for design improvements in these devices, leading to better performances.

By accurately predicting the performance of this device before its fabrication, we are able to make a significant contribution to making better receivers in optical networks. This work can be applied similarly, to other types of avalanche and pin photodiodes, benefiting a vast range of applications.

Bibliography

[1] 10-V Ge-on-Si APD with Si multiplication. www.kb.lumerical.com/en/photodetectors_avalanche-photodetector.html. Accessed: 2018-10-08.

[2] Avalanche Photodiode Receiver Performance Metrics. www.voxtel-inc.com/files/2012/07/TECH-NOTE-V803-Avalanche-Photodiode-and-Receiver-Performance-Metrics-By-GM-Williams-VOXTEL_B.pdf. Accessed: 2018-11-12.

[3] Carrier Generation and Recombination. www.iue.tuwien.ac.at/phd/entner/node11.html. Accessed: 2018-10-11.

[4] Fiber Optics understanding the basics. www.photonics.com/Articles/Fiber_Optics_Understanding_the_Basics/a25151. Accessed: 2018-10-06.

[5] NEP – Noise Equivalent Power. www.thorlabs.com/images/TabImages/Noise_Equivalent_Power_White_Paper.pdf. Accessed: 2018-11-12.

[6] New Services Are Driving Bandwidth Requirements. www.alliedtelesis.com/solutions/fttx. Accessed: 2018-10-06.

[7] Selecting Parameter in Transient Simulation in DEVICE. www.kx.lumerical.com/t/selecting-parameter-in-transient-simulation-in-device/1294/2. Accessed: 2018-11-12.

[8] Vertical photodetector. www.kb.lumerical.com/en/pic_photodetectors_vertical_photodetector.html. Accessed: 2018-10-08.

[9] Aryan Afzalian and Denis Flandre. Measurements, modelling and electrical simulations of lateral pin photodiodes in thin film-soi for high quantum efficiency and high selectivity in the uv range. In *European Solid-State Device Research, 2003. ESSDERC'03. 33rd Conference on*, pages 55–58. IEEE, 2003.

[10] Aryan Afzalian and Denis Flandre. Physical modeling and design of thin-film soi lateral pin photodiodes. *IEEE Transactions on Electron Devices*, 52(6):1116–1122, 2005.

[11] Aryan Afzalian and Denis Flandre. Characterization of quantum efficiency, effective lifetime and mobility in thin film ungated soi lateral pin photodiodes. *Solid-State Electronics*, 51(2):337–342, 2007.

[12] Donghwan Ahn, Ching-yin Hong, Jifeng Liu, Wojciech Giziewicz, Mark Beals, Lionel C Kimerling, Jurgen Michel, Jian Chen, and Franz X Kärtner. High performance, waveguide integrated ge photodetectors. *Optics express*, 15(7):3916–3921, 2007.

[13] Hiroaki Ando, Hiroshi Kanbe, Tatsuya Kimura, Toyoshi Yamaoka, and Takao Kaneda. Characteristics of germanium avalanche photodiodes in the wavelength region of 1-1.6 μm. *IEEE Journal of Quantum Electronics*, 14(11):804–809, 1978.

[14] David E Aspnes and AA Studna. Dielectric functions and optical parameters of si, ge, gap, gaas, gasb, inp, inas, and insb from 1.5 to 6.0 ev. *Physical review B*, 27(2):985, 1983.

[15] Amitabha Banerjee, Youngil Park, Frederick Clarke, Huan Song, Sunhee Yang, Glen Kramer, Kwangjoon Kim, and Biswanath Mukherjee. Wavelength-division-multiplexed passive optical network (wdm-pon) technologies for broadband access: a review. *Journal of optical networking*, 4(11):737–758, 2005.

[16] C.J. Brabec, V. Dyakonov, J. Parisi, and N.S. Sariciftci. *Organic Photovoltaics*. Springer, 2003.

[17] Steven J Byrnes. Multilayer optical calculations. *arXiv preprint arXiv:1603.02720*, 2016.

[18] Joe C. Campbell. Recent advances in avalanche photodiodes. *J. Lightwave Technol.*, 34(2):278–285, Jan 2016.

[19] Philippe Chanclou, Stephane Gosselin, J Fernandez Palacios, V Lopez Alvarez, and Evi Zouganeli. Overview of the optical broadband access evolution: a joint article by operators in the ist network of excellence e-photon/one. *IEEE Communications Magazine*, 44(8):29–35, 2006.

[20] Jiajia Chen, Lena Wosinska, Carmen Mas Machuca, and Monika Jaeger. Cost vs. reliability performance study of fiber access network architectures. *IEEE Communications Magazine*, 48(2):56–65, 2010.

[21] AG Chynoweth. Ionization rates for electrons and holes in silicon. *physical review*, 109(5):1537, 1958.

[22] Stephane Demiguel, Ning Li, Xiaowei Li, Xiaoguang Zheng, Jooyong Kim, Joe C Campbell, Hanfei Lu, and Alex Anselm. Very high-responsivity evanescently coupled photodiodes integrating a short planar multimode waveguide for high-speed applications. *IEEE Photonics Technology Letters*, 15(12):1761–1763, 2003.

[23] Christopher T DeRose, Douglas C Trotter, William A Zortman, Andrew L Starbuck, Moz Fisher, Michael R Watts, and Paul S Davids. Ultra compact 45 ghz cmos compatible germanium waveguide photodiode with low dark current. *Optics express*, 19(25):24897–24904, 2011.

[24] Ning Duan, S Wang, XG Zheng, X Li, Ning Li, Joe C Campbell, Chad Wang, and Larry A Coldren. Detrimental effect of impact ionization in the absorption region on the frequency response and excess noise performance of ingaas-inalas sacm avalanche photodiodes. *IEEE journal of quantum electronics*, 41(4):568–572, 2005.

[25] Ning Duan, Shuling Wang, Feng Ma, Ning Li, J. C. Campbell, Chad Wang, and L. A. Coldren. High-speed and low-noise sacm avalanche photodiodes with an impact-ionization-engineered multiplication region. *IEEE Photonics Technology Letters*, 17(8):1719–1721, Aug 2005.

[26] Y. M. El-Batawy and M. J. Deen. Modeling and optimization of resonant cavity enhanced-separated absorption graded charge multiplication-avalanche photodetector (rce-sagcm-apd). *IEEE Transactions on Electron Devices*, 50(3):790–801, March 2003.

[27] RB Emmons. Avalanche-photodiode frequency response. *Journal of Applied Physics*, 38(9):3705–3714, 1967.

[28] Qing Fang, Lianxi Jia, Junfeng Song, Andy EJ Lim, Xiaoguang Tu, Xianshu Luo, Mingbin Yu, and Guoqiang Lo. Demonstration of a vertical pin ge-on-si photo-detector on a wet-etched si recess. *Optics express*, 21(20):23325–23330, 2013.

[29] S Forrest. Performance of in x ga 1-x as y p 1-y photodiodes with dark current limited by diffusion, generation recombination, and tunneling. *IEEE Journal of quantum Electronics*, 17(2):217–226, 1981.

[30] H Fukano, A Kozen, K Kato, and O Nakajima. Edge-illuminated refracting-facet photodiode with high responsivity and low-operation voltage. *Electronics Letters*, 32(25):2346–2348, 1996.

[31] H Fukano, Y Muramoto, K Takahata, and Y Matsuoka. High efficiency edge-illuminated uni-travelling-carrier-structure refracting-facet photodiode. *Electronics Letters*, 35(19):1664–1665, 1999.

[32] Khaled Gasmi. Fast and low noise optical receiver using si apd for cloud-aerosol lidar. In *Optical Sensing and Detection IV*, volume 9899, page 98990I. International Society for Optics and Photonics, 2016.

[33] Steve Gorshe and Zdzislaw Papir. The status and evolution of the full-service access network standard (guest editorial). *IEEE Communications Magazine*, 39(12):116–116, 2001.

[34] E Gramsch, M Szawlowski, S Zhang, and M Madden. Fast, high density avalanche photodiode array. *IEEE transactions on nuclear science*, 41(4):762–766, 1994.

[35] Martin A Green. Self-consistent optical parameters of intrinsic silicon at 300 k including temperature coefficients. *Solar Energy Materials and Solar Cells*, 92(11):1305–1310, 2008.

[36] Martin A Green and Mark J Keevers. Optical properties of intrinsic silicon at 300 k. *Progress in Photovoltaics: Research and Applications*, 3(3):189–192, 1995.

[37] Chris Groves, Chon Chia, R.C. Tozer, J.P.R. David, and G.J. Rees. Avalanche noise characteristics of single alxga1-xas(0.3¡x¡0.6)-gaas heterojunction apds. 41:70 – 75, 02 2005.

[38] M. M. Hayat, Oh-Hyun Kwon, Yi Pan, P. Sotirelis, J. C. Campbell, B. E. A. Saleh, and M. C. Teich. Gain-bandwidth characteristics of thin avalanche photodiodes. *IEEE Transactions on Electron Devices*, 49(5):770–781, May 2002.

[39] Majeed M Hayat, Payman Zarkesh-Ha, Georges El-Howayek, Robert Efroymson, and Joe C Campbell. Breaking the buildup-time limit of sensitivity in avalanche photodiodes by dynamic biasing. *Optics express*, 23(18):24035–24041, 2015.

[40] CH Henry, RA Logan, and KA Bertness. Spectral dependence of the change in refractive index due to carrier injection in gaas lasers. *Journal of Applied Physics*, 52(7):4457–4461, 1981.

[41] Y Hirota, Y Muramoto, T Takeshita, T Ito, H Ito, S Ando, and T Ishibashi. Reliable non-zn-diffused inp/ingaas avalanche photodiode with buried n-inp layer operated by electron injection mode. *Electronics Letters*, 40(21):1378–1379, 2004.

[42] Yukihiro Hirota, Seigo Ando, and Tadao Ishibashi. High-speed avalanche photodiode with a neutral absorption layer for 1.55 μm wavelength. *Japanese journal of applied physics*, 43(3A):L375, 2004.

[43] Mengyuan Huang, Pengfei Cai, Su Li, Guanghui Hou, Naichuan Zhang, Tzung-I Su, Ching-yin Hong, and Dong Pan. 56ghz waveguide ge/si avalanche photodiode. In *2018 Optical Fiber Communications Conference and Exposition (OFC)*, pages 1–3. IEEE, 2018.

[44] Zhihong Huang, Cheng Li, Di Liang, Kunzhi Yu, Charles Santori, Marco Fiorentino, Wayne Sorin, Samuel Palermo, and Raymond G Beausoleil. 25 gbps low-voltage waveguide si–ge avalanche photodiode. *Optica*, 3(8):793–798, 2016.

[45] Shivkumar Kalyanaraman, Dibyendu Shekhar, and Kalyan Kidambi. Tcp/ip performance optimization over adsl. *GI2000*, 1995.

[46] Yimin Kang, Zhihong Huang, Yuval Saado, Joe Campbell, Alex Pauchard, John Bowers, and Mario Paniccia. High performance ge/si avalanche photodiodes development in intel. In *Optical Fiber Communication Conference*, page OWZ1. Optical Society of America, 2011.

[47] Yimin Kang, Han-Din Liu, Mike Morse, Mario J Paniccia, Moshe Zadka, Stas Litski, Gadi Sarid, Alexandre Pauchard, Ying-Hao Kuo, Hui-Wen Chen, et al. Monolithic germanium/silicon avalanche photodiodes with 340 ghz gain–bandwidth product. *Nature photonics*, 3(1):59, 2009.

[48] Jun-ichi Kani, Fabrice Bourgart, Anna Cui, Albert Rafel, Malcolm Campbell, Russell Davey, and Silvana Rodrigues. Next-generation pon-part i: Technology roadmap and general requirements. *IEEE Communications Magazine*, 47(11), 2009.

[49] Gerd Keiser. *FTTX concepts and applications*, volume 91. John Wiley & Sons, 2006.

[50] RJ King and KW Raine. Light reflection. http://www.kayelaby.npl.co.uk/general_physics/2_5/2_5_9.html, 2017. [Online; accessed 11-May-2018].

[51] GS Kinsey, JC Campbell, and AG Dentai. Waveguide avalanche photodiode operating at 1.55 μm with a gain-bandwidth product of 320 ghz. *IEEE Photonics Technology Letters*, 13(8):842–844, 2001.

[52] Oh-Hyun Kwon, M. M. Hayat, Shuling Wang, J. C. Campbell, A. Holmes, Yi Pan, B. E. A. Saleh, and M. C. Teich. Optimal excess noise reduction in thin heterojunction al/sub 0.6/ga/sub 0.4/as-gaas avalanche photodiodes. *IEEE Journal of Quantum Electronics*, 39(10):1287–1296, Oct 2003.

[53] C Lenox, H Nie, P Yuan, G Kinsey, AL Homles, BG Streetman, and JC Campbell. Resonant-cavity ingaas-inalas avalanche photodiodes with gain-bandwidth product of 290 ghz. *IEEE Photonics Technology Letters*, 11(9):1162–1164, 1999.

[54] Tsung-Yang Liow, Kah-Wee Ang, Qing Fang, Jun-Feng Song, Yong-Zhong Xiong, Ming-Bin Yu, Guo-Qiang Lo, and Dim-Lee Kwong. Silicon modulators and germanium photodetectors on soi: monolithic integration, compatibility, and performance optimization. *IEEE Journal of Selected Topics in Quantum Electronics*, 16(1):307–315, 2010.

[55] Zhipeng Lv and Jianhua Liu. Method and device for dynamic spectrum management of xdsl upstream and downstream shared frequency, December 6 2007. US Patent App. 11/612,965.

[56] W Maes, K De Meyer, and R Van Overstraeten. Impact ionization in silicon: A review and update. *Solid-State Electronics*, 33(6):705–718, 1990.

[57] IH Malitson. Interspecimen comparison of the refractive index of fused silica. *Josa*, 55(10):1205–1209, 1965.

[58] Baria Dipikaben Manharbhai, Amit Kumar Garg, and Vijay Janyani. A flexible remote node architecture for energy efficient direct onu internetworking in tdm pon. *2017 International Conference on Computer, Communications and Electronics (Comptelix)*, pages 453–457, 2017.

[59] Andrew RJ Marshall, Chee Hing Tan, John PR David, Jo Shien Ng, and Mark Hopkinson. Fabrication of inas photodiodes with reduced surface leakage current. In *Optical Materials in Defence Systems Technology IV*, volume 6740, page 67400H. International Society for Optics and Photonics, 2007.

[60] RJ McIntyre. Multiplication noise in uniform avalanche diodes. *IEEE Transactions on Electron Devices*, 13(1):164–168, 1966.

[61] Duilio Meglio, Corrado Cianci, Aldo Di Carlo, and Paolo Lugli. Non local impact ionization effects in semiconductor devices. *VLSI Design*, 6(1-4):291–297, 1998.

[62] Hektor Taavi Josef Meier. *Design, characterization and simulation of avalanche photodiodes*. PhD thesis, ETH Zurich, 2011.

[63] Derek Nesset. Ng-pon2 technology and standards. *Journal of Lightwave Technology*, 33(5):1136–1143, 2015.

[64] C Novo, R Giacomini, R Doria, Aryan Afzalian, and Denis Flandre. Illuminated to dark ratio improvement in lateral soi pin photodiodes at high temperatures. *Semiconductor Science and Technology*, 29(7):075008, 2014.

[65] D Renker and E Lorenz. Advances in solid state photon detectors. *Journal of Instrumentation*, 4(04):P04004, 2009.

[66] PL Richards. Bolometers for infrared and millimeter waves. *Journal of Applied Physics*, 76(1):1–24, 1994.

[67] Bahaa EA Saleh, Malvin Carl Teich, and Bahaa E Saleh. *Fundamentals of photonics*, volume 22. Wiley New York, 1991.

[68] Mohammad A Saleh, Majeed M Hayat, Bahaa EA Saleh, and Malvin Carl Teich. Dead-space-based theory correctly predicts excess noise factor for thin gaas and algaas avalanche photodiodes. *IEEE Transactions on Electron Devices*, 47(3):625–633, 2000.

[69] Gangxiang Shen, Rodney S Tucker, and Chang-Joon Chae. Fixed mobile convergence architectures for broadband access: Integration of epon and wimax [topics in optical communications]. *IEEE Communications Magazine*, 45(8):44–50, 2007.

[70] Mohammad Soltani and Richard Soref. Free-carrier electrorefraction and electroabsorption in wurtzite gan. *Optics Express*, 23(19):24984–24990, 2015.

[71] RICHARDA Soref and BRIANR Bennett. Electrooptical effects in silicon. *IEEE journal of quantum electronics*, 23(1):123–129, 1987.

[72] S.M. SZE. *Semiconductor Devices*. Wiley, 1985.

[73] Chee Tan, J.P.R. David, S.A. Plimmer, G.J. Rees, R.C. Tozer, and Robert Grey. Low multiplication noise thin al0.6ga0.4as avalanche photodiodes. 48:1310 – 1317, 08 2001.

[74] CZ Tan. Determination of refractive index of silica glass for infrared wavelengths by ir spectroscopy. *Journal of Non-Crystalline Solids*, 223(1-2):158–163, 1998.

[75] R Van Overstraeten and H De Man. Measurement of the ionization rates in diffused silicon pn junctions. *Solid-State Electronics*, 13(5):583–608, 1970.

[76] Oomman K Varghese and Craig A Grimes. Appropriate strategies for determining the photoconversion efficiency of water photoelectrolysis cells: a review with examples using titania nanotube array photoanodes. *Solar Energy Materials and Solar Cells*, 92(4):374–384, 2008.

[77] Roman Vitenberg. Source adaptive digital subscriber line and method, July 13 2004. US Patent 6,763,097.

[78] Laurent Vivien, Johann Osmond, Jean-Marc Fédéli, Delphine Marris-Morini, Paul Crozat, Jean-François Damlencourt, Eric Cassan, Y Lecunff, and Suzanne Laval. 42 ghz pin germanium photodetector integrated in a silicon-on-insulator waveguide. *Optics express*, 17(8):6252–6257, 2009.

[79] I Watanabe, M Tsuji, K Makita, and K Taguchi. Gain-bandwidth product analysis of inalgaas-inalas superlattice avalanche photodiodes. *IEEE Photonics Technology Letters*, 8(2):269–271, 1996.

[80] Pawel Wiatr. *Energy Saving vs. Performance: Trade-offs in Optical Networks*. PhD thesis, KTH Royal Institute of Technology, 2016.

[81] KJ Willis, JS Ayubi-Moak, SC Hagness, and I Knezevic. Global modeling of carrier-field dynamics in semiconductors using emc–fdtd. *Journal of computational electronics*, 8(2):153, 2009.

[82] P. Yuan, S. Wang, X. Sun, X. G. Zheng, A. L. Holmes, and J. C. Campbell. Avalanche photodiodes with an impact-ionization-engineered multiplication region. *IEEE Photonics Technology Letters*, 12(10):1370–1372, Oct 2000.

[83] Edward F Zalewski and C Richard Duda. Silicon photodiode device with 100% external quantum efficiency. *Applied optics*, 22(18):2867–2873, 1983.

[84] Jingjing Zhang and Nirwan Ansari. Toward energy-efficient 1g-epon and 10g-epon with sleep-aware mac control and scheduling. *IEEE Communications Magazine*, 49(2):s33–s38, 2011.

Appendix

Deriving Multiplication Gain

The process of deriving the multiplication gain is initiated by determining the bias voltage at which the second derivative of the photocurrent with respect to voltage is zero ($\partial^2 I_p / \partial V^2 = 0$), which will be the unity gain voltage. Thereafter, the multiplication gain at each voltage, is derived by diving its corresponding photocurrent to the photocurrent at unity gain.[1]

In this work, similar to what Lumerical currently presents[2], the above calculations are performed on current. This means that dark current is also included in the derivation of multiplication gain.

[1] Meier, Hektor Taavi Josef. "Design, characterization and simulation of avalanche photodiodes." PhD diss., ETH Zurich, 2011.

[2] 10-V Ge-on-Si APD with Si multiplication. www.kb.lumerical.com/en/ photodetectors avalanche-photodetector.html. Accessed: 2018-10-08